Technical Physics Letters, Vol. 31, No. 5, 2005, pp. 359–360. Translated from Pis'ma v Zhurnal Tekhnicheskoĭ Fiziki, Vol. 31, No. 9, 2005, pp. 1–5.

Effect of Gamma Radiation on the Properties of InSe Photodiodes

Z. D. Kovalyuk*, V. N. Katerynchuk, O. A. Politanska, O. N. Sydor, and V. V. Khomyak

Frantsevich Institute for Problems of Materials Science (Chernivtsy Department), National Academy of Sciences of Ukraine, Chernivtsy, Ukraine

Chernivtsy National University, Chernivtsy, Ukraine

** e-mail: chimsp@unicom.cv.ua*

Received November 29, 2004

Abstract—We have studied the influence of γ radiation (^{60}Co source) on the photoelectric parameters of InSe diodes based on the direct optical contact *p*-InSe/*n*-InSe. The penetrating radiation produces defects of the acceptor type in the base material, but does not lead to any significant degradation of the energy barrier. The irradiation even improves the parameters of InSe photodiodes, which is manifested by an increase in both the open-circuit voltage and the short-circuit current. © *2005 Pleiades Publishing, Inc.*

Introduction. An important task of semiconductor materials science is not only to develop radiation-resistant materials but also to study the behavior of devices based on such materials under conditions involving exposure to hard radiation. Silicon, germanium, and gallium arsenide are still the most widely used materials in semiconductor electronics. As is known, exposure of these semiconductors to penetrating radiation is accompanied by the accumulation of irreversible structural damage, which results in significant negative changes in the physical characteristics and leads eventually to degradation and failure of the devices based on such materials [1–3].

Layered crystals of indium selenide (InSe) typically contain structural defects of the stacking fault type [4], which determine a polytypism of the InSe crystal structure [5]. These defects, which are related to violation of the translational order of atoms along the crystallographic axis *C*, account for the relatively low mobility and short diffusion length of charge carriers in this direction. However, it is still unclear how the radiation-induced defects influence the crystal subsystem comprising a large number of intrinsic defects.

This study was devoted to elucidation of the effect of γ radiation on the photoelectric characteristics of InSe photodiodes.

Experimental. The InSe homojunctions were created by means of direct optical contact between semiconductor crystals [6]. Using this method, it is possible to obtain homo- and heterojunctions of various types owing to a high quality of the surface of plates cleaved from an ingot of stratified InSe single crystal.

InSe single crystals of the *n* and *p* types were grown using the vertical Bridgman technique. The frontal semiconductor layer was in the form of a thin (20- to 30-μm thick) *n*-InSe plate, while the base crystal was *p*-InSe doped with cadmium. The electric conductivity of the front semiconductor was higher by two orders of magnitude than that of the *p*-type crystal (10^3–10^4 Ω^{-1} cm^{-1}). The electric contacts were formed by vacuum deposition of pure indium.

The samples were irradiated at room temperatures by γ quanta from a continuous source based on the ^{60}Co isotope (E = 1.25 MeV). The total radiation dose was 10 or 300 R.

Results and discussion. The results of determination of the photoelectric parameters of InSe diodes measured before and after irradiation to various doses are presented in the table. As can be seen, there is a clearly pronounced tendency to increase in both open-circuit voltage V_{oc} and short-circuit current density J_{sc} with increasing radiation dose. The maximum increment of V_{oc} is 30%, while the J_{sc} value exhibits a 17-fold growth.

Figure 1 shows the spectra of the quantum efficiency η of the photocurrent for InSe homojunctions studied before and after irradiation. The long-wave-

Open-circuit saturation voltage (V_{oc}) and short-circuit current density (J_{sc}) of InSe diodes based on the *p*–*n* homojunction measured before after irradiation to various doses D at T = 293 K

D, R	V_{oc}, V	J_{sc}, mA/cm^2
0	0.4	0.12
10	0.44	0.24
300	0.52	2.0

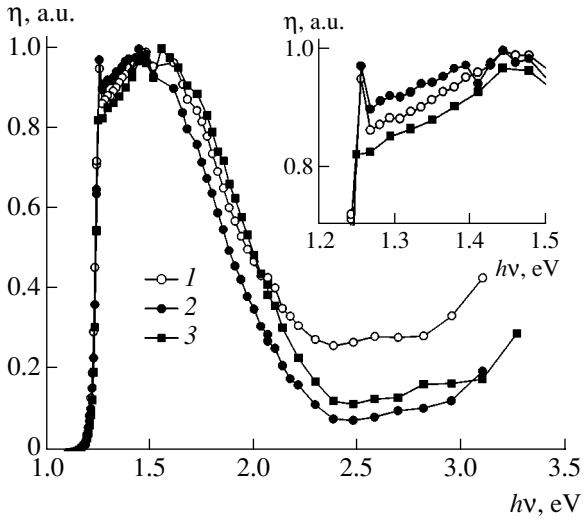

Fig. 1. Spectra of the quantum efficiency η of the photocurrent in InSe diodes (*1*) before and (*2*, *3*) after irradiation to a total dose of $D = 10$ (*2*) and 300 R (*3*) at $T = 293$ K. The inset shows the region of the exciton absorption on a greater scale.

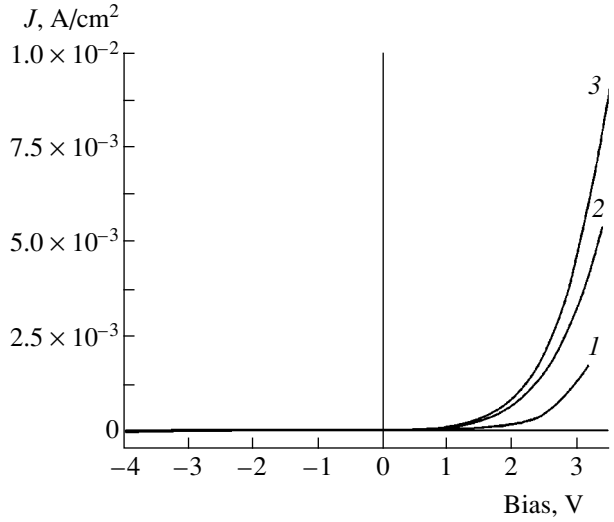

Fig. 2. The *J*–*V* curves of InSe diodes (*1*) before and (*2*, *3*) after irradiation to a total dose of $D = 10$ (*2*) and 300 R (*3*) at $T = 293$ K.

length region of the spectrum exhibits a sharp peak corresponding to the exciton absorption in InSe [7]. This peak is virtually not affected by small radiation doses (~10 R), but it vanishes when the dose is increased to 300 R (see the inset in Fig. 1). As is known, exciton absorption is not observed in structurally imperfect crystals. Therefore, the formation of radiation-induced defects leads to the same result. In the short-wavelength spectral range, the photosensitivity exhibits a decay that is related to the presence of surface states and to an increase in the surface recombination rate [8]. On the other hand, the observed changes in the quantum efficiency spectra are rather insignificant and only show evidence of the radiation defect formation.

More significant changes were observed for the *J*–*V* curves of the *p*–*n*-InSe homojunctions (Fig. 2). The exposure to γ radiation is accompanied by an increase in the rectification coefficient, and this tendency is retained with increasing radiation dose (cf. curves *2* and *3* in Fig. 2). An analysis of the *J*–*V* curve showed that the irradiation gives rise to V_{oc} and leads to a change in the parameters of the exponential relation between current and voltage. This may be caused by two factors: (i) a growth in the potential barrier and (ii) an increase in the conductivity of the homojunction base. The exposure to high-energy γ quanta leads to the formation of structural defects, which behave similarly to acceptor impurities and produce a shift of the Fermi levels in the contacting semiconductors, thus increasing the contact potential difference.

Conclusions. The observed changes in the characteristics of InSe diodes, which are improved under the action of irradiation, show evidence for the formation of structural defects. These defects exhibit the acceptor character and produce no negative influence on the *p*–*n* junction. The exposure to γ radiation leads to no significant changes in the spectrum of the photoresponse but is accompanied by an increase in the rectification coefficient and in the photoelectric parameters of the homojunctions (open-circuit voltage and short-circuit current).

Thus, InSe photodiodes based on the *p*–*n* homojunctions exhibit no decrease in characteristics upon irradiation to small doses (~300 R) and, hence, can be used under conditions of elevated radiation background.

REFERENCES

1. V. S. Vavilov, N. P. Kekelidze, and L. S. Smirnov, *Effects of Radiation on Semiconductors* (Nauka, Moscow, 1988; Consultants Bureau, New York, 1965).
2. *Physical Processes in Irradiated Semiconductors*, Ed. by L. S. Smirnov (Nauka, Novosibirsk, 1977) [in Russian].
3. F. P. Korshunov, G. V. Gatal'skiĭ, and G. M. Ivanov, *Radiation Effects in Semiconductor Devices* (Nauka i Tekhnika, Minsk, 1978) [in Russian].
4. Z. T. Kuznicki, K. Maschke, and Ph. E. Schmid, J. Phys. C **12**, 3749 (1979).
5. J. C. Terhell, Prog. Cryst. Growth Charact. **7**, 55 (1983).
6. V. L. Bakumenko and V. F. Chishko, Fiz. Tekh. Poluprovodn. (Leningrad) **11**, 2000 (1977) [Sov. Phys. Semicond. **11** (1977)].
7. V. N. Katerynchuk and M. Z. Kovalyuk, Fiz. Tekh. Poluprovodn. (Leningrad) **25**, 954 (1991) [Sov. Phys. Semicond. **25** (1991)].
8. S. Sze, *Physics of Semiconductor Devices* (Wiley, New York, 1981), Vol. 2.

Translated by P. Pozdeev

Technical Physics Letters, Vol. 31, No. 5, 2005, pp. 361–363. Translated from Pis'ma v Zhurnal Tekhnicheskoĭ Fiziki, Vol. 31, No. 9, 2005, pp. 6–13.

Percolation in Laser Ablation of Binary Mixtures

N. E. Kask* and S. V. Michurin

Skobel'tsyn Institute of Nuclear Physics, Moscow State University, Moscow, 119899 Russia

** e-mail: nek@srd.sinp.msu.ru*

Received November 3, 2004

Abstract—We have studied the optical emission of plasma expanding from a target made of a binary alloy or a pressed powder mixture and ablated by nanosecond laser pulses of moderate power. The intensity of spectral lines has been studied for the first time as dependent on the target composition. It is established that a three-dimensional percolation takes place in the plasma, with a percolation threshold determined by the atomic density of a metal component in the target composition. © *2005 Pleiades Publishing, Inc.*

Introduction. The formation of nanodimensional clusters during pulsed laser ablation of targets has been extensively studied in recent years in the context of solving certain problems of nanotechnology. The laser plasma parameters depend on the irradiation conditions and rapidly vary after termination of a single laser pulse. The dynamics of plasma expanding into the gas phase, the plasma composition, and the characteristics of various processes (absorption of laser radiation, heating, ionization, recombination, condensation, and clusterization) in the plume depend on various factors, in particular, on the pressure produced by the ambient (buffer) gas.

According to Harilal *et al.* [1], laser plasma exhibits adiabatic expansion at pressures below 1 Pa. The collisions of plasma particles with atoms of the ambient gas become significant at a pressure of ~10 Pa, as manifested by a significant increase in the intensity of emission from the plume observed 1–2 μs after termination of the laser pulse. In the case of a plasma expanding into vacuum during the ablation of aluminum [1] and silicon [2] targets, the relative intensities of ion emission lines show that the plasma temperature reaches a maximum (~10^4 K) at the end of the laser pulse and then decays at a characteristic time of ~10^{-7} s. Evidently, the increase in intensity of emission observed with microsecond intervals in the course of plasma expansion into a surrounding gas is related to a change in the emissivity (and absorption) of the plasma as a result of the condensation and clusterization processes.

According to the results of our previous investigations [3–5], the intensity of continuous emission in the case of millisecond laser pulses is correlated with a threshold behavior of the high-frequency conductivity as a function of the laser composition (this behavior is characteristic of percolation) and with the appearance of fractal nanostructures. As the ambient gas pressure increases, the effective brightness and color temperatures (characterizing the continuous emission) exhibit a jumplike increase to a level above the boiling point of the target material [6]. This is accompanied by a change in the shape and size of the plume and by the formation of a macroscopic fractal shell in its peripheral layers [5].

The continuous emission spectrum and a high microwave conductivity of the plasma are related to the presence of percolation clusters in the plume volume. These clusters, in contrast to compact ones, do not vanish when the temperature increases above the boiling point. For such clusters to exist, it is necessary that the density of medium exceed a certain critical value. Percolation must also take place when targets are ablated by shorter laser pulses, since the greater the flux intensity, the higher the density of the near-surface plasma. Experimental investigations of the plasma formed in the nanosecond range of laser pulse durations encounter difficulties related to plasma degradation and to the requirement of high temporal resolution of the measuring equipment. An alternative approach to the study of clusterization phenomena is offered by methods developed previously [3–6] for the investigation of percolation in laser plumes at the surface of composite targets and the analysis of spectral features of the continuous emission.

This paper presents the results of experimental investigation of the phenomenon of percolation in the plasma formed at the surface of a binary target ablated by nanosecond laser pulses.

Experimental setup and methods. The experimental setup used for the investigation of emission from the plume in a broad range of the buffer gas pressures (1–10^7 Pa) was described in detail elsewhere [6]. In this study, binary targets were ablated by single pulses of a Nd:YAG laser with λ = 1.06 μm, a pulse duration of ~10 ns, a pulse energy of ~10 mJ, and a power density of ~10^8 W/cm^2 in the laser spot.

We have measured the spectra of emission from plumes formed at the surface of binary targets representing either pressed powder mixtures or binary alloys (Cu_xAl_{1-x} and Cu_xNi_{1-x}). The powder mixtures were

1063-7850/05/3105-0361$26.00

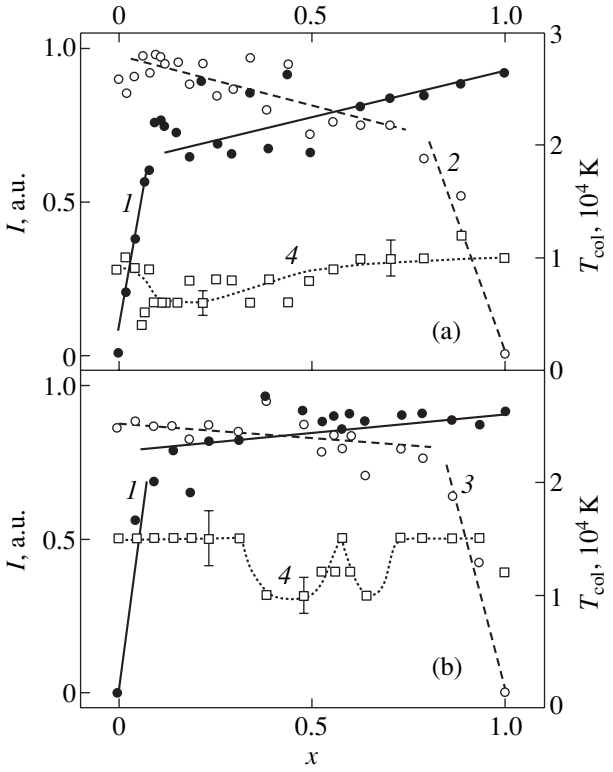

Fig. 1. Plots of the atomic spectral line intensity I versus composition (x is the atomic fraction of copper) for a binary alloy target ablated by nanosecond laser pulses at a buffer gas pressure of 10^5 Pa: (a) Cu_xAl_{1-x} alloy in argon; (b) Cu_xNi_{1-x} in air; (*1*) Cu, $\lambda \approx 0.5105$ μm; (*2*) Al, $\lambda \approx 0.3964$ μm; (*3*) Ni, $\lambda \approx 0.5477$ μm; (*4*) effective color temperature T_{col} of the plume.

melted in electric arc between tungsten electrodes in argon at normal pressure.

The results of control experiments using repeated laser pulses allowed the optimum conditions of irradiation to be selected to ensure reproducibility of the emission caused by two sequential laser pulses. These were the first and second pulses in the case of alloys, and the second and third pulses for powder mixtures, after which the target was shifted. The geometry of irradiation and the laser pulse parameters in the course of these measurements remained unchanged. The emission was taken in the direction perpendicular to the plume axis, from a plasma region spaced by ≈1 mm from the target surface. In the course of investigation of the effects of target composition, the size and shape of the plume (which depend predominantly on the laser pulse intensity and the ambient gas pressure [2]) also remained unchanged. One aim of this study was to determine the effect of the target composition on the effective temperatures in the laser plume. The observed significant excess of the effective color temperature ($T_{col} \geq 5000$ K) over the brightness temperature ($T_{br} \leq 3000$ K) in the visible spectral range indicates that the plasma layer is optically thin. The absorption of emission at discrete frequencies was also ignored, since the measurements were performed for low-intensity spectral lines corresponding to the transitions of subordinate series.

In the analysis of experimental data, it was assumed that (i) the target components are uniformly distributed in the plume volume and (ii) their relative densities in the evaporated substance are the same as in the target. The fraction of free atoms in the laser plasma was determined using the intensity of discrete atomic emission lines.

Experimental results and discussion. During the laser ablation of binary copper-based alloys with aluminum and nickel, we monitored the intensities of spectral lines belonging to Cu ($\lambda = 0.5105$ μm), Al ($\lambda = 0.3964$ μm), and Ni atoms ($\lambda = 0.5477$ μm). Figures 1a and 1b show plots of these intensities versus the relative number of Cu atoms in the target composition. These experimental data were obtained for a normal pressure of the buffer gas (Ar for Cu_xAl_{1-x}; air for Cu_xNi_{1-x}).

In the absence of absorption, the intensity of each spectral line must be proportional to the density of the corresponding metal component in the plume volume (provided that the line widths and shapes exhibit no significant variations). The full widths at half maximum (FWHM) of the monitored spectral lines were independent of the target composition and the buffer gas pressure and amounted to 0.37 ± 0.04, 1 ± 0.05, and 0.4 ± 0.04 nm for Cu, Al, and Ni, respectively. As can be seen from Fig. 1, deviations from the proportionality between the line intensity and the component density in the plasma are observed when the relative atomic density exceeds $n_a \sim 0.15$, which is a level characteristic of the three-dimensional percolation threshold [7]. Therefore, it was natural to assume that saturation of the intensity of the atomic spectral lines (Fig. 1) is related to a limitation on the number of free atoms in the plasma as a result of the formation of bound structures (clusters). Since the model of compact clusters is inconsistent with a rather high gas temperature (~1 eV) of the plasma at the moment of laser pulse action (when the intensities of spectral lines are at maximum [2]), the formation of "hot" bound structures is most probably explained in terms of the model of gaslike clusters [8] and the model of percolation cluster.

If the percolation threshold on the axis of compositions is determined as the position of a local maximum or a bending point, the binary metal alloys are characterized by the following values: 0.5 ± 0.05, 0.4 ± 0.04, and 1.3 ± 0.2 nm for Cu, Ni, and Al, respectively. During the laser ablation of binary metal targets (both alloys and powder mixtures), the percolation thresholds appear separately for each metal component and do not influence the behavior of the other components. In the case of a metal–salt mixture, the spectrum of the plume contains both the discrete lines of the metal component, the continuum, and the atomic spectrum of metal atoms entering into the salt molecules. The maximum inten-

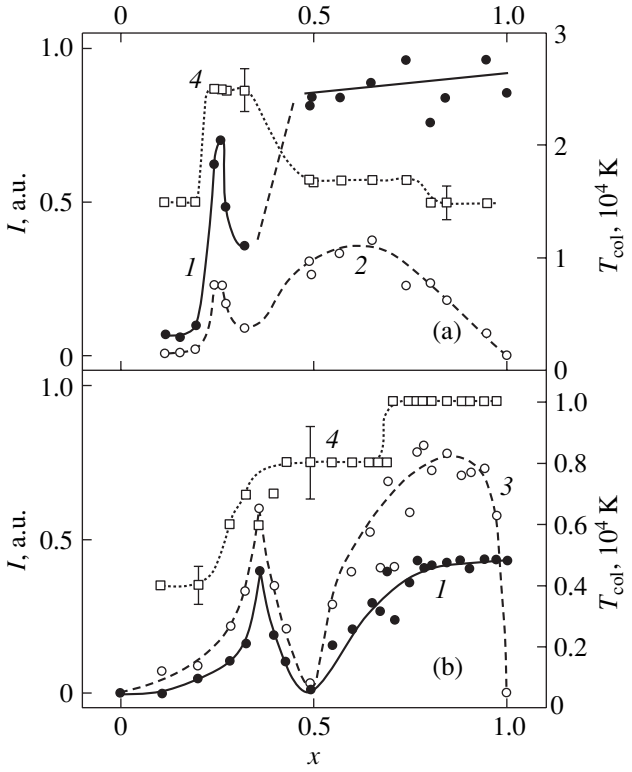

Fig. 2. Plots of the atomic spectral line intensity I versus composition (x is the atomic fraction of aluminum) for a pressed powder mixture target ablated by nanosecond laser pulses at a buffer gas (air) pressure of 10^5 Pa: (a) Al–LiF mixture; (b) Al–MgF_2 mixture; (*1*) Al, $\lambda \approx 0.3964$ μm; (*2*) Li, $\lambda \approx 0.4273$ μm; (*3*) Mg, $\lambda \approx 0.3838$ μm; (*4*) effective color temperature T_{col} of the plume.

sity of the spectral lines of aluminum in a mixture with salt was observed for a relative atomic density of $n_a' \sim 0.3$ (Figs. 2a and 2b). This value is about one and half times the percolation threshold for aluminum in the binary mixtures. This difference is probably related to a decrease in the content of free aluminum atoms, which is explained by their involvement in chemical reactions with the formation of fluorides AlF_n ($n \leq 3$) and by the liberation of metal atoms from salt molecules. In contrast to the results for alloys, the spectral line intensity in the case of pressed metal–salt powder mixtures sharply decreases above the percolation threshold. This can be interpreted as being due to the fact that aluminum atoms entering into a percolation cluster do not participate in chemical reactions.

It should be noted that a target made of a powder mixture can also be considered as a medium featuring three-dimensional percolation. However, the percolation threshold in such objects is determined by the volume ratio of the mixture components, rather than by their atomic densities [7]. Representation of the experimental results in Figs. 1 and 2 as functions of the volume fractions of components in the target leads to a much greater difference between percolation thresholds of the given metal (e.g., of copper in different alloys or aluminum in mixtures with different salts).

An alternative model for hot structures formed in a dense vapor is offered by the model of a gaslike cluster with the minimum number of bonds between atoms [8]. At a sufficiently high temperature, such structures appear as spontaneously formed (virtual) atomic chains. Since the critical density for the formation of one-dimensional chains (percolation threshold) is close to unity, this model is inconsistent with the experimental results obtained in this study. Our results are also at variance with the two-phase cluster model [9], according to which the outer monolayer of a compact cluster consists of particles with small numbers of bonds. Indeed, percolation in a two-dimensional layer is characterized by a threshold of 0.5. Zhukhovitskiĭ [10] proposed a generalized model of virtual chains, in which a cluster comprising a fractallike system of bound atomic chains has a topology close to that of the percolation cluster.

Conclusions. The results of our investigation showed that plasma generated during ablation of targets by nanosecond laser pulses and expanding into a buffer gas contains three-dimensional percolation clusters. The percolation threshold is determined by the critical atomic density of each evaporated metal component of the target. Such "hot" percolation clusters determine the absorption capacity, temperature, and spectral continuum of emission from the laser plasma.

Acknowledgments. This study was supported by the Russian foundation for Basic Research (project no. 03-02-17026) and the Program of Support for Leading Scientific Schools in Russia (NSh-1771.2003.2).

REFERENCES

1. S. S. Harilal, C. V. Bindhu, M. S. Tillack, *et al.*, J. Appl. Phys. **93**, 2380 (2003).
2. M. S. Tillack, D. W. Blair, and S. S. Harilal, Nanotechnology **15**, 390 (2004).
3. H. E. Kask, Pis'ma Zh. Éksp. Teor. Fiz. **60**, 204 (1994) [JETP Lett. **60**, 212 (1994)].
4. N. E. Kask, S. V. Michurin, and G. M. Fedorov, Zh. Éksp. Teor. Fiz. **116**, 1979 (1999) [JETP **89**, 1072 (1999].
5. N. E. Kask, E. G. Leksina, S. V. Michurin, *et al.*, Kvantovaya Élektron. (Moscow) **32**, 437 (2002).
6. N. E. Kask, S. V. Michurin, and G. M. Fedorov, Kvantovaya Élektron. (Moscow) **34**, 524 (2004).
7. B. I. Shklovskii and A. L. Efros, *Electronic Properties of Doped Semiconductors* (Nauka, Moscow, 1979; Springer-Verlag, New York, 1984).
8. D. I. Zhukhovitskiĭ, Zh. Éksp. Teor. Fiz. **113**, 181 (1998) [JETP **86**, 101 (1998)].
9. D. I. Zhukhovitskiĭ, Zh. Éksp. Teor. Fiz. **121**, 396 (2002) [JETP **94**, 336 (2002)].
10. D. I. Zhukhovitskiĭ, Zh. Fiz. Khim. **75**, 1159 (2001).

Translated by P. Pozdeev

Technical Physics Letters, Vol. 31, No. 5, 2005, pp. 364–366. Translated from Pis'ma v Zhurnal Tekhnicheskoĭ Fiziki, Vol. 31, No. 9, 2005, pp. 14–19.

The Effect of Weak Pulsed Magnetic Fields on Modified Wood

V. V. Postnikov*, M. N. Levin, N. N. Matveev, R. V. Skoridanov, N. S. Kamalova, and V. A. Shamaev

Voronezh State Academy of Forestry, Voronezh, Russia
Voronezh State University, Voronezh, Russia
** e-mail: vvpost@icmail.ru*
Received November 23, 2004

Abstract—The edge hardness of birch wood modified under the action of a weak (not exceeding 0.5 T) pulsed magnetic field is increased as compared to the initial level. The magnetic field effect has a threshold (0.2 T) and is explained by a decrease in the mobility of wood fibers as a result of the field-induced cross linking between side groups of cellulose macromolecules. *© 2005 Pleiades Publishing, Inc.*

Modified wood is widely used as a material replacing ferrous and nonferrous metals, textolite, plastics, and other structural materials [1]. In particular, relatively cheap slider bearings made of pressed wood exhibit sufficiently high strength and can be successfully used as support bearings in rolling mills of metalworking plants. The working life of such bearings is determined by the strength of the pressed wood. Therefore, the task of increasing the strength of modified wood is a currently important problem.

As is known [2], wood is a multicomponent natural polymer with a net composition in the absolutely dry state including ~49.5% carbon, 44.2% oxygen, and 6.3% hydrogen—the base elements of many other high-molecular-weight organic compounds. For this reason, the physical properties of wood are frequently studied by the same methods as those used for the characterization of polymers.

The main component of wood, which accounts for about half of the material composition, is cellulose—a polymer known to be capable of readily converting into a crystalline state [3]. In recent years, it was established that weak pulsed and constant magnetic fields may produce significant changes in the structure and mechanical properties of some crystallizable polymers (see, e.g., [4–7]). These phenomena stimulate interest in investigations of the possibility of using pulsed magnetic fields for modification of the mechanical properties of pressed wood. This Letter presents the results of the first study of the effect of a weak (not exceeding 0.5 T) magnetic field on the strength of pressed birch wood.

The experiments were performed with 15 × 15 × 15-mm samples of birch wood obtained by hydrostatic pressing. The wood was preliminarily plasticized under the action of a 25% aqueous ammonia solution for 24 h at T = 293 K, followed by drying for 12 h at T = 350 K [1]. The density of the pressed wood samples was ρ = (1.35–1.45) × 10^3 kg/m^3 at a relative humidity not exceeding 5%. These characteristics were determined using a high-precision balance of the VLR-200 type, which provided for sample weighing with an error not exceeding 0.5 mg.

The hardness measurements were performed using a Rockwell hardness meter. The indicator scale was adjusted at zero for an initial load of 10 N, after which the load was gradually increased to 250 N (over a time of ~30 s) and kept constant for ~30 s. Then, the depth of impression (h_1) was measured, the sample was gradually unloaded (over a time of ~30 s), and the recovered impression depth (h) was measured. The error of the determination of h_1 and h values did not exceed 2 μm. The sample hardness H according to Rockwell was calculated using the formula

$$H = \frac{P}{\pi d h},$$

where P is the load applied to the ball indenter and d = 5 mm is the indenter diameter.

The samples were exposed to the action of a pulsed magnetic field having the form of trains of 150–6000 symmetric triangular pulses of the same polarity with a pulse width of τ = 10 μs and a pulse repetition rate of f = 50 Hz. The magnetic induction pulse amplitude B_0 was varied from 0.05 to 05 T. The magnetic field was generated using the periodic discharge of a capacitor energy store via a low-inductance coil and monitored by measuring the charging current in the main coil and the induction voltage in the probing coil.

The pulsed magnetic treatment (PMT) of samples was performed at room temperature. In some cases (e.g., for the PMT at B_0 = 0.4 and 0.5 T for 1–2 min),

1063-7850/05/3105-0364$26.00 © 2005 Pleiades Publishing, Inc.

the solenoid was heated and the sample temperature during the exposure increased by 8–10 K. However, the results of control measurements on the samples heated 10 K above room temperature for 10 min (without magnetic field application) showed that this heat treatment did not led to changes in the hardness.

During exposure to a magnetic field, the samples were oriented inside the coil so that the wood fibers were parallel or perpendicular to the field lines. The results of hardness measurements showed that the PMT effect was dependent on the sample orientation.

Figure 1 shows plots of the relative hardness H/H_0 versus amplitude B_0 of the pulsed magnetic field. The PMT duration for all samples was 60 s (which corresponded to $N = 3000$ pulses), and the measurements of H were performed 48 h after the PMT. The initial hardness of the pressed wood was $H_0 = 200$–300 MPa. The results of preliminary measurements showed that the hardness of samples after PMT exhibited relaxation for a certain time after the exposure, reached a maximum level 5–10 h after the treatment, and then ceased to change. Each experimental point in Fig. 1 is averaged over no less than seven samples.

As can be seen from the experimental data in Fig. 1, there is a certain threshold value ($B_0 = 0.2$ T) below which the magnetic field does not influence the wood hardness H. The maximum increase in the longitudinal (edge) hardness $H_\parallel$ was observed after the PMT at $B_0 = 0.3$ T and above. It is interesting to note that the PMT at $B_0 = 0.3$ T and above led to virtually the same increase in H/H_0, reaching up to 50% for some of the samples.

A rather insignificant increase in the transverse hardness $H_\perp$ was observed for the same samples processed under identical PMT conditions. It should be noted that an increase in the H value was observed only when the samples were oriented during the PMT with their fibers parallel to the field direction. For the mutually perpendicular orientation of wood fibers and the magnetic field, the PMT effect on the hardness was much lower (the edge hardness $H_\parallel$ increased by no more than 3–4%).

The PMT duration also influenced the edge and transverse H values achieved upon treatment. As can be seen from the data presented in Fig. 2, the optimum PMT duration is $t = 60$ s, which corresponds to $N = 3000$. Further increase in the PMT time virtually did not additionally increase the $H_\parallel$ and $H_\perp$ values of the wood samples.

Thus, the main conclusion following from our experimental data is that the PMT leads to a significant irreversible increase in the edge hardness $H_\parallel$ (up to 50%).

Plasticization and subsequent hydrostatic pressing of the wood result in considerable breakage of the network of lignin–carbohydrate bonds [8] and in the multiple rupture of chemical bonds in cellulose macromolecules. In particular, such a degradation with the formation of radicals and uncompensated electrons may lead to dehydration of cellulose upon radiation treatment [9].

In our opinion, the PMT produces a change in the spin state of electrons (singlet–triplet transitions) involved in the broken bonds, thus stimulating the formation of cross links between neighboring cellulose molecules. This leads to a significant decrease in the

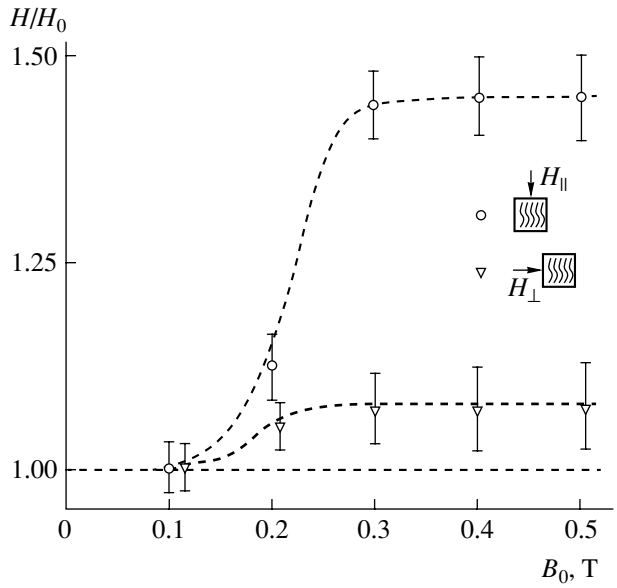

Fig. 1. Plots of the relative hardness H/H_0 versus pulsed magnetic field amplitude B_0 for pressed birch wood with $\rho = (1.35–1.45) \times 10^3$ kg/m^3 processed for 60 s ($N = 3000$). The hardness measurements were performed 48 h after the PMT.

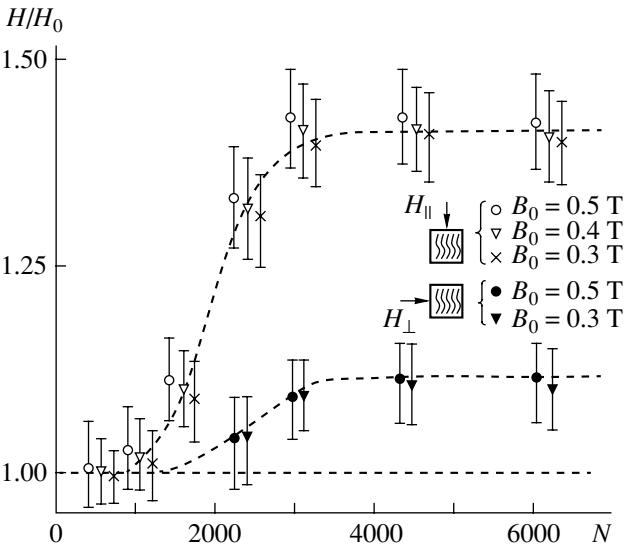

Fig. 2. Plots of the relative hardness H/H_0 versus PMT duration (number of pulses N) for pressed birch processed at various pulsed magnetic field amplitudes B_0. The hardness measurements were performed 48 h after the PMT.

mobility of molecular chains, especially in the longitudinal direction. It is also possible that the PMT favors restoration of the network of lignin–carbohydrate bonds broken upon plasticization and pressing, thus also increasing the edge hardness $H_{\parallel}$.

In conclusion, the PMT provides for an effective increase in the hardness of modified wood.

REFERENCES

1. N. I. Vinnik, *Modified Wood* (Lesnaya Promyshlennost, Moscow, 1984) [in Russian].
2. N. I. Klenkova, *Structure and Reaction Ability of Cellulose* (Nauka, Leningrad, 1976) [in Russian].
3. A. I. Kitaigorodskiĭ and D. Ya. Tsvankin, Vysokomol. Soedin., Ser. A **1**, 269 (1959).
4. N. N. Peschanskaya, V. Yu. Surovova, and P. N. Yakushev, Fiz. Tverd. Tela (Leningrad) **34**, 2111 (1992) [Sov. Phys. Solid State **34**, 1127 (1992)].
5. Yu. I. Golovin, R. B. Morgunov, and S. Yu. Liksutin, Vysokomol. Soedin., Ser. A **42**, 277 (2000).
6. M. N. Levin, V. V. Postnikov, and N. N. Matveev, Vysokomol. Soedin., Ser. A **45**, 217 (2003).
7. M. N. Levin, V. V. Postnikov, and N. N. Matveev, Zh. Fiz. Khim. **77**, 675 (2003).
8. P. P. Érin'sh and I. F. Kul'kevitsa, Khim. Drev., No. 5, 13 (1981).
9. V. A. Sharpatyĭ, A. A. Shapilov, and S. N. Pintelin, Khim. Fiz. **20** (12), 19 (2001).

Translated by P. Pozdeev

Technical Physics Letters, Vol. 31, No. 5, 2005, pp. 367–369. Translated from Pis'ma v Zhurnal Tekhnicheskoĭ Fiziki, Vol. 31, No. 9, 2005, pp. 20–25.

Bulk GaN Layers Grown on Oxidized Silicon by Vapor-Phase Epitaxy in a Hydride–Chloride System

Yu. V. Zhilyaev, S. D. Raevskiĭ, D. Z. Grabko, D. S. Leu, M. E. Kompan, Sh. A. Yusupova*, and M. P. Shcheglov

Ioffe Physicotechnical Institute, Russian Academy of Sciences, St. Petersburg, 194021 Russia
State University of Moldova, Kishinev, Moldova
Academy of Sciences of Moldova, Kishinev, Moldova
** e-mail: sh_yusupova@mail.ru*
Received December 10, 2004

Abstract—Bulk GaN layers with a thickness of up to 1.5 mm and a lateral size of 50 mm were grown by hydride–chloride vapor-phase epitaxy (HVPE). The best samples show a half-width (FWHM) of the X-ray rocking curve of $\omega_\theta = 27'$, a charge carrier density of $\sim 8 \times 10^{19}$ cm^{-3}, and a mobility of ~50 cm^2/(V s). The photoluminescence spectra of the obtained epitaxial GaN layers exhibit an edge emission band at 348 eV. The HVPE layers are characterized by a high mechanical strength: $H_V = 14$ GPa. © *2005 Pleiades Publishing, Inc.*

Introduction. Gallium nitride (GaN) has proved to be a promising semiconductor material for optoelectronics and acoustoelectronics, ensuring the manufacture of high-frequency devices capable of operating at high temperatures. In particular, highly effective LEDs and lasers were created on the bases of GaN, but the emitting structures were grown for the most part on sapphire and SiC substrates. Such structures are characterized by considerable residual stresses and large densities of defects caused by a misfit between the crystal lattice parameters and the thermal expansion coefficients of GaN layers and substrates. The residual stresses and defects negatively influence the efficiency and reliability of devices: they are the main source of problems encountered in the development and production of GaN-based devices. The best solution to these problems would be the use of intrinsic GaN substrates.

This study was aimed at obtaining thick epitaxial GaN layers of homogeneous thickness on standard 2-inch single crystal silicon wafers.

Experimental. Epitaxial layers (epilayers) of GaN were grown in a horizontal reactor by hydride–chloride vapor-phase epitaxy (HVPE) on oxidized silicon wafers SiO_2/Si(111) and on Al_2O_3(0001) sapphire substrates. In these experiments, we also studied the effect of the substrate rotation rate on the homogeneity of GaN epilayers. The initial substances were hydrogen, ammonia, gallium, and hydrogen chloride. The growth was effected in two steps: in the first stage, a buffer layer was grown at a substrate temperature of 800 K, and, in the second stage, the main GaN epilayer was grown at a higher temperature. In both stages, the source of gallium was maintained at 1120 K. The H_2/NH_3 flux ratio was ~2/1. The flow rate of ammonium was ~1 l/min, and the flow rate of HCl over liquid gallium was varied within 20–50 ml/min. The gaseous reactants were supplied to the growth zone via nozzles of different geometries and directed at various angles relative to the surface of a rotating substrate. The substrate was rotated by the hydrogen flow.

The synthesized GaN crystals were studied using optical and electron microscopy techniques. The crystal structure was studied by X-ray diffraction on a two-crystal diffractometer. The electric properties of epilayers were determined using the van der Pauw method. The mechanical strength was determined using a Vickers hardness meter.

Results and discussion. When GaN epilayers are grown by HVPE in a horizontal reactor, the reactive gases are usually supplied to the growth zone so that their flows are parallel to the substrate surface. Because of a high rate of the epitaxial growth of GaN, the concentration of the gallium-carrying component rapidly decreases upon mixing with ammonia. This leads to a sharp drop in the growth rate (and in the deposit thickness) along the flow. Considerable inhomogeneity of the layer thickness is also observed in the direction perpendicular to the gas flow. Use of a quartz tube with a rectangular cross section for the supply of one of the reactants (ammonia or gallium chloride) only partly levels the epilayer thickness in the transverse direction and does not improve the longitudinal situation. A decrease in the reactor cross section (for increasing the average gas flow velocity) at a constant supply of reactants, as well as a decrease in the ammonia-supplying nozzle cross section, also cannot provide for obtaining layers of homogeneous thickness in the longitudinal direction.

1063-7850/05/3105-0367$26.00 © 2005 Pleiades Publishing, Inc.

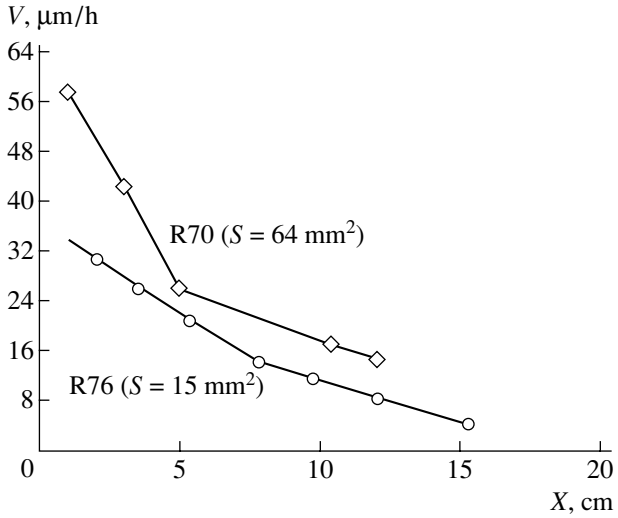

Fig. 1. Plots of the GaN growth rate (V) versus distance (X) from the ammonia-supplying nozzle edge for two samples (R70 and R76) grown using nozzles with different cross-section areas S.

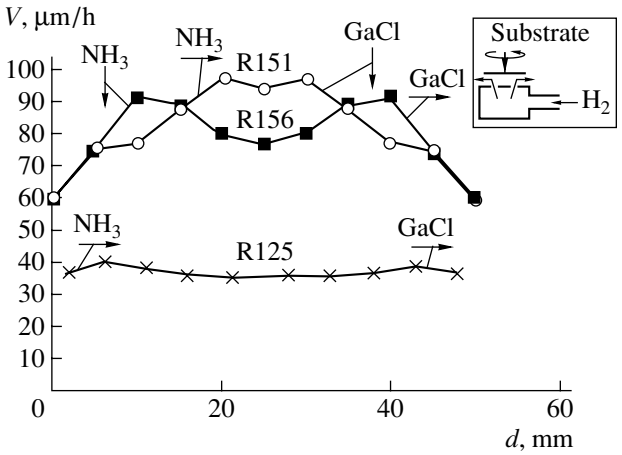

Fig. 2. The GaN growth rate profiles along the diameter of a rotating substrate for three samples (R151, R156, and R125) obtained using various geometries of the supply of reactants to the growth zone. The inset shows a scheme of substrate rotation in the hydrogen flow. See text for explanations.

Figure 1 shows plots of the GaN growth rate (V) versus distance (X) from the ammonia-supplying nozzle edge for a constant supply of H_2, NH_3, and HCl and a variable area (S) of the nozzle cross section. As can be seen, the curves consist of two nearly linear parts. The slope of the first part (corresponding to a region close to the nozzle edge) is somewhat greater and increases with the cross-section area S. This is explained by greater concentrations of reactants and, accordingly, higher growth rates near the nozzle. Then, a high reaction rate leads to depletion of the component (GaCl) with a lower concentration, which results in a sharp decrease in the GaN growth rate. When the nozzle area S is decreased, the NH_3 flow velocity grows and the slopes in the two parts of the $V(X)$ curve become closer to each other, but the average deposition rate decreases. The results of our investigation showed that, for a static arrangement of substrates in the horizontal reactor, even the most optimum conditions can provide for stabilization of the epilayer thickness only within 50% over a 50-mm distance along the gas flow.

More homogeneous layers are obtained when the substrates are rotated. Previously, this method was used to grow GaN on a mechanically rotated substrate in a vertical reactor [1]. In this study, the substrates were rotated by the hydrogen flow (see the inset in Fig. 2). This approach simplifies the reactor design and improves the product quality, since the substrate rotating on a gas cushion is less subject to vibrations detrimentally influencing the nucleation and growth.

Figure 2 shows the GaN growth rate profiles along the diameter of a rotating substrate for three samples obtained using various geometries of the supply of reactants to the growth zone. Sample R151 (with an epilayer thickness of 650 ± 90 μm) was grown using the NH_3 flow directed parallel to and the GaCl flow directed perpendicular to the substrate plane. For sample R156 (630 ± 70 μm), the flow of ammonia was perpendicular, while the flow of GaCl was parallel to the substrate. Sample R125 (150 ± 5 μm) was grown using both NH_3 and GaCl flows parallel to the substrate surface. As can be seen, the layer thickness variations relative to the average value for these samples are 14, 11, and 3.3%. Even when both reactant flows were directed perpendicular to the substrate, the thickness variations did not exceed 15%. Therefore, in all variants of the supply of reactants, the substrate rotation in the course of deposition provides for a significant increase in homogeneity of the GaN growth rate.

It was established that, at small rotation rates, the substrate plane exhibits oscillations relative to the gas flow that negatively influence the growth process. As a result, the GaN epilayer on a 2-inch substrate has a truncated ellipsoid profile. When the substrate rotation rate is increased to or above 120 rpm, the growth becomes more homogeneous and the layer thickness profiles are like those depicted in Fig. 2. In addition, an increase in the flow rate of hydrogen (rotating the substrate) above ~1 l/min leads to displacement of the reactants (GaCl and NH_3) from the substrate edge and prevents overgrowth of GaN at the edge. This results, on the one hand, in a reduction of the diameter of the deposited GaN layer and, on the other hand, in a decrease in the density of defects caused by roughness of the substrate edge.

The structural perfection of GaN epilayers grown on oxidized silicon substrates increases with the layer thickness. This tendency was observed previously [2] for GaN epilayers grown on sapphire substrates. We obtained GaN epilayers with thicknesses on the order of 1 mm on SiO_2/Si(111) substrates. The full width at

half maximum (FWHM) of the X-ray rocking curves of these deposits was $\omega_\theta \sim 1.5°$ for the samples grown in a 10-h cycle and $\omega_\theta \sim 4°$–$5°$ for the samples grown in a 5-h cycle. Therefore, the process of improvement of the crystal perfection of GaN epilayers is continued during the entire growth period.

We have determined a critical thickness of the GaN deposit (≤300 μm) for which the substrate–epilayer heterostructure does not exhibit fracture (as a result of the difference between thermal expansion coefficients of silicon and GaN) upon cooling. By etching off the silicon from such structures, it is possible to obtain GaN substrates for subsequent growth of GaN epilayers with a thickness of up to ~1.5 mm. Upon grinding and polishing, we obtained mirror-smooth GaN epilayers with a thickness of ~1 mm, which could be also used as substrates. These substrates are semitransparent and have a brown color characteristic of strongly doped GaN.

The electrical characteristics of GaN epilayers were determined using room-temperature Hall effect measurements. It was found that as-grown GaN substrates possess *n*-type conductivity with the charge carrier density of $\sim 8 \times 10^{19}$ cm^{-3} and a mobility of ~1 cm^2/(V s). After a 4-h annealing in ammonia at the growth temperature, the carrier density remained unchanged, while the mobility increased to ~20 cm^2/(V s). In bulk GaN layers grown on such substrates, the mobility amounted to ~50 cm^2/(V s). This increase in the carrier mobility in a bulk layer as compared to that in the annealed substrate is probably related to the sample prehistory involving healing of the homosubstrate and prolonged heating in ammonia during the growth cycle.

The photoluminescence spectra of the obtained GaN epilayers exhibit an edge emission band with a maximum near 3.48 eV. This band is typical of GaN crystals.

The mechanical properties of GaN epilayers were characterized by the Vickers method using an indenter loaded to within 0.25–1 N. The Vickers microhardness (H_V) was measured on the rear (buffer) and front sides of the samples. The scatter of H_V values over the sample surface fell within the accuracy of measurements, which was evidence of a high mechanical homogeneity of the obtained epilayers. The microhardness was ~12 GPa on the buffer side and ~14 GPa on the front side. The latter value was also characteristic of the polished bulk GaN layers. For all loads in the range employed, the indenter formed clear marks on the GaN surface, which was indicative of a high plasticity of the crystals studied.

Conclusion. We have demonstrated that bulk GaN epilayers with a homogeneous thickness of up to 1.5 mm can be obtained using a two-stage HVPE process on rotating 2-inch oxidized silicon wafers.

REFERENCES

1. R. J. Molnar, W. Götz, L. T. Romano, and N. M. Johnson, J. Cryst. Growth **178**, 147 (1997).
2. P. R. Tavernier, E. V. Etzkorn, Y. Wang, and D. R. Clarke, Appl. Phys. Lett. **77**, 1804 (2000).

Translated by P. Pozdeev

Technical Physics Letters, Vol. 31, No. 5, 2005, pp. 370–373. Translated from Pis'ma v Zhurnal Tekhnicheskoĭ Fiziki, Vol. 31, No. 9, 2005, pp. 26–34.

A Criterion for Electric Field Reversal in the Negative Glow Region of a Short DC Glow Discharge

A. A. Kudryavtsev* and N. E. Toinova

St. Petersburg State University, St. Petersburg, Russia

** e-mail: akud@ak2138.spb.edu*

Received December 23, 2004

Abstract—A theoretical analysis is performed and simple analytical formulas are obtained for estimating the position of the point of electric field reversal in a short (without the positive column) dc glow discharge. Using these formulas, the position of the reversal point can be approximately determined from tabulated published data on the ionization coefficients for fast electrons in the field. © *2005 Pleiades Publishing, Inc.*

The possible reversal of the sign of an axial electric field in the negative glow (NG) region of a dc glow discharge has been discussed in the literature for a long time [1, 2]. This phenomenon has been observed in experiment [3] and repeatedly demonstrated by the results of numerical simulations (see, e.g., [4, 5]). The position x_m of the point of field reversal (or the maximum plasma density) determines the fraction of ions going back to the cathode. Since the number of these ions is frequently greater than the number of ions generated in the cathode layer [6, 7], knowledge of x_m is necessary for correctly determining the conditions of self-sustained discharge.

Kolobov and Tsendin [6] developed a self-consistent analytical model with allowance for nonlocal ionization in the cathode region and pointed out that the situation is determined primarily by the ratio of the mean free paths Λ_f of fast electrons and the interelectrode distance L. However, explicit expressions for x_m were not obtained in [6]; moreover, an equation describing x_m (see [6, Eq. (42)]) contains an error and should not be used for calculations of this value.

Later, Boeuf and Pitchford [7] used an the expression for the self-consistent field [1] and obtained an analytical formula for x_m,

$$x_{mb} = d + \lambda/\ln\left(\frac{\lambda}{(L-d)}\left(1 - \exp\left(-\frac{(L-d)}{\lambda}\right)\right)\right), \quad (1)$$

where d is the cathode sheath length, L is the interelectrode distance, and λ is the scale of relaxation of the source of nonlocal ionization in the NG region ($x \geq d$). The latter source was approximately described [7] as

$$Z_b(x) = s_m \exp(-(x-d)/\lambda) = s_m a(x), \quad x \geq d. \quad (2)$$

Maric *et al.* [8] performed x_m calculations using formula (1) and obtained perfect coincidence with the results of simulations according to a model adopted for the glow discharge in argon. The values of the characteristic ionization length λ were determined from decay of the excitation rate profile in the NG region (i.e., from the results of a full-scale Monte Carlo simulation of the discharge with allowance for fast electrons). Unfortunately, since each particular case requires lengthy preliminary calculations, this approach does not allow the x_m value to be predicted for other discharge conditions. However, in principle, Monte Carlo simulations can be used to obtain approximate formulas describing λ for any gases or their mixtures. This approach was most consistently developed in [9], where the λ values were obtained for four gases (argon, helium, nitrogen, and silane) under anomalous discharge conditions, $pd < (pd)_n$. As for the other gases and discharge conditions, no data are available in the literature for estimation of the characteristic ionization length λ.

This paper presents an analysis of the field reversal conditions and gives simple analytical formulas for estimating the position of the point of reversal from well-known data [1, 2] on the field dependence of the Townsend ionization coefficients.

From the standpoint of physics, the field reversal is caused by nonlocal ionization in the plasma region with a low field strength, which is produced by high-energy (fast) electrons generated in the cathode sheath (see, e.g., [1–7]). A strong (exponential) dependence of the Townsend ionization coefficient α on the field to pressure ratio E/p,

$$\alpha/p = A\exp(-Bp/E) \quad (3)$$

(where A and B are constants tabulated for most gases [1, 2]), leads to instability of the cathode sheath that results in the formation of a cathode spot, in which the normal current density corresponds to "switching off" of the dependence of α on E/p [10]. In such field, the rate of ionization at a given point is determined by a

1063-7850/05/3105-0370$26.00 © 2005 Pleiades Publishing, Inc.

potential difference over the path traveled by fast electrons from the start point (rather than by the local field). Therefore, the ionization has a nonlocal character. This situation is usually described using the results of Monte Carlo simulations or by directly solving the kinetic equation. Unfortunately, the lack of reliable data for the complete set of cross sections of the elementary processes (in particular, their angular dependences) poses questions concerning the accuracy of such calculations.

In our analysis, fast electrons with energies $w \gg \varepsilon_i$ are described in terms of the drag force $F(w)$ so that the ionization characteristics are determined by the electron energies (i.e., by the electron energy distribution function) rather than by the local E/p ratio. According to the results of numerous calculations, $F(w)$ weakly varies with the electron energy for $w \le 1000$ eV and, hence, can be considered approximately constant (for more details, see [6, 10]). These conditions correspond to the point of inflection (saturation) of the dependence of α on E/p given by Eq. (3), which is achieved for $(E/p)_m = B$. The same condition approximately corresponds to the conditions of electron runaway [6, 10].

A fast electron with an initial energy corresponding to the cathode fall U_c travels a distance

$$\Lambda_f = eU_c/E_m = eU_c/(pB) \quad (4)$$

until the ionization capacity is completely exhausted. In a normal discharge, this distance corresponds to the point of minimum voltage on the Paschen curve [1, 10]. Note also that the Λ_f value determines the length $\Lambda_f - d$ of the NG plasma region [1, 6]. In the glow discharge, the distance Λ_f is greater than the cathode sheath length d and, hence, ionization in the plasma proceeds to a considerable extent in a nonlocal manner. At $x = \Lambda_f$, the most energetic electrons emitted from the cathode are stopped, and the Faraday dark space occurs to the right of this point (Fig. 1). Electrons generated in the NG plasma, where the field strength is small, are incapable of producing further ionization. Therefore, the ionization is determined entirely by the fast electrons arriving from the cathode sheath, and the ionization rate decays with the distance. This ionization source can be approximately described by relation (2), while rough estimates of the ionization length λ can be obtained using the formula

$$\lambda \approx \Lambda_f/2 = U_c/2pB, \quad (5)$$

which corresponds to a e^2-fold (i.e., approximately tenfold) decay of the intensity of source (2).

The magnitude and direction of a self-consistent field in the plasma are determined from the condition of quasi-neutrality. The ion current (dominating on the cathode) is transformed into the electron current (dominating in the regions far from the cathode) due to ionization. Since the nonlocal ionization in the plasma accounts for a considerable part of the total ionization in the entire cathode region [7, 8], the ion current from plasma to cathode sheath and then to cathode is on the order of the total discharge current. In contrast to the ion current in the cathode sheath, where the field is strong, the ion current in the NG plasma is transported by a relatively weak mechanism of ambipolar diffusion. Accordingly, the ion density gradient toward the cathode in the NG plasma must be large.

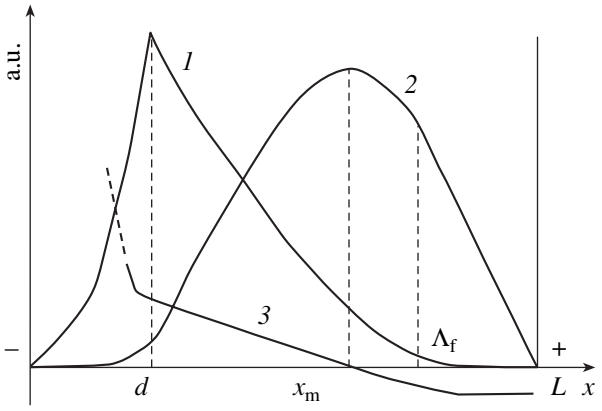

Fig. 1. Profiles of the (*1*) ionization source $Z(x)$, (*2*) plasma density $n(x)$, and (*3*) electric field strength $E(x)$ in a short dc glow discharge (see text for explanations).

In order to transfer a large ion current (accounting for a significant fraction of the total current), a deep plasma region at $x = x_m > d$ must exhibit a significant maximum in the ion density n_m, which has to be several orders of magnitude higher than the ion density in the sheath and in the positive column of the glow discharge. Then, if the ion density decay toward the anode is sufficiently steep, a reverse field (directed toward the anode) retarding the electron diffusion will appear at x_m (Fig. 1). Thus, a potential well for electrons is formed, whereas the motion of ions corresponds to ambipolar diffusion [1, 6]. The point of the maximum ion density corresponds, to within an insignificant shift (on the order of the ratio of ion and electron mobilities toward the anode, $b_i/b_e \ll 1$), to the point of field reversal [7]. This very condition was in fact used for determining x_m in [6, 7]. The proximity of the point of field reversal to the point of maximum ion density was observed both in experiment [3] and in model calculations [4, 5].

Thus, the problem of finding the point of field reversal is reduced to determining the point of maximum ion density in the plasma. In order to estimate the position of this point, let us proceed from the equation of ambipolar diffusion. Similar to [6, 7], we will consider the simplest case of a short discharge (without the positive column) between plane-parallel electrodes. For simple

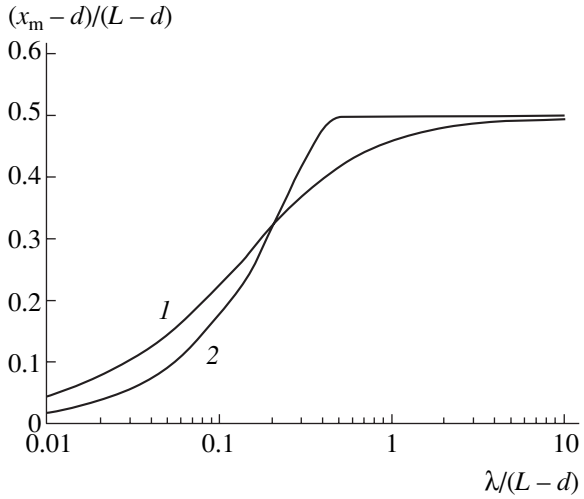

Fig. 2. Plots of the position of the point of field reversal determined using (*1*) formula (1) and (*2*) formulas (7) and (8) as functions of the $\lambda/(L–d)$ ratio.

single-component plasma with mobilities independent of the field and ion density, we obtain the equation

$$\frac{d}{dx}D_a\frac{dn}{dx} + Z(x) = 0, \qquad (6)$$

where $D_a = D_i(1 + T_e/T)$ is the coefficient of ambipolar diffusion and $Z(x)$ is the ionization source profile. The nonlocal character of ionization (i.e., the presence of fast electrons capable of producing ionization not only in the cathode sheath, but in the plasma as well) accounts for the nonzero source $Z(x)$ in Eq. (6) (Fig. 1). Most electrons are confined within the NG plasma region, and the electric field does not heat these electrons, so that the coefficient of ambipolar diffusion can be considered constant to the first approximation.

Since the ion density in the cathode and anode sheaths is relatively small, Eq. (6) can be solved with zero boundary conditions at the sheath–plasma interface and on the anode: $n(d) = n(L) = 0$. Then, the distribution $n(x)$ described by Eq. (6) has a maximum n_m, whereby ions formed at $x > x_m$ move toward the anode and those formed at $x < x_m$ return to the cathode (Fig. 1). The position of this maximum can be determined, provided that the ionization source profile $Z(x)$ is known. Substituting $Z(x)$ given by formula (2) into Eq. (6), we obtain the ion density profile in the plasma (described by [7, Eq. (19)]), with the position x_m of the maximum described by formula (1) (coinciding with that presented in [7]).

In order to simplify the problem, let us assume the ionization source in Eq. (6) to be constant, so that $Z(x) \approx Z_0 = \text{const}$ for $x \le \Lambda_f$ and $Z(x) = 0$ for $\Lambda_f < x < L$ [6]. Then, Eq. (6) yields for x_m a simple formula:

$$x_{mc} = \begin{cases} (2L\Lambda_f - \Lambda_f^2 - d^2)/(2(L-d)), & \Lambda_f \le L \\ (L+d)/2, & \Lambda_f \ge L \end{cases}. \qquad (7)$$

Using these expressions, one can readily estimate the position x_m of the plasma density maximum for the given values of d, L, and U_c using relations (1) and (5) (or (7) and (4)) in all gases for which published values of B are available (see, e.g., [1, 2]).

By virtue of the integral dependence, a solution to the diffusion equation is known to be weakly dependent on the shape of the source profile. For this reason, we may expect that x_m will weakly depend on $Z(x)$ in Eq. (6); that is, the results of calculations using formulas (7) and (1) will not differ significantly. In order to check this assumption and evaluate the possible errors, let us use the simplest relation (5) between λ and Λ_f. Curve *1* in Fig. 2 shows the ratio $(x_{mb} - d)/(L - d)$ as a function of $\Lambda = \lambda/(L - d)$, which reproduces [7, Fig. 1]. Using formula (7) with $d/L \ll 1$, we obtain the relation

$$(x_{mc} - d)/(L - d) \approx \begin{cases} 2\Lambda(1-\Lambda), & \Lambda \le 1/2 \\ 1/2, & \Lambda \ge 1/2 \end{cases}, \qquad (8)$$

which is depicted by curve *2* in Fig. 2.

For $\Lambda \ge 1/2$, curve *2* in Fig. 2 corresponds to the asymptotic behavior of a discharge whose breakdown and development corresponds to those described by the left branch of the Paschen curve ($\Lambda_f > L$). In this case, Eq. (6) gives a parabolic profile of the plasma density with the maximum

$$n_m = Z_0(L-d)^2/8D_a \qquad (9)$$

approximately in the middle of the discharge volume, that is, at $x_m = (L + d)/2$. According to formula (9), approximately half of the ions formed in the plasma return to the cathode, and the others are driven toward the anode. The same asymptotic value for x_m is given by formula (1) for $\lambda \gg L$.

If the interelectrode distance is relatively large, $L \gg \Lambda_f$, the point x_{mc} given by formula (7) approaches the boundary ($x_{mc} \approx \Lambda_f$) between the NG region and the Faraday dark space, and an increasing fraction of ions is returned from the plasma to the cathode. Accordingly, formula (1) with $\lambda \ll \Lambda$ gives the asymptotic behavior of $x_{mb} \approx d + \lambda/\ln((L - d)/\lambda)$, which corresponds to a somewhat lower value x_m as compared to x_{mc} given by formula (7).

As can be seen from Fig. 2, formulas (1) and (7) give close values of x_m in a broad range of conditions. Now, let us compare the estimates given by formulas (1), (5) and (7), (4) to the data reported in [4, 5] for a dc glow

Comparison of the results of calculations with the published data [5]

U_c, V	d, cm	x_m, cm	Λ_f, cm	x_{mb}, cm	x_{mc}, cm
125.8	0.59	0.86	0.7	0.75	0.68
124	0.44	0.63	0.69	0.66	0.63
123.9	0.4	0.6	0.69	0.63	0.62
138.9	0.34	0.34	0.77	0.53	0.58

discharge in argon with B = 180 V/(cm Torr) [1]. The results of simulations using a multibeam model (see [4, Fig. 10] for p = 0.6 Torr, L = 2 cm, d = 0.22 cm, and U_c = 300 V) give x_m = 1.02 cm. Under these conditions, formula (4) gives $\Lambda_f \approx 2.8$ cm > L, so that both x_{mb} = 1.05 cm and x_{mc} = 1.1 cm agree well with the results obtained in [4]. A comparison to the results of estimates obtained in [5] for p = 1 Torr and L = 1 cm (see the table) also show good coincidence for both x_{mb} and x_{mc}.

In order to use estimates according to simple formulas (1) and (7), it is necessary that the transverse size be relatively large, $R \gg \Lambda_f - d$, and the pressure not be too high, so that the characteristic length of the volume recombination $l_r = \sqrt{D_a \tau_r}$ would exceed the longitudinal size: $l_r \gg \Lambda_f - d$ (for $\tau_r = 1/(\beta n_e)$, where β is the recombination coefficient). In this case, the discharge is short (its length is insufficient to form a positive column) and the geometry can be considered one-dimensional.

Thus, we recommend the following procedure for approximately determining the point of field reversal in a short glow discharge (R, $l_r \gg L$). First, the mean free path of fast electrons $\Lambda_f = eU_c/(pB)$ is estimated using formula (4) for the given cathode fall U_c and tabulated B values in the approximate relation (3) between α and E/p. Then, the x_m value is estimated using formulas (7) or (1) and (5).

For the short dc glow discharges under consideration, it is necessary to take into account the following circumstances [6, 10]. The electron current can be subdivided into the diffusion and drift components only provided that the characteristic scale of the potential well for electrons (L–d) exceeds the characteristic length λ_ε of the energy relaxation of electrons [6]. Should the L–d value be smaller than λ_ε, the subdivision into diffusion and drift becomes senseless and a kinetic analysis becomes necessary. In atomic gases, $\lambda_\varepsilon \approx \lambda/\sqrt{2m/M} > 100\lambda$ and the condition L–$d > \lambda_\varepsilon$ is only satisfied for $pL > 10$ cm Torr. Unfortunately, most short glow discharges do not obey this condition.

Acknowledgments. The authors are grateful to L.D. Tsendin for fruitful discussions.

This study was supported by the US Civilian Research and Development Foundation for Independent Countries of the Former Soviet Union (CRDF project no. RP-1-567-ST-03). One of the authors (A.A.K.) also gratefully acknowledges support from the International Scientific–Technological Center (ISTC grant no. 3098).

REFERENCES

1. Yu. P. Raizer, *Physics of Gas Discharge* (Nauka, Moscow, 1992); Yu. P. Raizer and M. N. Schneĭder, Teplofiz. Vys. Temp. **29**, 1041 (1991).
2. A. von Engel, *Ionized Gases* (Fizmatgiz, Moscow, 1959; Clarendon Press, Oxford, 1965).
3. R. A. Gottscho, A. Mitchell, G. R. Scheller, *et al.*, Phys. Rev. A **40**, 6407 (1989).
4. M. Surendra, D. B. Graves, and G. M. Jellum, Phys. Rev. A **41**, 1112 (1990).
5. A. Fiala, L. C. Pitchford, and J. P. Boeuf, Phys. Rev. E **49**, 5607 (1994).
6. V. I. Kolobov and L. D. Tsendin, Phys. Rev. A **46**, 7837 (1992).
7. J. P. Boeuf and L. C. Pitchford, J. Phys. D **28**, 2083 (1995).
8. D. Maric, K. Kutasi, G. Malovic, *et al.*, Eur. Phys. J. D **21**, 73 (2002).
9. I. Pérès, N. Ouadoudi, L. C. Pitchford, and J. P. Boeuf, J. Appl. Phys. **72**, 4533 (1992).
10. A. A. Kudryavtsev and L. D. Tsendin, DC Glow Discharge, in *Encyclopedia of Low-Temperature Plasma*, Ed. by V. E. Fortov (Nauka, Moscow, 2000), Vol. 2, pp. 18–28.

Translated by P. Pozdeev

Technical Physics Letters, Vol. 31, No. 5, 2005, pp. 374–377. Translated from Pis'ma v Zhurnal Tekhnicheskoĭ Fiziki, Vol. 31, No. 9, 2005, pp. 35–42.

Eigenmode Geometry in a High-Birefringence Optical Fiber

A. N. Alekseev, A. V. Volyar*, and T. A. Fadeeva

Taurida National University, Simferopol, Ukraine

** e-mail: volyar@ccssu.crimea.ua*

Received December 6, 2004

Abstract—A new method for determining the weights of eigenmodes in a weakly multimode optical fiber with strong linear anisotropy is developed using the geometric approach. The proposed method is based on the measurement of geometric parameters of the lines of equal intensity (isolines) in the vicinity of a zero point of the field intensity distribution pattern at the output face of the fiber. Using this method, the weights of eigenmodes in a fiber have been determined upon computer processing of the experimental images of intensity distributions observed upon displacement of a probing laser beam relative to the center of the input face. The results are compared to theoretically calculated weights of the eigenmodes. © *2005 Pleiades Publishing, Inc.*

In recent years, single-mode optical fibers have been widely used in various fields of science and in numerous applications. The well-established technology of such fibers stipulates their use only in optical systems with parameters strictly corresponding to certain technical characteristics of the fibers. One of the most important restrictions is related to the wavelength of light transmitted via the fiber. Any significant deviations from a preset carrier wavelength not only lead to a sharp increase in the level of optical losses but also result in significant disturbances in the functioning of the entire system.

This circumstance is related to a change in the mode composition of radiation transmitted via the fiber. For example, an optical fiber with a waveguide parameter of $V = 2.1$ at a wavelength of $\lambda = 1.33$ μm is capable of guiding only the fundamental HE_{11} mode (provided that the fiber birefringence is ignored). However, the waveguide parameter at $\lambda = 0.63$ μm is $V = 4.4$, which implies that the fiber can maintain $N = 12$ eigenmodes (with allowance for the mode parity) [1]. The situation becomes even more complicated for birefringent fibers. In real cases, the energy of the beam at the input edge is nonuniformly distributed over the eigenmodes, while the "weights" of theses modes are related to the conditions of excitation of the fiber-optic system. Here, we encounter the old problem of "weighing" eigenmodes.

As long ago as in the beginning of 1970s, attempts were undertaken to measure the weights of eigenmodes at the fiber output face. These measurements were performed in most cases using complicated holographic masks positioned past the fiber [2]. The mask scattered part of the beam in a certain direction that corresponded to a given eigenmode. The resolution of this method and the accuracy of such measurements were very low. For this reason, it is a common practice to restrict mode weighing to a qualitative analysis of the mode composition of the field by comparing the intensity distribution in the output beam of classical optical fibers [3, 4] or fibers based on the photonic crystals [5] to the standard distribution. However, using a method proposed recently for the geometric analysis of the state of the core of optical vortices [6, 7], it is possible to develop a new geometric method for measuring the weights of eigenmodes in optical fibers.

This study was aimed at using a geometric analysis of the pattern of intensity distribution for determining the weights of eigenmodes in a weakly multimode optical fiber characterized by a strong linear anisotropy.

Below, we will consider a fiber characterized by high birefringence that provides a decrease in the number of propagating modes in the case of excitation by light linearly polarized along one of the anisotropy axes [1]. As is known [1, 8], the fields of eigenmodes in such a fiber can be expressed as

$$\begin{aligned}
\mathbf{e}_{tl}^{1,x} &= \hat{\mathbf{x}}\cos(l\varphi)F_l(R)\exp\{i\beta_l^{1,x}z\},\\
\mathbf{e}_{tl}^{2,x} &= \hat{\mathbf{x}}\sin(l\varphi)F_l(R)\exp\{i\beta_l^{2,x}z\},\\
\mathbf{e}_{tl}^{1,y} &= \hat{\mathbf{y}}\cos(l\varphi)F_l(R)\exp\{i\beta_l^{1,y}z\},\\
\mathbf{e}_{tl}^{2,y} &= \hat{\mathbf{y}}\sin(l\varphi)F_l(R)\exp\{i\beta_l^{2,y}z\},
\end{aligned} \tag{1}$$

where $\hat{\mathbf{x}}$, $\hat{\mathbf{y}}$ are the unit vectors of the linear polarization along the anisotropy axes of the fiber; l is the orbital mode index; $F_l(R)$ is the radial distribution function; $R = r/\rho$; r, φ, z are the cylindrical coordinates; ρ is the fiber core radius; β is the mode propagation constant; and the upper indices 1 and 2 in the notation of field components refer to the even and odd modes, respectively.

Consider a weakly multimode fiber with a waveguide parameter $V < 3.8$, in which only the modes with $l = 0.1$ can propagate. Let the index profile be par-

abolic, so that $F_l(R) = R^l \exp\{-VR^2/2\}$. If the fiber is excited by light linearly polarized along the x axis, the field at the output face can be expressed as

$$e_t = (a_0 \exp\{i\beta_0 z\} + a_1 X \exp\{i\beta_1 z\} + a_2 Y \exp\{i\beta_2 z\})\exp\{-VR^2/2\}, \quad (2)$$

where a_i are the weighing coefficients of modes, $X = r\cos(\varphi)/\rho$, and $Y = r\sin(\varphi)/\rho$. The pattern of intensity distribution comprises a point of zero field surrounded by lines of equal intensity (isolines) having an elliptical shape (Fig. 1a). The zero point (X_0, Y_0) can be found by equating field intensity (2) to zero, which yields the coordinates

$$X_0 = \frac{a_0}{a_1}\frac{\sin((\beta_0 - \beta_2)z)}{\sin((\beta_2 - \beta_1)z)}, \quad Y_0 = -\frac{a_0}{a_2}\frac{\sin((\beta_0 - \beta_1)z)}{\sin((\beta_2 - \beta_1)z)}. \quad (3)$$

As can be readily shown, the beam intensity distribution in the vicinity of the zero point is described by the expression

$$I = [a_1^2 X^2 + a_2^2 Y^2 + 2a_1 a_2 XY\cos((\beta_2 - \beta_1)z) + a_0^2 + 2a_0\{a_1 X\cos((\beta_0 - \beta_1)z) + a_2 Y\cos((\beta_0 - \beta_2)z)\}]\exp(-VR_0^2) = \text{const}, \quad (4)$$

where $R_0^2 = X_0^2 + Y_0^2$. Note that the equation $I(X, Y) = \text{const}$ describes an ellipse with the ellipticity $Q = a/b$ (a and b are semiaxes) and the axes making an angle ψ with the axes of the laboratory coordinate system (Fig. 1a).

Upon transition to a system of coordinates (X', Y') with the axes parallel to the axes of the ellipse and the origin coinciding with the point of zero intensity, the above equation can be written in the canonical form

$$A^2 X'^2 + B^2 Y'^2 = C^2 = \text{const}, \quad (5)$$

where

$$A^2 = a_1^2\cos^2\psi + a_2^2\sin^2\psi + a_1 a_2\cos((\beta_2 - \beta_1)z)\sin(2\psi),$$
$$B^2 = a_1^2\sin^2\psi + a_2^2\cos^2\psi - a_1 a_2\cos((\beta_2 - \beta_1)z)\sin(2\psi), \quad (6)$$

$$\tan(2\psi) = \frac{2a_1 a_2}{a_1^2 - a_2^2}\cos((\beta_2 - \beta_1)z), \quad (7)$$

$a = C/A$, and $b = C/B$. After simple transformations, we obtain the following expressions for the mode amplitudes (to within a constant factor):

$$a_1 = (\sin^2\psi + Q^2\cos^2\psi)^{1/2}, \quad a_2 = (Q^2\sin^2\psi + \cos^2\psi)^{1/2}, \quad (8)$$

and, for the cosine of the phase difference,

$$\cos((\beta_2 - \beta_1)z) = \frac{\sin(2\psi)(Q^2 - 1)}{[(1 + Q^4)\sin^2(2\psi) + 4Q^2(\cos^4\psi + \sin^4\psi)]^{1/2}}. \quad (9)$$

Using simple geometric considerations (Fig. 1a), we also readily obtain expressions for the amplitude a_0 and

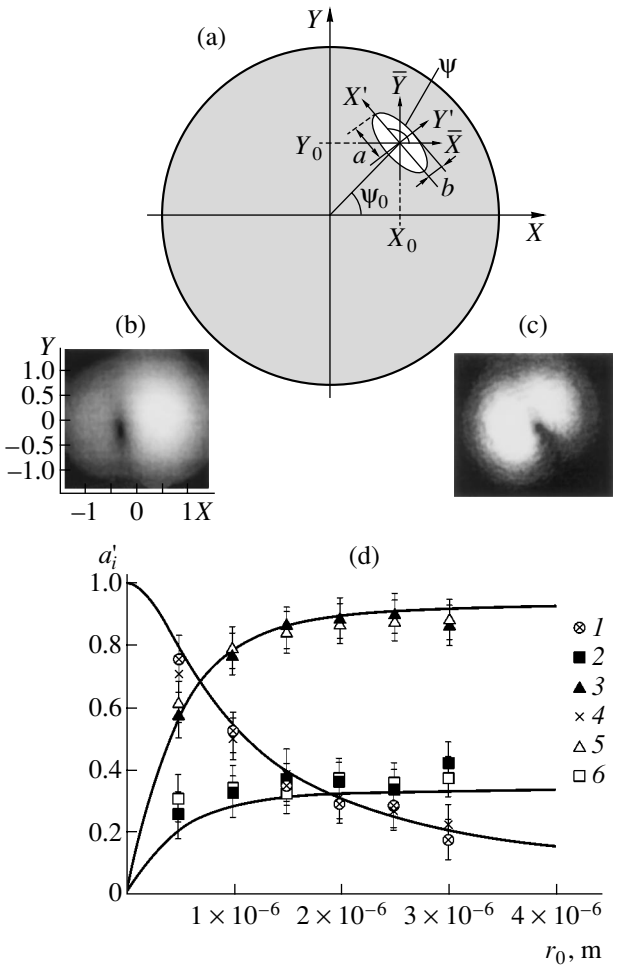

Fig. 1. Radiation intensity distribution in the output face of an optical fiber: (a) schematic diagram; (b) calculated pattern ($r_0 = 2$ μm); (c) measured pattern ($r_0 = 2$ μm); (d) plots of the mode weights (excitation coefficients) a_i' versus laser beam displacement r_0 relative to the center of the input face for a_0' (*1*, *4*), a_1' (*2*, *5*), and a_2' (*3*, *6*) measured (points) and calculated (curves) for the input polarizer set at α = 110° (*1*–*3*) and 20° (*4*–*6*).

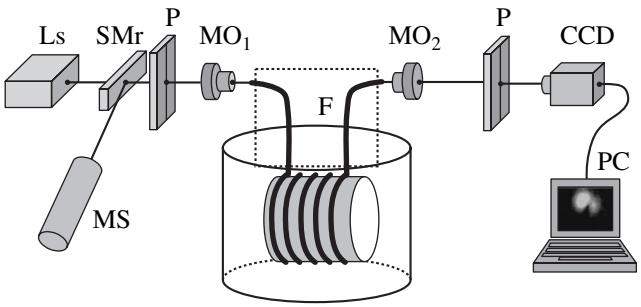

Fig. 2. Schematic diagram of the experimental setup: (Ls) He–Ne laser; (SMr) semitransparent mirror; (P) polarizers; ($MO_{1,2}$) 20^x and 8^x microobjectives, respectively; (F) optical fiber fixed in a thermostat; (MS) side-view microscope; (CCD) charge-coupled device camera; (PC) personal computer.

the phase difference of the fundamental mode:

$$a_0 = \frac{R_0 a_2 \sin((\beta_2 - \beta_1)z)}{\sin((\beta_0 - \beta_1)z)} \sin\psi_0, \tag{10}$$

$$\cot((\beta_0 - \beta_1)z) = \frac{a_1}{a_2} \frac{\cot\psi_0}{\sin((\beta_2 - \beta_1)z)} + \cot((\beta_2 - \beta_1)z). \tag{11}$$

The parameters a_0, ψ_0, Q, and ψ can be directly measured in experiment.

Now let us obtain expressions for the coefficients of excitation of the eigenmodes. Let the optical fiber be excited by a Gaussian beam shifted by $r_0 = (x_0, y_0)$ relative to the center. The mode excitation coefficients are defined as [1, 9]

$$a_i^{x,y} = \int_{S_\infty} E_l^{x,y} (e_l^{i,x(y)})^* dS / \int_{S_\infty} \left| e_t^{i,x(y)} \right|^2 dS. \tag{12}$$

Assuming that the field of the beam launched into the fiber is $E_t^x = \hat{\mathbf{x}} \exp\{-r'^2/(2\rho_g^2)\}$, where $r'^2 = (x - x_0)^2 + (y - y_0)^2$, and ignoring small optical losses in the fiber and partial redistribution of the mode energy caused by diffraction at the output face, the weights of the eigenmodes can be expressed as

$$a_0 = \frac{2\rho_g^2}{\rho^2/V + \rho_g^2} \exp\left\{-\frac{x_0^2 + y_0^2}{2} \frac{1}{\rho^2/V + \rho_g^2}\right\},$$

$$a_1 = \frac{4x_0 \rho \rho_g^2}{(\rho^2/V + \rho_g^2)^2} \exp\left\{-\frac{x_0^2 + y_0^2}{2} \frac{1}{\rho^2/V + \rho_g^2}\right\}, \tag{13}$$

$$a_2 = \frac{4y_0 \rho \rho_g^2}{(\rho^2/V + \rho_g^2)^2} \exp\left\{-\frac{x_0^2 + y_0^2}{2} \frac{1}{\rho^2/V + \rho_g^2}\right\}.$$

Figure 1b shows the pattern of intensity distribution calculated using formulas (2) and (13) for a Gaussian beam shifted to $r_0 = 2$ μm.

The experiments were performed using the setup schematically depicted in Fig. 2. The beam of a He–Ne laser ($\lambda = 0.63$ μm) passes through a polarizer and enters via a 20^x microobjective into an optical fiber with $V = 2.8$, a core radius of 3.5 μm, a length of 1 m, and a relatively high birefringence ($n_x - n_y \sim 10^{-4}$). Another (8^x) microobjective forms a projection of the fiber output face onto the entrance window of a CCD camera. The image formed by this camera is processed and displayed on a computer monitor. In order to eliminate random noise, the fiber was rigidly fixed in a thermostat. The input polarizer was adjusted so as to provide maximum polarization at the fiber output, which was evidence that the light was polarized parallel to the anisotropy axis. In our system, this corresponded to an angle of 20° and 110° relative to the vertical axis. The output polarizer was adjusted to the maximum intensity and blocked a small component polarized in the transverse direction, which appeared as a result of mode conversion in the fiber [1].

We have measured redistribution of the weights of eigenmodes when the laser beam spot on the input face was shifted along the vertical and horizontal axes. The beam and fiber axes coincided to within 2°. The laser beam displacement was monitored with the aid of a side-view microscope. The measurements were performed with the input polarizer set, as described above, to 20° and 110° relative to the vertical axis.

Figure 1c shows the typical pattern of the intensity distribution at the fiber output. Theoretical calculations were performed for the fiber and radiation parameters corresponding to those used in the experiment. As can be seen, the results of theoretical calculations (Fig. 1b) satisfactorily agree with the experimental pattern. The image of the output beam intensity distribution was processed using a special program (written in Delphi), which determined the parameters of the elliptic isoline and calculated the mode weights according to formulas (8) and (10).

Figure 1d presents plots of the normalized mode weights versus displacement r_0 of the laser beam on the input face. Solid curves show the results of calculations using formulas (13). As can be seen, the weight of the fundamental mode decreases with increasing r_0, whereas the weights of higher modes ($l = 1$) increase. Small deviations of the experimental data from theoretical cures are probably related to a mismatch between the laser beam and the fiber axes, the optical losses in the waveguide channel, and the partial energy redistribution as a result of the anisotropic diffraction of eigenmodes in the output face. Switching the shift from vertical to horizontal leads to a symmetric change of the curves for the coefficients a_1' and a_2'.

In conclusion, it should be noted that, using the proposed method of measurement of the weights of eigenmodes in anisotropic fibers, it is possible to perform an analysis of the radiation field on a substantially new level. This approach allows us to pass from a qualitative comparison of the patterns of intensity distribution to the quantitative determination of the mode weights. In determining the geometric parameters of isolines, it is not necessary to take into account the nonlinear sensitivity of photodetectors with respect to the light intensity, which significantly decreases the uncertainty of measurements. The proposed method can be used for the creation of transducers of physical characteristics based on anisotropic optical fibers.

REFERENCES

1. A. W. Snyder and J. D. Love, *Optical Waveguide Theory* (Chapman and Hall, London, 1983).
2. D. I. Mirovitskiĭ, I. F. Budagyan, and V. F. Dubrovin, *Microwave Optics and Holography* (Nauka, Moscow, 1983) [in Russian].
3. K. F. Barrell and C. Pask, J. Opt. Soc. Am. **69**, 294 (1979).
4. F. Dubois, F. Emplit, and O. Hugon, Opt. Lett. **19**, 433 (1994).
5. P. S. Westbrook, B. J. Eggletton, R. S. Windeler, *et al.*, IEEE Photonics Technol. Lett. **12**, 495 (2000).
6. A. V. Volyar, Yu. A. Egorov, A. F. Rubass, and T. A. Fadeeva, Pis'ma Zh. Tekh. Fiz. **30** (16), 82 (2004) [Tech. Phys. Lett. **30**, 701 (2004)].
7. A. F. Rubass, A. N. Alexeyev, V. S. Latysheva, and A. V. Volyar, in *Proceedings of the International Conference on Advanced Optoelectronics and Lasers (CAOL'2003), Alushta, 2003*, Vol. 2, pp. 57–58.
8. K. N. Alekseev, A. V. Volyar, and T. A. Fadeeva, Opt. Spektrosk. **93**, 639 (2002) [Opt. Spectrosc. **93**, 588 (2002)].
9. A. V. Volyar and T. A. Fadeeva, Pis'ma Zh. Tekh. Fiz. **22** (17), 69 (1996) [Tech. Phys. Lett. **22**, 719 (1996)].

Translated by P. Pozdeev

Technical Physics Letters, Vol. 31, No. 5, 2005, pp. 378–380. Translated from Pis'ma v Zhurnal Tekhnicheskoĭ Fiziki, Vol. 31, No. 9, 2005, pp. 43–49.

Broadband Quasi-Total Autocollimation Cross-Polarization Wave Transformation

A. P. Kusaykin, P. N. Melezhik, and A. E. Poyedynchuk

Usikov Institute of Radiophysics and Electronics, National Academy of Sciences of Ukraine, Kharkov, Ukraine

e-mail: ire@ire.kharkov.ua

Received September 15, 2004

Abstract—The problem of diffraction of plane *E*- and *H*-polarized waves on a chiral layer supported on a periodic reflective grating composed of rectangular metal rods is solved using the methods of reexpansion and generalized scattering matrices. The diffraction on this structure is accompanied by quasi-total autocollimation cross-polarization wave transformation in a broad frequency band. *© 2005 Pleiades Publishing, Inc.*

Much attention in modern microwave technologies is devoted to the creation of new composite materials exhibiting the properties of chiral media, such as the ability to produce polarization transformation. In the last three decades, the phenomenon of electromagnetic chirality and the chiral materials were extensively studied in a number of applications for a broad (from decimeter to millimeter) range of wavelengths [1, 2]. In particular, such materials have been used for the development of polarization converters and for the creation of low-reflection coatings [3]. On the other hand, also extensively studied and widely used are diffraction gratings of various types, which exhibit a number of unique resonance properties [4, 5]. One such property is the phenomenon of nonspecular reflection of plane waves.

Previously, we obtained for the first time exact solutions to the problem of wave diffraction on a structure of the chiral layer–grating type [6, 7], which allowed us to discover the phenomenon of nonspecular, nearly total reflection of waves with a polarization transformation exhibiting a pronounced resonance character. In this context, it was of considerable interest to study the electromagnetic properties of a structure comprising a chiral layer supported on a reflective diffraction grating composed of rectangular rods (Fig. 1). This paper presents the results of the solution of the problem of plane wave diffraction on such a structure.

The vector problem of wave diffraction was solved using the methods of reexpansion and generalized scattering matrices. Since a chiral layer mutually relates the waves with different polarizations, application of the method of generalized scattering matrices makes it necessary to solve the problem separately for the diffraction of plane *E*- and *H*-polarized waves on the chiral layer and on the grating. The solution of such problems is described in detail elsewhere [6]; hence, we only outline below the formulation of the problem.

Consider the diffraction of a plane *E*-polarized wave of unity amplitude incident at an angle φ on an isotropic chiral layer infinite in the *OX* and *OY* directions. The layer material is characterized by relative permittivity ε, relative magnetic permeability μ, chirality parameter γ, and thickness h_2. Let the chiral layer be supported on a periodic reflective grating composed of rectangular metal rods. The grating is characterized by the groove depth h_1, groove width d, and period l (Fig. 1). In the incident wave, the electric vector E is assumed to be perpendicular to the plane of Fig. 1.

The reflection and transmission coefficients for the wave incident on the chiral layer were determined upon representing the material equations in the following form [2]:

$$\mathbf{D} = \varepsilon\varepsilon_0\mathbf{E} + i\gamma\sqrt{\varepsilon_0\mu_0}\mathbf{H},$$

$$\mathbf{B} = \mu\mu_0\mathbf{H} - i\gamma\sqrt{\varepsilon_0\mu_0}\mathbf{E},$$

were ε_0 and μ_0 are the permittivity and permeability of vacuum, respectively, and the time dependence is selected in the form of exponent $\exp(-i\omega t)$. The field

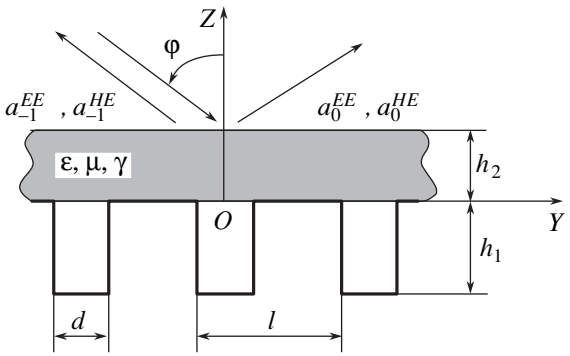

Fig. 1. Schematic diagram illustrating formulation of the diffraction problem (see text for explanations).

1063-7850/05/3105-0378$26.00 © 2005 Pleiades Publishing, Inc.

inside the chiral layer can be described in terms of a superposition of plane circularly polarized waves:

$$\mathbf{E} = \mathbf{E}^+ + \mathbf{E}^-, \quad \mathbf{H} = -\frac{i}{\rho}(\mathbf{E}^+ - \mathbf{E}^-),$$

where $\rho = \rho_0\sqrt{\mu/\varepsilon}$ and $\rho_0 = \sqrt{\mu_0/\varepsilon_0}$. The waves are characterized by the propagation constants $k^\pm = k_0\sqrt{\varepsilon\mu}\,(1 \pm \eta)$, where $\eta = \gamma/\sqrt{\varepsilon\mu}$ is the relative chirality and $k_0 = \omega\sqrt{\varepsilon_0\mu_0}$.

The diffraction field components are determined from the Maxwell equations and expressed in terms of the electric ($E_x(y, z)$) and magnetic ($H_x(y, z)$) fields. Taking into account that the diffraction field must obey the conditions of quasi-periodicity and radiation at infinity, the E_x and H_x components outside the scattering structure can be represented as follows:

$$E_x = e^{i(k_0^y y - k_0^z z)} + \sum_{n=-\infty}^{\infty} a_n^{EE} e^{i(k_n^y y + k_n^z z)},$$

$$H_x = \sum_{n=-\infty}^{\infty} a_n^{HE} e^{i(k_n^y y + k_n^z z)} \quad (z > 0),$$

where $k_n^y = 2\pi(n + \kappa\sin\varphi)/l$ and $k_n^z = 2\pi\sqrt{\kappa^2 - (n + \kappa\sin\varphi)^2}/l$ are the propagation constants of the nth spatial harmonic along the OY and OZ axes, respectively; $\kappa = l/\lambda$; l is the grating period; λ is the wavelength of the incident wave in the free space; a_n^{EE} are the unknown coefficients of transformation of the incident E-polarized field into the reflected E-polarized field; and a_n^{HE} are the coefficients of transformation of the incident E-polarized field into the reflected H-polarized field.

The problem of diffraction of the plane H-polarized wave is formulated using analogous considerations, and the corresponding unknown coefficients are denoted a_n^{HH} for the transformation of the incident H-polarized field into the reflected H-polarized field and a_n^{EH} for the transformation of the incident H-polarized field into the reflected E-polarized field.

By their physical meaning, the coefficients a_n represent the complex amplitudes of plane waves (harmonics) of the spatial spectrum of a field over the scattering structure. The angle φ_n at which the wave of the spatial spectrum leaves the structure is determined by the relation $\sin\varphi_n = -n/\kappa - \sin\varphi$. The regime in which one of the spectral harmonics propagates in the direction opposite to that of the incident wave is called the autocollimation regime (Littrow's mounting). This regime is a partial case of the nonspecular wave reflection. The autocollimation condition for the nth harmonic reflection is $\kappa\sin\varphi = -n/2$.

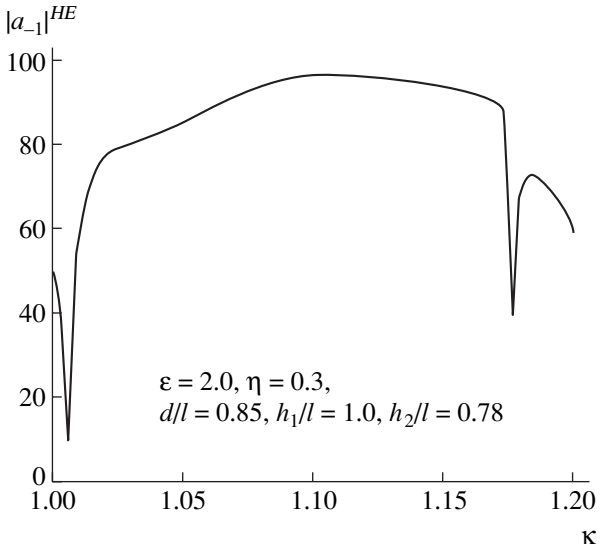

Fig. 2. A plot of the CPWT coefficient versus frequency of an E-polarized incident wave.

In order to solve the problem of plane polarized wave diffraction on the chiral layer–grating structure, we used the method of generalized scattering matrices extended so as to apply to the case of the vector problem under consideration. As a result, we obtained a system of linear algebraic equations of second order with respect to the unknown coefficients a_n. This allowed effective numerical algorithms to be constructed and an optimized search to be performed for a regime of quasi-total autocollimation cross-polarization wave transformation (CPWT) in a broad band of wavelengths. By the quasi-total autocollimation CPWT, we imply a regime in which the moduli of the coefficients a_n^{HE} and a_n^{EH} under autocollimation conditions are not smaller than 90%.

The results of the search for such a regime for the (–1) harmonic of the spatial spectrum are presented in Figs. 2 and 3 (where the transformation coefficients are expressed in percents). The autocollimation condition for this harmonic is $\kappa\sin\varphi = 0.5$. As can be seen from Fig. 2, there are certain parameters of the grating and the chiral layer such that the incident E-polarized wave is transformed into a reflected H-polarized wave within a frequency bandwidth greater than 15% (on a 50% level of the transformation coefficient). For the transformation of the H-polarized incident wave into a reflected E-polarized wave (Fig. 3), the frequency bandwidth (on the same transformation efficiency level) is greater than 10%. It should be noted that the level of the CPWT at the maxima reaches 96% for the E-polarized incident wave and 97% for the H-polarized wave.

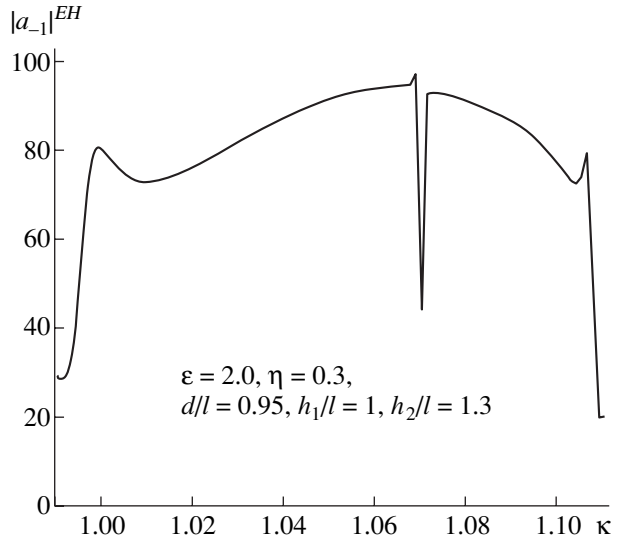

Fig. 3. A plot of the CPWT coefficient versus frequency of an *H*-polarized incident wave.

An analogous effect of quasi-total CPWT in the autocollimation regime was observed for the spectral harmonics with $|n| > 1$. As the harmonic number $|n|$ increases, the width of the frequency band in which the effect is manifested decreases.

The high-*Q* resonance maxima and minima of the CPWT coefficients a_n^{HE} and a_n^{EH} (see Fig. 2, the points at $\kappa = 1.01$ and 1.18; Fig. 3, the point at $\kappa = 1.07$) are related to the so-called confined mode resonance [4]. These are half-wave resonances with respect to the grating depth for the higher modes (above $n = 1$ for the *E*-polarized wave and above $n = 0$ for the *H*-polarized wave) in plane-parallel waveguides represented by grooves of the grating. The parameters of the scattering structure can be optimized so as to enhance these resonances either at the edge (Fig. 2) or in the middle (Fig. 3) of the corresponding frequency band. In the former case, it is possible to create a broadband polarization converter, while, in the latter case, it is possible to construct a device measuring the parameters of chiral layers.

To summarize, we have constructed a strict solution of the problem of diffraction for plane *E*- and *H*-polarized waves on a chiral layer supported on a periodic reflective grating composed of rectangular metal rods. Based on this solution, we discovered the phenomenon of quasi-total autocollimation cross-polarization wave transformation in a broad band of frequencies of the incident wave.

REFERENCES

1. A. Lakhtakia, V. K. Varadan, and V. V. Varadan, *Time-Harmonic Electromagnetic Fields in Chiral Media* (Springer-Verlag, Berlin, 1989).
2. I. V. Lindell, A. H. Sihvola, S. A. Tret'yakov, and A. J. Viitanen, *Electromagnetic Waves in Chiral and Bi-isotropic Media* (Artech House, Boston, 1994).
3. S. A. Tret'yakov, Radiotekh. Élektron. (Moscow) **39**, 1470 (1994).
4. V. P. Shestopalov, A. A. Kirilenko, S. A. Masalov, and Yu. K. Sirenko, *Resonant Scattering of Waves*, Vol. 1: *Diffraction Gratings* (Naukova Dumka, Kiev, 1986) [in Russian].
5. *Electromagnetic Theory of Gratings*, Ed. by R. Petit (Springer-Verlag, Berlin, 1980).
6. O. P. Kusaykin and A. Y. Poyedynchuk, Microwave Opt. Technol. Lett. **33**, 462 (2002).
7. S. B. Panin and A. Y. Poyedynchuk, in *Proceedings of the URSI–EMTS International Symposium on Electromagnetic Theory, Pisa, 2004*, pp. 1011–1013.

Translated by P. Pozdeev

Technical Physics Letters, Vol. 31, No. 5, 2005, pp. 381–384. Translated from Pis'ma v Zhurnal Tekhnicheskoĭ Fiziki, Vol. 31, No. 9, 2005, pp. 50–57.

Effect of the Carbon Isotope Composition on the Properties of Diamond

M. N. Magomedov

Institute for Geothermal Research, Dagestan Scientific Center, Russian Academy of Sciences, Makhachkala, Dagestan, Russia

e-mail: mahmag@xtreem.ru

Received November 1, 2004

Abstract—Parameters of the interatomic interaction potential for ^{12}C and ^{13}C carbon isotopes in the crystal lattice of diamond have been determined. Based on these data, the isotope dependence of the properties of diamond such as the Debye temperature, molar heat capacity, thermal expansion coefficient, vacancy formation energy, self-diffusion activation energy, surface energy, and longitudinal sound velocity is described. This approach is used for estimating a change in the bulk compression modulus of lithium crystals upon the passage from ^{7}Li to ^{6}Li. As the temperature increases, the isotope dependence of the heat capacity at constant volume vanishes; at a certain temperature, the isotope dependence of the thermal expansion coefficient changes from growth to decay. The expected isotope dependence of the parameters of phase transitions is predicted. It is shown that carbon condensates formed upon deposition from the gas phase must be enriched with the heavy isotope. © *2005 Pleiades Publishing, Inc.*

The influence of isotope composition on the properties of crystals has been studied for a long time, but it is still unclear which properties are subject to strong variations and which are independent of the average atomic mass in the bulk. In order to elucidate this issue, it is necessary primarily to determine differences in the interatomic interactions between various isotopes. This paper is devoted to an analysis of this problem in the case of diamond. Diamond was selected for two reasons: (i) availability of reliable experimental data and (ii) relatively strong interatomic interaction (two to three orders of magnitude greater than the energy of zero-point oscillations), which substantially simplifies calculations of the parameters of interatomic interactions.

Let us describe the pair interactions between carbon atoms in diamond in terms of the Mie–Lennard-Jones potential [1–5],

$$\varphi(r) = [D/(b-a)][a(r_0/r)^b - b(r_0/r)^a] = [D/(b-a)]\{a[r_0/(c+r')]^b - b[r_0/(c+r')]^a\}, \quad (1)$$

where D is the potential well depth; r_0 is the coordinate of the potential well minimum; a and b are the parameters characterizing rigidity and range of the potential, respectively; and c is the distance between the centers of nearest-neighbor atoms in the crystal lattice. Various methods were proposed for self-consistent determination of the total set of four parameters (see, e.g., reviews [4, 5]). Since the energy of zero-point oscillations in diamond is two to three orders of magnitude lower than the energy of interatomic bonds, the parameters of potential (1) can be determined to a good approximation using the following expressions [1–7]:

$$r_0 = c_{00} = (6k_yV_{00}/\pi N_A)^{1/3};\ D = 18B_{00}V_{00}/(k_nabN_A);\ b = 6\gamma_0 - 2;\quad a = 3[B'(P)_{00} - 2] - b, \quad (2)$$

where V is the molar volume of the crystal; N_A is the Avogadro number; k_n and k_y are the first coordination number and the packing coefficient (for diamond, $k_n = 4$ and $k_y = 0.3401$); γ_0 is the Grüneisen parameter at zero pressure and room temperature; $B'(P) = \partial B/\partial P$ is the pressure derivative of the isothermal bulk compression modulus; and the quantities with the 00 subscript refer to zero temperature and pressure ($T = 0$ K; $P = 0$).

According to the available experimental data, the distance $c_0^*(X)$ between the centers of nearest neighbor carbon atoms and the bulk compression modulus $B_0^*(X)$ of diamond vary depending of the atomic fraction $X = [^{13}C]/([^{12}C] + [^{13}C])$ of the ^{13}C isotope as described by the relations

$$c_0^*(X) = (1 - \Delta_C X);\quad B_0^*(X) = (1 + \Delta_B X). \quad (3)$$

In these relations, the coefficients according to the data

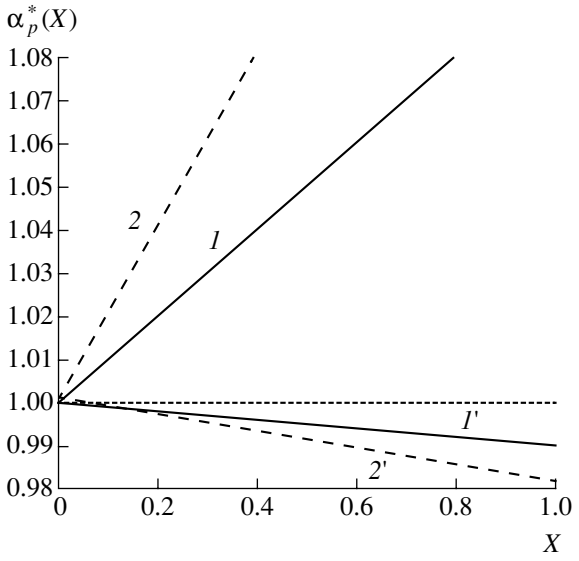

Plots of the relative thermal expansion coefficient α_p^* of (*1*, *1*') diamond and (*2*, *2*') lithium crystals versus the atomic fraction *X* of heavier isotope: (*1*, *2*) at low temperatures $T \ll \Theta_0$, $\alpha_p^*(X)_{\text{low}} \cong (1 + \Delta_m X)^{3/2}/[(1 + \Delta_B X)^{5/2}(1 - \Delta_C X)^{9/2}]$; (*1*', *2*') in the high-temperature limit $T \gg \Theta_0$, $\alpha_p^*(X)_{\text{high}} \cong 1/[(1 + \Delta_B X)(1 - \Delta_C X)^3]$. The calculations were performed for $\Delta_m = 0.0833$ (C) and 0.1667 (Li); $\Delta_C = 1.5 \times 10^{-4}$ (C) and 5×10^{-4} (Li); and $\Delta_B = 0.01$ (C) and 0.02 (Li).

of various researchers are as follows:

$$\Delta_C = \begin{cases} 1.486 \times 10^{-4} \\ \text{(Hollowey } \textit{et al.}\text{, 1991 [8])}; \\ 1.962 \times 10^{-4} \\ \text{(Gillet } \textit{et al.}\text{, 1999 [9])}; \\ (1.486\text{–}2.52) \times 10^{-4} \text{ (Plekhanov, 2003 [10])}. \end{cases} \quad (4)$$

$$\Delta_B = \begin{cases} 17 \times 10^{-2} \\ \text{(Hurley } \textit{et al.}\text{, 1994 [11])}; \\ -1.8 \times 10^{-2} \\ \text{(Gillet } \textit{et al.}\text{, 1999 [9])}; \\ (0.12\text{–}0.18) \times 10^{-2} \text{ (Plekhanov, 2003 [10])}.. \end{cases} \quad (5)$$

The functions with asterisks represent reduced values defined as $F^*(X) = [F(\text{C})/F(^{12}\text{C})] = [F(X)/F(0)]$.

According to the same data [8–11], the quantities $B'(P) = 4$ and $\gamma_0 = 1$ are independent of the isotope composition of diamond (i.e., $b = 4$ ad $a = 2$). Using these results and Eqs. (2) and (3), the remaining parameters as functions of the ^{13}C isotope content are given by the expressions

$$\begin{aligned} r_0^*(X) &= (1 - \Delta_C X); \\ D^*(X) &= (1 + \Delta_B X)(1 - \Delta_C X)^3. \end{aligned} \quad (6)$$

The dependence of the Debye temperature at $T = 0$ K and $P = 0$ (i.e., at $c = r_0$) on the isotope content can be expressed (with allowance for the fact that the chemical bond energy in diamond is two to three orders of magnitude greater than the energy of zero-point oscillations) as follows [12]:

$$\begin{aligned} \Theta_0^*(X) &\cong [D^*/(r_0^*)^2 m^*]^{1/2} \\ &= [(1 + \Delta_B X)(1 - \Delta_C X)/(1 + \Delta_m X)]^{1/2}, \end{aligned} \quad (7)$$

where $m^* = 1 + \Delta_m X$ (for diamond, $\Delta_m = (13/12) - 1 = 0.0833$). For $X > 0$, we must have $\Theta_0^*(X) < 1$ and, hence, $\Delta_B - \Delta_C < \Delta_m$. This implies that $\Delta_B < \Delta_m + \Delta_C \cong 0.084$, and, therefore, the value of $\Delta_B = 17 \times 10^{-2}$ reported in [11] is obviously overstated.

The heat capacity at constant volume under conditions of relatively high and low temperatures can be evaluated as $C_v(T \gg \Theta_0) \cong 3R$ and $C_v(T \ll \Theta_0) \cong (12\pi^4/5)R(T/\Theta_0)^3$, where *R* is the universal gas constant. Using these estimates, the isotope dependence of the molar heat capacity at high and low temperatures can expressed as $C_v^*(X)_{\text{high}} \cong 1$ and $C_v^*(X)_{\text{low}} \cong [\Theta_0^*(X)]^{-3}$, from which we infer that $C_v^*(X)_{\text{low}}$ increases with *X*. On the other hand, the isotope dependence of the heat capacity decreases with increasing temperature.

The isobaric thermal expansion coefficient is defined as $\alpha_p(T) = \gamma C_v(T)/B(T)V(T)$ [13]. For $T \gg \Theta_0$ and $P = 0$, the isotope dependence of this coefficient is described by the relation

$$\alpha_p^*(X)_{\text{high}} \cong 1/D^*(X) = 1/[(1 + \Delta_B X)(1 - \Delta_C X)^3]. \quad (8)$$

For $T \ll \Theta_0$ and $P = 0$, the behavior of $\alpha_p^*(X)$ changes to the opposite:

$$\begin{aligned} \alpha_p^*(X)_{\text{low}} &\cong 1/\{D^*(X)[\Theta_0^*(X)]^3\} \\ &= (1 + \Delta_m X)^{3/2}/[(1 + \Delta_B X)^{5/2}(1 - \Delta_C X)^{9/2}]. \end{aligned} \quad (9)$$

The relations described by formulas (8) and (9) with $\Delta_m = 0.0833$, $\Delta_C = 0.00015$ [8, 10], and $\Delta_B = 0.01$ are presented in the figure. It should be noted that this Δ_B value is more than five times that reported in [11], but even with such an overstated parameter, the value of $\alpha_p^*(X)$ increases in the low-temperature limit and decreases in the high-temperature limit. Therefore,

there is a certain intermediate temperature T_x at which the thermal expansion coefficient of diamond is independent of the isotope composition, that is, $\alpha_p^*(T = T_x) = \text{const}$. At $T < T_x$, the function $\alpha_p^*(X)$ increases, and at $T > T_x$ it decreases with increasing X.

The energy of vacancy formation and the self-diffusion activation energy at $T \gg \Theta_0$ and $P = 0$ depend on the isotope composition in the same manner [14, 15]:

$$E_i^*(X)_{\text{high}} \cong m^*(c^*\Theta_0^*)^2 = (1 + \Delta_B X)(1 - \Delta_C X)^3. \quad (10)$$

Since the activation energy cannot decrease with increasing isotope mass (i.e., $E_i^*(X)_{\text{high}} \geq 1$), it follows that $\Delta_B \geq 3\Delta_C$. In this context, the value of $\Delta_B = -1.8 \times 10^{-2}$ reported in [9] is hardly probable. For diamond, the Δ_B value must fall within the following interval:

$$(3\Delta_C < 0.001) \leq \Delta_B < (\Delta_m + \Delta_C \cong 0.084).$$

According to [16], the specific (per unit surface area) surface energy at $T \gg \Theta_0$ and $P = 0$ depends on the isotope composition as follows:

$$\sigma^*(X)_{\text{high}} \cong D^*/(c^*)^2 = (1 + \Delta_B X)(1 - \Delta_C X). \quad (11)$$

Assuming that the Poisson ratio is independent of X, we obtain the following relation for the isotope dependence of the longitudinal sound velocity at $T = 0$ K and $P = 0$ [4, 17]:

$$\omega_0^*(X) \cong [D^*(X)/m^*(X)]^{1/2} = [(1 + \Delta_B X)(1 - \Delta_C X)^3/(1 + \Delta_m X)]^{1/2}. \quad (12)$$

Gromnitskaya *et al.* studied the crystals of ^{7}Li and ^{6}Li isotopes and obtained reliable experimental data on the isotope dependence of the lattice parameter and the longitudinal sound velocity: $\Delta_c = (4–6) \times 10^{-4}$ and $\omega_0^*(X) = \omega_0^*(^7\text{Li})/\omega_0^*(^6\text{Li}) \cong 5.7[\text{km/s}]/6.1[\text{km/s}] = 0.93443$, where $X = [^7\text{Li}]/([^6\text{Li}] + [^7\text{Li}])$ and $\Delta_m = (7/6) - 1 = 0.1667$ (for lithium, $\gamma_0 = 1$ [18]). Using these data and formula (12), we obtain a relation $\Delta_B = (2–2.05) \times 10^{-2}$, which implies that the bulk compression modulus increases upon the passage from ^{6}Li to ^{7}Li. This conclusion contradicts the results obtained in [18] using a different method, according to which $\Delta_B < 0$. This discrepancy is related to the fact that the method used in [18] did not take into account the effect of isotope composition on the parameters of interatomic interaction in crystalline lithium.

An analysis of the established relations leads to the following conclusions:

(i) The function $c_0^*(X)$ decreases, while the functions $B_0^*(X)$ and $(1 + \Delta_B X)(1 - \Delta_C X)$ increase with increasing atomic fraction X of the heavy isotope. For this reason, the increase in X is accompanied by increase of the $D^*(X)$, $C_v^*(X)_{\text{low}}$, $\alpha_p^*(X)_{\text{low}}$, $E_i^*(X)_{\text{high}}$, and $\sigma^*(X)_{\text{high}}$ functions and by decrease of the $r_0^*(X)$, $\Theta_0^*(X)$, $\alpha_p^*(X)_{\text{high}}$, and $\omega_0^*(X)$ functions.

(ii) As the temperature is increased, the heat capacity at constant volume ceases to depend on the isotope composition (i.e., $C_v^*(X)_{\text{high}} \cong 1$), while the isotope dependence of the thermal expansion coefficient exhibits a change in the trend: the increase in $\alpha_p^*(X)_{\text{low}}$ changes to a gradual decrease in $\alpha_p^*(X)_{\text{high}}$.

(iii) The depth D of the interatomic potential well slightly increases with X (see (6)). Taking into account that the temperatures of the first-order phase transitions are linear functions of the D value [19], we may expect that the melting point and the temperatures of other first-order phase transitions must increase with X.

(iv) The latent heat of the crystal–liquid phase transition, the enthalpy of sublimation, and the latent heats of polymorphous first-order phase transitions are usually proportional to the depth D of the interatomic potential well [19]. For this reason, we may expect that the latent heats of such transitions grow with increasing X.

(v) The temperature, molar volume, and pressure at a critical point of the liquid–vapor phase transition are usually proportional to the parameters of the interatomic interaction potential [19]: $T_{\text{cr}} \sim D/k_{\text{b}}$; $V_{\text{cr}} \sim r_0^3$; $P_{\text{cr}} \sim D/r_0^3 \sim (1 + \Delta_B X)$ (k_{b} is Boltzmann's constant). Therefore, it is expected that T_{cr}, and P_{cr} will grow, while V_{cr} will decrease with increasing X. In accordance with the law of corresponding states for nonpolar substances [20], the compressibility factor at the critical point is independent of the isotope composition: $Z_{\text{cr}} = P_{\text{cr}}V_{\text{cr}}/RT_{\text{cr}} = \text{const} = 0.27$. This result additionally confirms the correctness of the proposed method of calculation of the properties of crystals as functions of the isotope composition.

(vi) Since $D^*(^{13}\text{C}) > D^*(^{12}\text{C})$ and $D^*(^7\text{Li}) > D^*(^6\text{Li})$, and, in the general case, $D^*(^{k+1}A) > D^*(^kA)$, condensation from a gas phase comprising a mixture of isotopes must lead with a higher probability to the formation of clusters enriched with heavier isotopes. This was in fact observed in the study of isotope composition of condensed Ne clusters containing 4–22 atoms [21], where the content of the ^{22}Ne isotope (~12.5%) was significantly greater than that (~8.7%) in the initial gas phase with a natural isotope composition.

(vii) Since $\sigma^*(^{13}\text{C})_{\text{high}} > \sigma^*(^{12}\text{C})_{\text{high}}$ and $\sigma^*(^7\text{Li})_{\text{high}} > \sigma^*(^6\text{Li})_{\text{high}}$, and, in the general case $\sigma^*(^{k+1}A)_{\text{high}} > \sigma^*(^kA)_{\text{high}}$, the criterion formulated in [22] implies that

crystallization must be accompanied by the predominant formation of nanocrystals involving heavy isotopes. Therefore, nanocrystals formed in a mixture of various isotopes will be enriched by the heavy isotopes as compared to macroscopic crystals.

Acknowledgments. The author is grateful to A.D. Filenko, K.N. Magomedov, and Z.M. Surkhaeva for fruitful discussions and their help with the work.

This study was supported by the Russian Foundation for Basic Research (project no. 02-03-33301) and the Russian Academy of Sciences (project no. 7/067-095/05.05.04-229).

REFERENCES

1. E. A. Moelwyn-Hughes, *Physical Chemistry* (Pergamon Press, London, 1961).
2. M. N. Magomedov, Zh. Fiz. Khim. **62**, 2103 (1988).
3. M. N. Magomedov, Zh. Fiz. Khim. **63**, 1106 (1989).
4. M. N. Magomedov, Zh. Fiz. Khim. **63**, 2943 (1989).
5. M. N. Magomedov, Zh. Neorg. Khim. **49**, 2057 (2004).
6. I. V. Aleksandrov, A. F. Goncharov, A. N. Zisman, and S. M. Stishov, Zh. Éksp. Teor. Fiz. **93**, 680 (1987) [Sov. Phys. JETP **66**, 384 (1987)].
7. S. M. Stishov, Pis'ma Zh. Éksp. Teor. Fiz. **71**, 25 (2000) [JETP Lett. **71**, 15 (2000)].
8. H. Hollowey, K. S. Hass, M. A. Tamor, *et al.*, Phys. Rev. B **44**, 7123 (1991).
9. Ph. Gillet, G. Fiquet, I. Daniel, *et al.*, Phys. Rev. B **60**, 14660 (1999).
10. V. G. Plekhanov, Usp. Fiz. Nauk **173**, 711 (2003) [Phys. Usp. **46**, 689 (2003)].
11. D. C. Hurley, R. S. Gilmore, and W. F. Banholzer, J. Appl. Phys. **76**, 7726 (1994).
12. M. N. Magomedov, Fiz. Tverd. Tela (St. Petersburg) **45**, 33 (2003) [Phys. Solid State **45**, 32 (2003)].
13. S. I. Novikova, *Thermal Expansion of Solids: A Handbook* (Nauka, Moscow, 1974) [in Russian].
14. M. N. Magomedov, Pis'ma Zh. Tekh. Fiz. **27** (18), 36 (2001) [Tech. Phys. Lett. **27**, 773 (2001)].
15. M. N. Magomedov, Pis'ma Zh. Tekh. Fiz. **28** (10), 64 (2002) [Tech. Phys. Lett. **28**, 430 (2002)].
16. M. N. Magomedov, Fiz. Tverd. Tela (St. Petersburg) **46**, 924 (2004) [Phys. Solid State **46**, 954 (2004)].
17. M. N. Magomedov, Zh. Fiz. Khim. **58**, 1804 (1984).
18. E. L. Gromnitskaya, O. V. Stal'gorova, and S. M. Stishov, Pis'ma Zh. Éksp. Teor. Fiz. **69**, 36 (1999) [JETP Lett. **69**, 38 (1999)].
19. B. M. Smirnov, Usp. Fiz. Nauk **171**, 1291 (2001) [Phys. Usp. **44**, 1229 (2001)].
20. R. C. Reid, J. M. Prausnitz, and T. K. Sherwood, *The Properties of Gases and Liquids* (McGraw-Hill, New York, 1977; Khimiya, Leningrad, 1982).
21. P. Scheier and T. D. Mark, J. Chem. Phys. **87**, 5238 (1987).
22. V. I. Nizhenko, Powder Metall. Met. Ceram. **43**, 273 (2004).

Translated by P. Pozdeev

Technical Physics Letters, Vol. 31, No. 5, 2005, pp. 385–387. Translated from Pis'ma v Zhurnal Tekhnicheskoĭ Fiziki, Vol. 31, No. 9, 2005, pp. 58–62.

Exact Analytical Solutions of Self-Consistent Equations of Plasma Hydrodynamics with Absorbing Boundary Conditions

V. A. Fedorov

Mints Radio Engineering Institute, Moscow, Russia

Received December 9, 2004

Abstract—Exact analytical solutions of a one-dimensional self-consistent system of nonlinear hydrodynamic equations are obtained for plasma with absorbing boundary conditions on the conducting surface of an insulated body. The electric field strength, electron velocity, and electron density in the plasma are determined. © *2005 Pleiades Publishing, Inc.*

Solution of the boundary-value problems of dynamics for the flows of charged particles, which move toward the surface of an absorbing body and are not compensated by the space charge, makes it necessary to determine a self-consistent electric field dependent on the distribution of charged particles and on their total number varying with time. The difficulty of simultaneous description of these factors is the main obstacle to obtaining analytical solutions, which inspires formulation of simplified problems [1, 2] or use of the boundary conditions without absorption [3, 4].

In order to surmount this obstacle, let us write, in an analytical form, the law of conservation of electric charge in the system comprising a charged insulated body and a layer of plasma. Thereby, we obtain an additional integral of motion for the system of equations, which will allow us to determine simultaneously the distribution of charged particles and their variable total number. This approach makes it possible to obtain exact analytical solutions for a nonlinear system of equations of plasma hydrodynamics with absorbing boundary conditions, which was the aim of the present study.

We consider a plasma layer of thickness Δ in contact with an electrically insulated body bounded by conducting surface S_0 bearing charge $Q_0(0) > 0$ with a surface density of $\sigma_0(0)$. Let the total initial charges of electrons ($Q_e(0)$) and ions ($Q_i(0)$) in the plasma layer satisfy the condition $Q(0) + Q_e(0) + Q_i(0) = 0$. Assuming that only electrons are mobile and that the motion is one-dimensional, we can rewrite this relation as

$$\sigma_0(t)R_0^\kappa + \int_{R_0}^{R_c} e[n_e(R, t) - n_i(R, 0)]R^\kappa dR = 0, \quad (1)$$

where R_0 and R_c are the distances from the plasma boundaries to the origin; $R_c = R_0 + \Delta$; $\kappa = 0$, 1, and 2 for the plane, cylindrical, and spherical symmetries, respectively; $n_{e,i}(R, t)$ are the electron and ion densities in the plasma; e is the electron charge; and R is the distance (radius) from the origin to a point in space.

The system of one-dimensional hydrodynamic equations for electrons in a cold plasma can be written as [5]

$$\frac{\partial v_e}{\partial t} + v_e\frac{\partial v_e}{\partial R} + \nu_e v_e = \frac{e}{m_e}E, \quad (2)$$

$$\frac{1}{R^\kappa}\frac{\partial}{\partial R}(R^\kappa E) = 4\pi e(n_e - n_i), \quad (3)$$

$$\frac{\partial E}{\partial t} = -4\pi e n_e v_e, \quad (4)$$

where $E(R, t) = E_0(R, t) + E_e(R, t) + E_i(R, 0)$ is the strength of the electric field generated by charges $Q_0(t)$, $Q_e(t)$, and $Q_i(0)$; $v_e(R, t)$ and m_e are the electron velocity and mass, respectively; and ν_e = const is the frequency of collisions between electrons and neutral particles in the plasma.

The initial and boundary conditions for the system of equations (2)–(4) are as follows [6]:

$$v_{e,i}(R_*, 0) = 0, \quad n_{e,i}(R_*, 0) = n_{e,i}^0 f_{e,i}(R_*, 0), \quad (5)$$

$$E(R_*, 0) = \frac{4\pi}{R_*^\kappa}\left\{\sigma_0(t)R_0^\kappa + \int_{R_0}^{R_*} e[n_e^0 f_e(R_*, 0) - n_i^0 f_i(R_*, 0)]R_*^\kappa dR_*\right\}, \quad (6)$$

$$v_{e,i}(R_0, t) = 0, \quad n_{e,i}(R_0, t) = 0, \quad (7)$$

$$-\frac{\partial\sigma_0(t)}{\partial t} = en_e(R_0 + 0, t)v_e(R_0 + 0, t), \quad E(R_0, t) = 4\pi\sigma_0(t), \quad (8)$$

1063-7850/05/3105-0385$26.00

$$E(R_c, t) = 0, \quad v_{e,i}(R_c, t) = 0,$$
$$n_{e,i}(R_c, t) = n^0_{e,i} f_{e,i}(R_c, t), \tag{9}$$

where $R_0 \le R_* \le R_c$; $n^0_e = n^0_i$ = cost are the unperturbed electron and ion densities, respectively; and $f_{e,i}(R, t) \ge 1$.

Integrating Eq. (3) over the plasma volume and using the Gauss theorem, we obtain

$$E(R_*, t) = \frac{4\pi}{R^\kappa}\left\{\sigma_0(t)R_0^\kappa + \int_{R_0}^{R} en^0_e[f_e(R_*, t) - f_i(R_*, 0)]R^\kappa dR\right\}, \tag{10}$$

where R is the final position of the mobile boundary, which initially ($t = 0$) occurred at the point R_*. Condition (1) can be rewritten as

$$\sigma_0(t)R_0^\kappa + \int_{R_0}^{R} en^0_e[f_e(R, t) - f_i(R, t)]R^\kappa dR = -\int_{R}^{R_c} en^0_e[f_e(R, t) - f_i(R, 0)]R^\kappa dR. \tag{11}$$

Using relations (10) and (11), we obtain

$$E(R, t) = -\frac{m_e}{e}\left\{\omega_0^2\int_{R}^{R_c}[f_e(R, t) - f_i(R, 0)]R^\kappa dR\right\}\frac{1}{R^\kappa}, \tag{12}$$

where $\omega_0^2 = 4\pi e^2 n^0_e/m_e$. Assuming that the electron trajectories do not intersect, we have [7]

$$\int_{R}^{R_c} n_e(R, t)R^\kappa dR = \int_{R_*}^{R_c} n_e(R_*, 0)R_*^\kappa dR_*. \tag{13}$$

Using this relation, Eq. (12) can be rewritten as

$$E(R_*, E) = -\frac{m_e}{e}\left[C(R_*) - \omega_0^2\int_{R}^{R_c} f_i(R, 0)R^\kappa dR\right]\frac{1}{R^\kappa}, \tag{14}$$

where $C(R_*) = \omega_0^2\int_{R_*}^{R_c} f_e(R_*, 0)R_*^\kappa dR_*$. Substituting this expression into Eq. (2), we obtain

$$\frac{\partial v_e}{\partial t} + v_e\frac{\partial v_e}{\partial R} + \nu_e v_e = -\left[C(R_*) - \omega_0^2\int_{R}^{R_c} f_i(R, 0)R^\kappa dR\right]\frac{1}{R^\kappa}. \tag{15}$$

Passing to a substantial derivative in relation (15), we obtain

$$\frac{d^2R}{dt^2} + \nu_e\frac{dR}{dt} = -\left[C(R_*) - \omega_0^2\int_{R}^{R_c} f_i(R, 0)R^\kappa dR\right]\frac{1}{R^\kappa}. \tag{16}$$

Rewriting Eq. (5) in the Lagrange coordinates, we arrive at an equation for determining $n_e(R_*, t)$:

$$n_e(R_*, t) = n_i(R_*, 0) + \frac{1}{4\pi e}\left(\kappa\frac{E}{R} + \frac{\partial E}{\partial R} + \frac{\partial E}{\partial R_*}\frac{1}{\partial R/\partial R_*}\right). \tag{17}$$

Equation (15) can be reduced to the Abel equation of the second kind [8],

$$v_e\frac{\partial v_e}{\partial R} + \nu_e v_e = -\left[C(R_*) - \omega_0^2\int_{R}^{R_c} f_i(R, 0)R^\kappa dR\right]\frac{1}{R^\kappa}. \tag{18}$$

For $\nu_e = 0$, let us seek a solution to Eq. (2) in the following form:

$$v_e(R_*, R) = -\left[C(R_*) - \omega_0^2\int_{R}^{R_c} f_i(R, 0)R^\kappa dR\right]\frac{1}{R^\kappa}. \tag{19}$$

This yields

$$t(R_*, R) = \pm\int_{R_*}^{R}\frac{dR}{\sqrt{-\left[C(R_*) - \omega_0^2\int_{R}^{R_c} f_i(R, 0)R^\kappa dR\right]\frac{1}{R^\kappa}}}. \tag{20}$$

Rewriting Eq. (3) in the Lagrange coordinates and using relations (14) and (20), we obtain the relation

$$n_e(R_*, R) = n_i^0 + \frac{1}{4\pi e}\left(\kappa\frac{E}{R} + \frac{\partial E}{\partial R} + \frac{\partial E}{\partial R_*}\frac{\partial t/\partial R}{\partial t/\partial R_*}\right). \tag{21}$$

Expressions (14)–(17) and (19)–(21) offer analytical solutions to the self-consistent nonlinear hydrodynamic equations for a plasma with absorbing nonstationary boundary conditions in the cases of various symmetry. For the system under consideration, these solutions were obtained owing to the fact that the law of electric charge conservation was written in an explicit form that provided an additional integral of motion for the system of equations and allowed the distribution of charged particles and their variable number to be simultaneously determined.

It should be noted that such an increase in the number of integrals of motion for dynamic structures significantly expands the class of problems admitting exact analytical solutions for nonlinear systems of equations. In particular, this method is of interest for investigations into the dynamics of charged particles in double plasma layers [9] frequently encountered in free space and in the vicinity of insulated charged absorbing bodies both under laboratory conditions [10] and in space [11, 12].

REFERENCES

1. A. A. Rukhadze, L. S. Bogdankevich, S. E. Rosinskiĭ, *et al.*, *Physics of High-Current Relativistic Electron Beams* (Atomizdat, Moscow, 1980) [in Russian].
2. E. E. Barminova and A. S. Chikhachev, Radiotekh. Élektron. (Moscow) **37**, 2097 (1992).
3. N. D. Naumov, Radiotekh. Élektron. (Moscow) **45**, 755 (2000).
4. V. A. Fedorov, Radiotekh. Élektron. (Moscow) **47**, 103 (2002).
5. V. L. Ginzburg and A. A. Rukhadze, *Waves in Magnetoactive Plasma* (Nauka, Moscow, 1975); *Hand Physics* (Springer Verlag, 1972), Vol. 49.
6. L. I. Sedov, *A Treatise on Continuum Mechanics* (Nauka, Moscow, 1983), Vol. 1 [in Russian].
7. K. P. Stanyukovich, *Nonstationary Motions of Continuum Media* (Nauka, Moscow, 1971) [in Russian].
8. E. von Kamke, *Differentialgleichungen. Losungsmethoden und Losungen* (Akademie Verlag, Leipzig, 1951; Nauka, Moscow, 1976).
9. I. Langmuir, Phys. Rev. **33**, 954 (1929).
10. S. Eliezer and H. Hora, Phys. Rep. **172**, 339 (1989).
11. L. P. Block, in *Physics of Hot Plasma in the Magnetosphere*, Ed. by B. Hultquist and L. Stenflo (Plenum, New York, 1975), pp. 229–250.
12. *Artificial Particle Beams in Space Plasma Studies*, Ed. by B. Grandal (Plenum, New York, 1982).

Translated by P. Pozdeev

Technical Physics Letters, Vol. 31, No. 5, 2005, pp. 388–390. Translated from Pis'ma v Zhurnal Tekhnicheskoĭ Fiziki, Vol. 31, No. 9, 2005, pp. 63–68.

Relativistic Magnetron with Distributed Output of Microwave Radiation

I. I. Vintizenko*, A. I. Zarevich, and S. S. Novikov

Nuclear Physics Institute, Tomsk Polytechnic University, Tomsk, Russia

** e-mail: lablia@npi.tpu.ru*

Received October 18, 2004

Abstract—Problems related to the extraction and shaping of microwave radiation generated by a relativistic magnetron have been experimentally studied. A modified magnetron oscillator is described, in which a coupling waveguide channel loaded on a system of radiators is provided between elements of the resonance system. It is shown that this scheme allows the required amplitude–phase profiles of oscillations to be obtained and ensures high spectral and amplitude stability of the output radiation. © *2005 Pleiades Publishing, Inc.*

The development of relativistic microwave radiation sources encounters problems related to the transfer and shaping of electromagnetic oscillations on an ultrahigh power level. These problems are caused by the low electric strength of the elements involved in the output power extraction and by the large dimensions and weights of such oscillators. These factors restrict the possibility of using classical methods for the extraction and shaping of the output microwave radiation and stimulate the search for new original solutions. In a relativistic magnetron, one possible solution consists in increasing the number of output waveguides. However, this reduces the Q value of the entire system and leads (in view of instability of the pulsed voltage and nonstationary operation of the explosive emission cathodes) to a decrease in the coherency of oscillations.

Previously, we developed a modified magnetron oscillator in which a mutual coupling waveguide channel loaded on a common radiator was provided between the cavities [1]. The results of experiments showed the high efficiency of this method for the stabilization of oscillations [2]. Further development of this idea is offered by a magnetron with distributed microwave radiation output [3, 4].

This paper presents the results of our experimental investigation of such a modified relativistic magnetron oscillator with distributed microwave radiation output aimed at elucidating the influence of the external mutual coupling between cavities in the anode unit on the output radiation characteristics.

The experimental setup (Fig. 1) comprised a periodic-pulse six-cavity *S*-band relativistic magnetron *1* with magnetic system *2*, a pumping source including section *3* of an induction linear accelerator (LIU 0.4/6), and a stabilized power supply for the magnet. Two opposite cavities of the anode unit are linked via external coupling waveguide structure *4* to three radiators *5*. This setup [5] generates microwave pulses with a repetition frequency of up to 320 Hz at a cathode–anode voltage of ~450 V and a total current of ~3 kA. The coupling channel is composed of rectangular 72 × 34-mm waveguide sections and loaded on waveguide H-tees connected to radiating horn antennas *6*. In these experiments, we determined the power and measured the spectrum of pulsed microwave radiation as described in [6].

The introduction of mutual coupling between cavities of the magnetron leads to the interaction of microwave fields in these cavities, which results in mutual leveling of the amplitudes and phases of microwave oscillations in the anode unit. This favors stabilization of the working mode, for which oscillations traveling over the coupling waveguide structure are in phase with oscillations in the cavities, and provides suppression of the other modes.

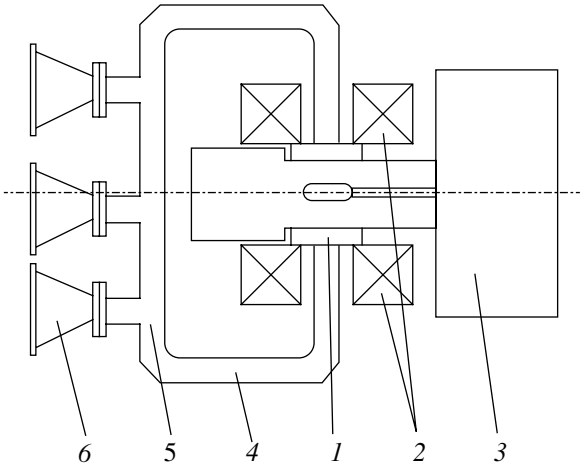

Fig. 1. Schematic diagram of the experimental setup (see text for explanations).

1063-7850/05/3105-0388$26.00 © 2005 Pleiades Publishing, Inc.

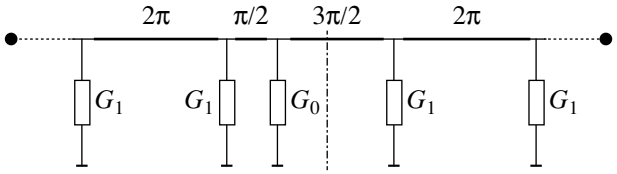

Fig. 2. Equivalent circuit diagram of the coupling channel.

The coupling channel was constructed according to a symmetric-asymmetric scheme [7]. Figure 2 shows an equivalent circuit diagram of the coupling channel for an arbitrary number of loads [8]. The central load G_0 is shifted by π/2 relative to the electrical symmetry axis of the channel. For the working π mode, the oscillations of opposite cavities are in phase at the chain inputs and, hence, are subtracted in the G_0 load. If the neighboring loads G_1 are shifted by π/2 relative to the central load and the other loads are shifted by a multiple of π relative to each other, the system will feature a "parallel" connection of loads in the left and right groups. In order to provide for a distribution of oscillations with equal amplitudes between the loads, it is necessary to ensure their equal conductivities. The distribution is phase matched if the distances between loads in the groups are multiples of 2π and if one of the groups is additionally shifted by π relative to the central load. The central load plays an important role in the mode selection. Calculations of the resonance system of the modified magnetron showed that losses introduced by this load in the counterphase regimes significantly reduce the loaded Q value, thus providing for rapid damping of all oscillations other than the working mode.

In our experiments, the length of the coupling channel was selected based on the results of preliminary investigations [2, 9] and amounted to ~34π for the working π mode. The right and left loads were spaced by 5π/2 and 7π/2 from the central one. In the uncoupled regime, the magnetron had the following characteristics. The level of radiation power at each output was ~190 MW at a total energy of ~4.8 J per pulse. The radiation frequency was ~2740 MHz. The current spectrum in a ~200 MHz bandwidth (Fig. 3a) exhibits several clear maxima, which probably correspond to coexisting (competing) modes. Figure 3b shows matched oscillograms of ten microwave pulses. The observed scatter in the pulse shape reflects instability of the oscillation process.

When the magnetron outputs are combined via the coupling channel, the levels of power and pulse energy at the central radiator output do not exceed 25 MW and 1.5 J, respectively. This result shows that oscillations are subtracted in the central load and confirms the existence of the working π mode. The results of spectral measurements for one of the side radiators are presented in Fig. 3c. The magnetron frequency in this experiment was 2720 MHz, and the current spectrum width at the pulse center did not exceed 30 MHz (at a −3 dB level). The levels of power in the side radiators were close (the difference did not exceed 10%) and amounted to ~200 MW at a pulse energy of ~5 J, which was indicative of the equal amplitudes of oscillations in the loads. The output radiation was characterized by a high amplitude and temporal stability, as evidenced by the matched oscillograms of ten pulses in Fig. 3d.

Stability of the oscillation phase distribution over the system of coupled horn radiators was confirmed by special measurements of the spatial distribution of microwave radiation. The presence of deep minima (−13 dB) in the directional diagram was evidence of the

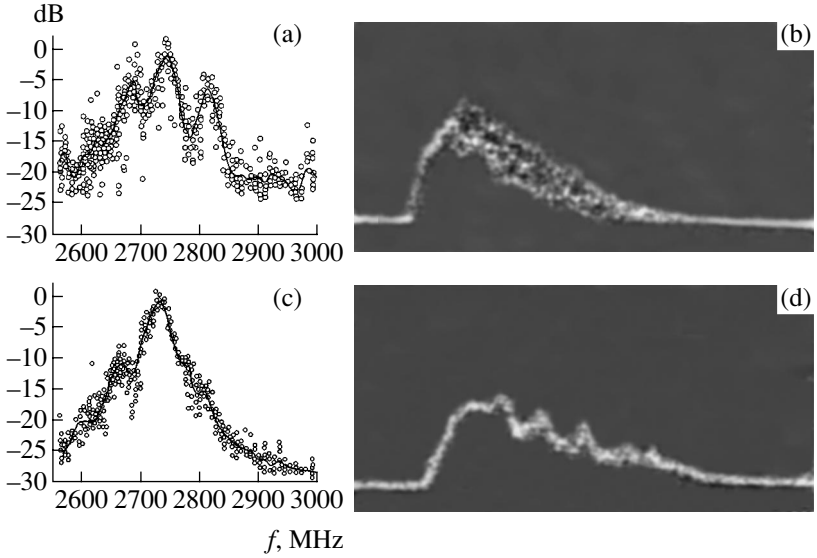

Fig. 3. (a, c) Microwave radiation spectra and (b, d) oscillograms of the microwave radiation pulses measured in the relativistic magnetron (a, b) without and (c, d) with an external coupling channel.

stability of the amplitude–phase profile in the working regime.

Thus, the results of our investigation showed that the coupling of cavities in the modified relativistic magnetron via the external coupling channel loaded on the common radiators makes realization of a distributed power output with a required amplitude–phase profile possible. The interaction of oscillations generated in the system of cavities ensures a high mode, amplitude, and spectral stability of the pulsed output microwave radiation. The obtained results can be used in the development of ultrahigh-power radiating systems based on relativistic microwave oscillators.

REFERENCES

1. I. I. Vintizenko, A. I. Zarevich, and S. S. Novikov, RF Patent No. 2190281; Byull. Izobret., No. 27 (2001).
2. I. I. Vintizenko, V. I. Gusel'nikov, A. I. Zarevich, and S. S. Novikov, Pis'ma Zh. Tekh. Fiz. **29** (7), 64 (2003) [Tech. Phys. Lett. **29**, 294 (2003)].
3. I. I. Vintizenko, A. I. Zarevich, and S. S. Novikov, RF Patent No. 2228560; Byull. Izobret., No. 13 (2004).
4. A. I. Zarevich, I. I. Vintizenko, and S. S. Novikov, in *Proceedings of the 13th International Symposium on High Current Electronics, Tomsk, 2004*, pp. 269–272.
5. L. D. Butakov, I. I. Vintizenko, V. I. Gusel'nikov, *et al.*, Pis'ma Zh. Tekh. Fiz. **26** (13), 66 (2000) [Tech. Phys. Lett. **26**, 571 (2000)].
6. A. I. Zarevich, E. V. Vegner, and I. I. Vintizenko, Prib. Tekh. Éksp., No. 3, 78 (2004).
7. S. A. Maĭdanovskiĭ and S. S. Novikov, Radiotekh. Élektron. (Moscow) **48** (6), 1 (2003).
8. S. S. Novikov and A. I. Zarevich, in *Proceedings of the 1st International Congress on Radiation Physics, High Current Electronics and Modification of Materials, Tomsk, 2000*, Vol. 2, pp. 466–469.
9. A. I. Zarevich, I. I. Vintizenko, and S. S. Novikov, in *Proceedings of the 13th International Symposium on High Current Electronics, Tomsk, 2004*, pp. 300–303.

Translated by P. Pozdeev

Technical Physics Letters, Vol. 31, No. 5, 2005, pp. 391–393. Translated from Pis'ma v Zhurnal Tekhnicheskoĭ Fiziki, Vol. 31, No. 9, 2005, pp. 69–75.

Observation of the Radiative Transitions between $4d^9(^2D_{5/2,3/2})5s^2nl$ and $4d^{10}5p(^2P^0_{1/2,3/2})nl$ Autoionization States of Cadmium Atom Excited by Electron–Ion Collisions

A. N. Gomonai* and A. I. Imre

Institute of Electron Physics, National Academy of Sciences of Ukraine, Uzhgorod, Ukraine

** e-mail: ovetex@mail.uzhgorod.ua; dep@mail.uzhgorod.ua*

Received August 3, 2004

Abstract—Radiative transitions between the $4d^9(^2D_{5/2,3/2})5s^2nl$ and $4d^{10}5p(^2P^0_{1/2,3/2})nl$ autoionization states of the cadmium atom, representing dielectronic recombination satellites of the laser lines of Cd^+ ion with λ = 325.0 nm ($4d^95s^2\ ^2D_{3/2} \longrightarrow 4d^{10}5p^2P^0_{1/2}$) and λ = 353.6 nm ($4d^95s^2\ ^2D_{3/2} \longrightarrow 4d^{10}5p^2P^0_{3/2}$), have been observed for the first time in the regime of electron–ion collisions. The energy dependence of the effective cross sections for the electron-impact excitation of satellite lines has been studied in the interval from 7 to 10 eV. The effective cross sections for the excitation of dielectronic recombination satellites are on the order of ~10^{-17} cm^2, which is comparable with the efficiency of excitation of the main laser lines. © *2005 Pleiades Publishing, Inc.*

Reliable spectroscopic diagnostics and simulation of astrophysical and laboratory plasmas can be based upon the knowledge of the qualitative behavior and quantitative characteristics of the main atomic processes, including electron–ion collisions. An important role in the balance of impact ionization of positive ions taking place during such collisions in low-density plasma is played by the dielectronic recombination (DR) of ions [1]. This process involves trapping of a free electron by the ion with the formation of an intermediate autoionization state. This intermediate state decays via a radiative channel to a stable state of the atom (or the ion with a charge reduced by unity, which can take place for multiply charged ions). Radiative decay of the autoionization states may decrease the contribution of resonances to the excitation cross section by half for moderately charged ions and even more significantly for multiply charged ions [2].

Under the conditions of crossed electron and ion beams, DR was originally observed for K^+ [3] and, later, for Cs^+, Rb^+ [4], and Tl^+ [5] ions. The photon–ion coincidence technique was successfully used for the investigation of DR in Mg^+ [6] and Ca^+ [7] ions. However, the radiation observed in these experiments was due to transitions in which only the upper level corresponded to an autoionization state, whereas the lower level represented a usual level of the neutral atom (or the ion with a charge reduced by unity). The limits of convergence for these autoionization states were the lower resonance levels of the ion. For the autoionization states converging to higher levels of the ion, there is an additional channel of radiative decay to the other autoionization states with lower energy levels. Such radiative transitions between the autoionization states of the lithium atom were experimentally observed and studied using electron–atom collisions [8], and it was pointed out that the intensity of spectral lines corresponding to these transitions is quite high. However, no data are available for the transitions between autoionization states formed upon electron–ion collisions. Therefore, direct observation of the radiative transitions between autoionization states formed in collisions of low-energy electrons with ions is of considerable basic importance.

This paper presents the results of a spectroscopic investigation of the radiative transitions between the $4d^9(^2D_{5/2,3/2})5s^2nl$ and $4d^{10}5p(^2P^0_{1/2,3/2})nl$ autoionization states of the Cd atom observed for the first time upon collisions between low-energy electrons and Cd^+ ions. This study was also of interest from the standpoint of applications, since the observed lines are satellites of the $4d^95s^2\ ^2D_{3/2} \longrightarrow 4d^{10}5p^2P^0_{1/2,3/2}$) laser lines of the Cd^+ ion, which are characterized by a low excitation threshold [9].

The spectroscopic experiments were performed on a setup described in detail elsewhere [10]. A low-voltage discharge source generated a stable beam of ions with an energy of 640 eV and a beam current of (6–8) × 10^{-7} A. The discharge voltage ($U_d \le 12$ V) was selected

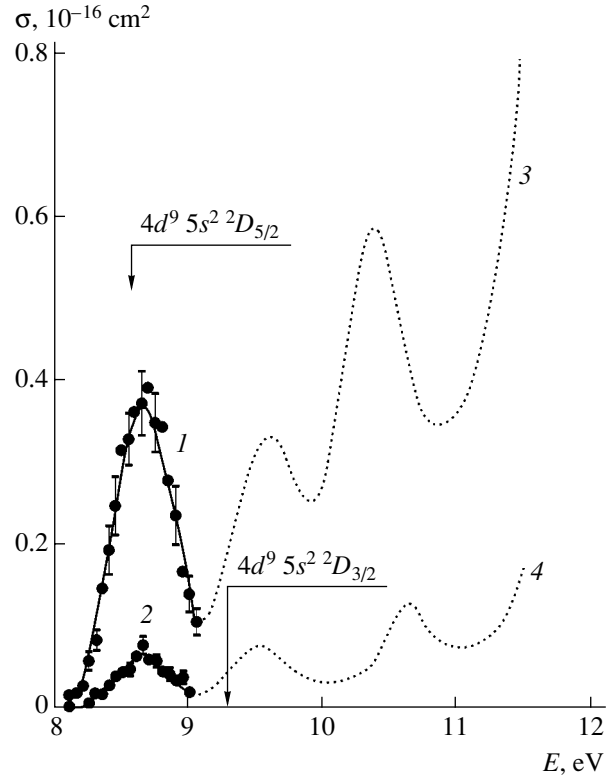

Fig. 1. The energy dependence of the effective cross sections for the electron-impact excitation of DR satellites $4d^9(^2D_{5/2,3/2})5s^2nl \longrightarrow 4d^{10}5p(^2P^0_{1/2,3/2})nl$ measured within (*1*) $\lambda = 325.0 \pm 2$ nm and (*2*) $\lambda = 353.6 \pm 2$ nm in the region of the laser lines of Cd^+ ion with (*3*) $\lambda = 325.0$ nm ($4d^95s^2\ ^2D_{3/2} \longrightarrow 4d^{10}5p\ ^2P^0_{1/2}$) and (*4*) $\lambda = 353.6$ nm ($4d^95s^2\ ^2D_{3/2} \longrightarrow 4d^{10}5p\ ^2P^0_{3/2}$), respectively.

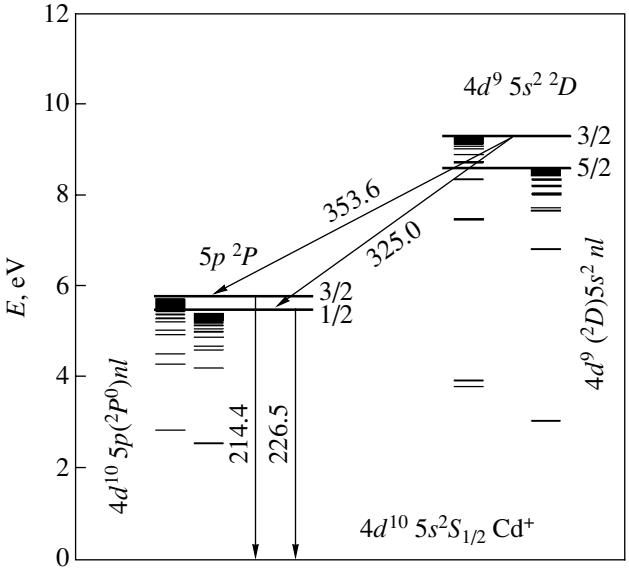

Fig. 2. Schematic diagram of the lower energy levels of Cd^+ ion and the converging autoionization states of Cd atom.

to be definitely below the excitation energy (17.6 eV) for the lowest of the long-lived $4d^95s^2\ ^2D_{5/2,3/2}$ states of Cd^+. This condition provided for a significant decrease in the background related to the radiative decay of these states. A triple-anode electron gun generated a ribbon electron beam with an energy of 7–10 eV, a total current of 7×10^{-5} A and a full width at half maximum (FWHM) of the electron energy distribution $\Delta E_{1/2} = 0.35$ eV. The electron and ion beam crossed in the interaction region at right angles in a vacuum of ~10^{-8} Torr. The radiation was analyzed by a high-aperture grating (1200 lines/mm) monochromator MDR-2 (Russia) with an inverse linear dispersion of ~2 nm/mm. The spectral lines were detected by a water-cooled photoelectron multiplier (FEU-140 Photon). The signal (0.5–1 cps) was accumulated over 1000–1500 s and discriminated against the background by means of a double-beam lock-in scheme gated by voltage pulses shifted by 1/4 of the modulation period, at a signal to noise ratio from 1/20 to 1/30. The process of data acquisition and processing was automated and controlled by a personal computer.

High-precision investigation of the near-threshold regions in the energy dependence of the effective cross sections for electron-impact excitation of the laser lines of Cd^+ ion with $\lambda = 325.0$ nm ($4d^95s^2\ ^2D_{3/2} \longrightarrow 4d^{10}5p\ ^2P^0_{1/2}$) and $\lambda = 353.6$ nm ($4d^95s^2\ ^2D_{3/2} \longrightarrow 4d^{10}5p\ ^2P^0_{3/2}$) showed the presence of intensive radiation at electron energies below the excitation threshold (9.29 eV). It was suggested that this radiation corresponds to satellites of the laser lines. In order to provide for a clear separation of the main lines from satellites and ensure the maximum transmission of the satellite radiation, the measurements were performed in the wavelength intervals $\lambda = 325.0 \pm 2$ nm and $\lambda = 353.6 \pm 2$ nm.

Figure 1 shows the energy dependence of the effective excitation cross sections σ for the Cd^+ lines with $\lambda = 325.0$ and 353.6 nm in the range of electron energies from 7 to 10 eV. Vertical bars at the points show the rms error limits. The absolute values of the effective cross sections were determined with an error not exceeding 15% using a method described in [10]. Figure 2 presents a diagram of the lower energy levels of Cd^+ ion and the converging autoionization states of Cd atom (data on the energies and electron configurations were taken from [11–13]).

As can be seen from Fig. 1, the energy dependences of σ in the region below the excitation threshold of the laser lines studied have the shape of a peak within a narrow energy interval (from 8 to 9 eV) with a maximum at ~8.6 eV. An analysis of the obtained results and published data on the autoionization states of Cd atom showed that these lines are probably related to the radiative decay of $4d^9(^2D_{5/2,3/2})5s^2nl$ autoionization states (formed as a result of resonance trapping of the imping-

ing electron and simultaneous excitation of one *d* electron) to $4d^{10}5p(^2P^0_{1/2,3/2})nl$ autoionization states:

$$e + \mathrm{Cd}^+(4d^{10}5s)^2\mathrm{S}_{1/2} \longrightarrow \mathrm{Cd}^{**}[4d^9(^2D_{5/2,3/2})5s^2nl] \longrightarrow \mathrm{Cd}^{**}[4d^{10}5p(^2P_{1/2,3/2})nl] + h\nu_n. \quad (1)$$

Therefore, the satellite lines are excited by means of the DR mechanism. According to the selection rules, the allowed radiative transitions are $4d^95s^2np \longrightarrow 4d^{10}5pnp$, $4d^95s^2ns \longrightarrow 4d^{10}5pns$, and $4d^95s^2nd \longrightarrow 4d^{10}5pnd$. The most probable transitions in the first series are those between the autoionization states with n = 7–9, which are situated in the interval between the $4d^95s^2\ ^2D_{5/2}$ and $4d^95s^2\ ^2D_{3/2}$ levels (Fig. 2). It should be noted that the lines corresponding to these transitions can represent the DR satellites of only the line with λ = 353.6 nm. Radiative transitions of the $4d^95s^2ns \longrightarrow 4d^{10}5pns$ series proceed primarily between the autoionization states with n = 7–8, while the $4d^95s^2nd \longrightarrow 4d^{10}5pnd$ transitions proceed between the autoionization states with n = 6 situated below the $4d^95s^2\ ^2D_{5/2}$ level. In the latter case, radiative decay is possible from the upper autoionization states to the $4d^{10}5pns(nd)$ autoionization states converging to both lower ($5p\ ^2P_{1/2}$ and upper ($5p\ ^2P_{3/2}$) resonance levels, so that the radiation is due to DR satellites of the laser lines with λ = 325.0 and 353.6 nm, respectively.

Therefore, the results of our investigation showed that the collisions of low-energy electrons with Cd^+ ions result in intense emission due to the radiative transitions between $4d^9(^2D_{5/2,3/2})5s^2nl$ and $4d^{10}5p(^2P^0_{1/2,3/2})nl$ autoionization states of cadmium atom, representing DR satellites of the laser lines of Cd^+ ion with λ = 325.0 nm ($4d^95s^2\ ^2D_{3/2} \longrightarrow 4d^{10}5p^2P^0_{1/2}$) and λ = 353.6 nm ($4d^95s^2\ ^2D_{3/2} \longrightarrow 4d^{10}5p^2P^0_{3/2}$). The maximum effective cross sections for the electron-induced excitation of these satellites are 4×10^{-17} and 1×10^{-17} cm^2, respectively, and are comparable with the effective cross sections for the excitation of laser lines of the Cd^+ ion [13]. According to our experimental data [13] and the results of *R*-matrix calculations in the close-coupling approximation for 15 channels [14], the upper laser levels $4d^95s^2\ ^2D_{5/2}$ and $4d^95s^2\ ^2D_{3/2}$ are populated in the course of electron–ion collisions predominantly due to the resonance contribution of the autoionization states (resonance excitation). Therefore, it is very important to take into account the radiative decay of these states via DR (competing with the electron decay channel), which may significantly decrease the effective cross section for the resonance excitation.

REFERENCES

1. Yu. Hahn, Rep. Prog. Phys. **60**, 691 (1997).
2. *Atoms in Astrophysics*, Ed. by P. G. Burke, W. B. Eissner, D. G. Hammer, and I. C. Percival (Plenum, New York, 1983).
3. I. S. Aleksakhin, A. I. Zapesochny, and A. I. Imre, Pis'ma Zh. Éksp. Teor. Fiz. **28**, 576 (1978) [JETP Lett. **28**, 531 (1978)].
4. A. I. Zapesochnyĭ, A. I. Imre, I. S. Aleksakhin, *et al.*, Zh. Éksp. Teor. Fiz. **90**, 1972 (1986) [Sov. Phys. JETP **63**, 1155 (1986)].
5. A. N. Gomonai, A. I. Imre, and E. E. Kontrosh, Opt. Spektrosk. **81**, 29 (1996) [Opt. Spectrosc. **81**, 22 (1996)].
6. D. S. Belic, G. H. Dunn, T. J. Morgan, *et al.*, Phys. Rev. Lett. **50**, 339 (1983).
7. J. F. Williams, Phys. Rev. A **29**, 2936 (1984).
8. I. S. Aleksakhin, G. G. Bogachev, I. P. Zapesochny, and S. Yu. Ugrin, Pis'ma Zh. Éksp. Teor. Fiz. **40**, 459 (1984) [JETP Lett. **40**, 1287 (1984)].
9. *Handbook of Lasers*, Ed. by A. M. Prokhorov (Sov. Radio, Moscow, 1978), Vol. 1.
10. A. N. Gomonai, Opt. Spektrosk. **94**, 538 (2003) [Opt. Spectrosc. **94**, 488 (2003)].
11. M. W. D. Mansfield, Proc. Phys. Soc. London, Sect. A **362**, 129 (1978).
12. M. W. D. Mansfield and M. M. Murnane, J. Phys. B **18**, 4223 (1985).
13. A. N. Gomonai and A. I. Imre, Pis'ma Zh. Tekh. Fiz. **27** (18), 89 (2001) [Tech. Phys. Lett. **27**, 798 (2001)].
14. O. I. Zatsarinny and L. O. Bandurina, Opt. Spektrosk. **89**, 546 (2000) [Opt. Spectrosc. **89**, 498 (2000)].

Translated by P. Pozdeev

Technical Physics Letters, Vol. 31, No. 5, 2005, pp. 394–396. Translated from Pis'ma v Zhurnal Tekhnicheskoĭ Fiziki, Vol. 31, No. 9, 2005, pp. 76–82.

Theory of Self-Magnetically Insulated Vacuum Transmission Lines

S. Ya. Belomyttsev, A. V. Kirikov, and V. V. Ryzhov*

Institute of High-Current Electronics, Siberian Division, Russian Academy of Sciences, Tomsk, Russia

** e-mail: ryzhov@to.hcei.tsc.ru*

Received October 26, 2004

Abstract—It is assumed that vacuum transmission lines in the self-magnetic insulation regime feature a limiting current, whereby the trajectories of electrons at the wave front arriving at the anode are tangent to the surface. Under this assumption, the law of energy conservation in the system provides an equation for the relativistic factor γ_m corresponding to the voltage at the outer boundary of the electron layer that can be used for determining the main characteristics of a transmission line in the self-magnetic insulation regime. © *2005 Pleiades Publishing, Inc.*

An important problem in high-current electronics, which has been studied for several decades, is related to determining the parameters of self-magnetically insulation waves (SMIWs) propagating in homogeneous vacuum transmission lines (Fig. 1). In a line featuring such waves, the electron emission from the cathode proceeds in the regime of unlimited emissivity. As a result, a current-carrying electron layer is formed in the SMIW near the cathode surface. The main characteristics of a transmission line in the self-magnetic insulation regime (total current I, cathode current I_C, and leak current I_L) are determined by the voltage drops across the wave, U, and across the electron layer, U_m (or by the corresponding relativistic factor $\gamma_m = 1 + eU_m/mc^2$, where e is the electron charge, m is the electron mass, and c is the velocity of light in vacuum).

In most papers devoted to the theory of magnetically insulated transmission lines (MITLs), the relativistic factor γ_m is determined using the condition of minimum current, according to which a certain minimum current $I = I_{\min}(U)$ exists at given voltage U that provides self-magnetic insulation in the line [1]. In this study, γ_m is determined from an analysis of the SMIW front, considered as a factor controlling the self-magnetic insulation regime. This analysis yields an equation for γ_m, which is obtained using the law of energy conservation in the system. An analogous result is obtained using the law of conservation of the longitudinal component of momentum.

Consider a SMIW propagating in a vacuum coaxial transmission line. Since the polarity of electrodes is insignificant, let the inner tube serve as the cathode (Fig. 1). The results will be applicable to a planar line as well.

We assume that the SMIW front shape does not change with time and that the electron layer behind the front is homogeneous and can be described by solutions obtained in the hydrodynamic approximation [2]. Let us describe the SMIW front in an inertial frame K' moving at a velocity V_f (equal to that of the wave front) relative to the laboratory frame K. In the moving frame, the SMIW front is stationary, the potential difference between electrodes is zero, and electrons emitted from the cathode with a tangential velocity equal to V_f strike the anode at the same velocity. In the limiting case, which corresponds to a limiting current $I = I_{\lim}$ in the SMIW (limiting current approximation), the trajectories of all electrons arriving at the anode with the SMIW front are tangent to the anode surface. Thus, in the K' frame, the velocity of electrons at the anode surface is opposite to that on the cathode surface.

In the limiting current approximation ($I = I_{\lim}$), we may readily calculate the electron energy on the anode in the laboratory inertial frame K. Then, the anode current yields the power transferred with the SMIW to the anode. The difference between the SMIW power and the power transferred to the anode is the energy density per unit length multiplied by the SMIW front velocity V_f.

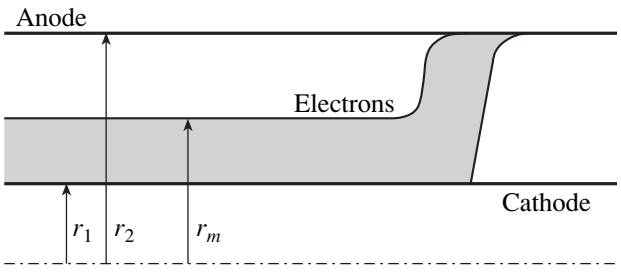

Fig. 1. Schematic diagram of the MITL: r_1 is the cathode radius, r_2 is the anode radius, r_m is the outer radius of the electron layer.

1063-7850/05/3105-0394$26.00 © 2005 Pleiades Publishing, Inc.

This provides a relation between U and γ_m, from which we can determine the relativistic factor as a function of the voltage, $\gamma_m(U)$, in the limiting current approximation.

In the hydrodynamic approximation, the electric and magnetic fields in the electron layer are given by the expressions [2]

$$E_r = H_C r_1 r^{-1} \sinh(\alpha \ln r/r_1),$$

$$H_\theta = H_C r_1 r^{-1} \cosh(\alpha \ln r/r_1),$$

where H_C is the magnetic field strength at the cathode surface, $\alpha = eH_C r_1/mc^2$, and r_1 is the cathode radius (Fig. 1). The average electron velocity V_b and the relativistic factor γ_m are expressed as

$$V_b = c(\gamma_m - 1)^{1/2}/(\gamma_m + 1)^{1/2},$$

$$\gamma_m = \cosh(\alpha \ln(r_m/r_1)),$$

where r_m is the outer radius of the electron layer (Fig. 1). The current in the electron layer is $I_b = I(\gamma_m - 1)/\gamma_m$, the cathode current is $I_C = I/\gamma_m$, and the total current is

$$I = I_b + I_C = \frac{H_C r_1 c}{2}\gamma_m = \frac{I_0 \gamma_m}{2\ln(r_2/r_1)} \times [\ln(\gamma_m + (\gamma_m^2 - 1)^{1/2}) + (\Gamma - \gamma_m)(\gamma_m^2 - 1)^{-1/2}], \quad (1)$$

where $I_0 = mc^3/e \approx 17$ kA and $\Gamma = 1 + eU/mc^2$.

A relation between γ_m and Γ is usually established using the condition of minimum of the total current in the SMIW [1]:

$$dI/d\gamma_m = 0,$$

which yields

$$\ln(\gamma_{m\,\min} + (\gamma_{m\,\min}^2 - 1)^{1/2}) = (\Gamma - \gamma_{m\,\min})(\gamma_{m\,\min}^2 - 1)^{-3/2}. \quad (2)$$

Let us find a relation between γ_m and Γ corresponding to the law of energy conservation. The energy flux (i.e., power) through the SMIW cross section in a homogeneous region is

$$W = IU = I_0 H_C r_1 \gamma_m (\Gamma - 1)/2 \quad (3)$$

while the energy density per unit length in the MITL (including the kinetic energy of electrons and the field energy in the electron layer and in the gap between this layer and the anode) is

$$\varepsilon = \frac{I_0 H_C r_1}{4c}\left[2\gamma_m(\gamma_m^2 - 1)^{1/2} + \frac{(2\gamma_m^2 - 1)(\Gamma - \gamma_m)}{(\gamma_m^2 - 1)^{1/2}} - 2(\gamma_m^2 - 1)^{1/2} + \ln(\gamma_m + (\gamma_m^2 - 1)^{1/2})\right]. \quad (4)$$

The SMIW velocity

$$V_f = c(\gamma_m^2 - 1)^{1/2}(\Gamma - 1)(\Gamma\gamma_m - 1)^{-1} \quad (5)$$

is greater than the average electron velocity V_b in the layer. Therefore, the current I_C is partly spent to charge the electron layer, while the residual (leak) current passes to the anode:

$$I_L = I_C - I_b(V_f/V_b - 1) = H_C r_1 c(\Gamma + \gamma_m^2 - \gamma_m - 1)/2(\Gamma\gamma_m - 1). \quad (6)$$

In the limiting current approximation, the velocity of electrons arriving at the anode with the current I_L is (according to the relativistic rule of addition) $V_1 = 2V_f/(1 + V_f^2/c^2)$. The corresponding relativistic factor is

$$\gamma_1 = (1 - V_1^2/c^2)^{-1/2} = \frac{(\gamma_m^2 - 1)(\Gamma - 1)^2 + (\Gamma\gamma_m - 1)^2}{(\Gamma\gamma_m - 1)^2 - (\gamma_m^2 - 1)(\Gamma - 1)^2}. \quad (7)$$

Therefore, the power transferred by the current I_L to the anode is

$$W_1 = I_0 I_L(\gamma_1 - 1)/c = I_0 H_C r_1(\Gamma + \gamma_m^2 - \gamma_m - 1)(\gamma_1 - 1)/2(\Gamma\gamma_m - 1). \quad (8)$$

According to the energy conservation law,

$$W - W_1 = \varepsilon V_f. \quad (9)$$

Substituting expressions (3)–(5) and (8), we eventually obtain the following relation between γ_m and Γ in the limiting current approximation ($I = I_{\lim}$):

$$2\gamma_{m\,\lim}(\Gamma - 1) - 2(\gamma_1 - 1) \times (\Gamma + \gamma_{m\,\lim}^2 - \gamma_{m\,\lim} - 1)/(\Gamma\gamma_{m\,\lim} - 1) = (\Gamma - 1)(2(\gamma_{m\,\lim})^2(\Gamma - 1) - \Gamma - \gamma_{m\,\lim} + 2 + (\gamma_{m\,\lim}^2 - 1)^{1/2}\ln(\gamma_{m\,\lim} + (\gamma_{m\,\lim}^2 - 1)^{1/2}))/(\Gamma\gamma_{m\,\lim} - 1), \quad (10)$$

where γ_1 is given by formula (7).

Figure 2 shows the plots of $\gamma_{m\,\lim}$ versus voltage U according to relation (10). For comparison, we also present a curve of $\gamma_{m\,\min}(U)$ calculated using relation (2)

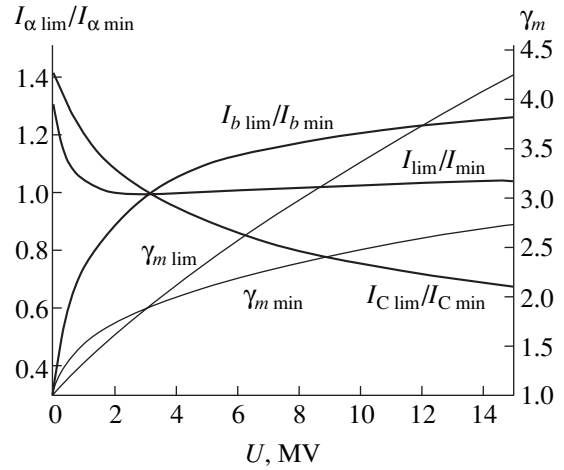

Fig. 2. Plots of the MITL characteristics calculated in the limiting current approximation (subscript "lim") and minimum current approximation (subscript "min") versus the voltage in SMIW: thin lines show the relativistic factor γ_m corresponding to the potential at the boundary of the electron layer; thick lines show the ratios of the total currents (I), the currents via the cathode tube (I_C) and the currents via the electron layer (I_b) in the two approximations.

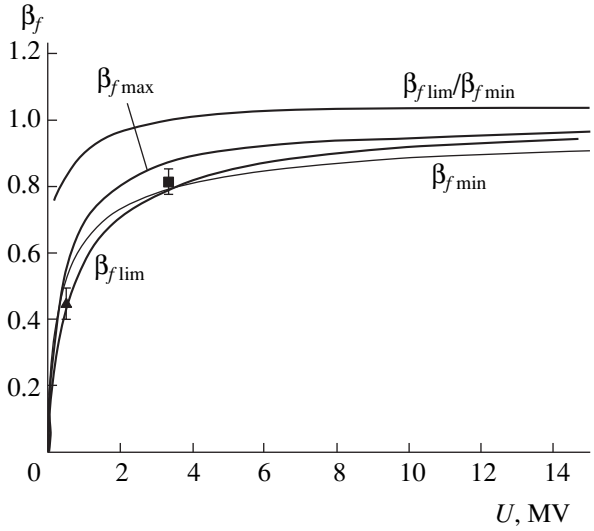

Fig. 3. Plots of the reduced velocity $\beta_f = V_f/c$ of the SMIW front versus voltage in the SMIW: $\beta_{f\,\mathrm{lim}}$ and $\beta_{f\,\mathrm{min}}$ were calculated in the limiting and minimum current approximations, respectively; $\beta_{f\,\max} = (\Gamma - 1/\Gamma + 1)^{1/2}$ is the limiting velocity of SMIW corresponding to $\gamma_m = \Gamma$; points show the experimental data for (▲) U = 0.46 MV [3] and (■) U = 3.4 MV [4] (data taken from [5]).

derived in the minimum current approximation ($I = I_{\mathrm{min}}$). As can be seen, the values of γ_m and, hence, of the voltage U_m across the electron layer in the two cases are substantially different. This difference leads to a significant increase in the current transferred via the electron layer at the expense of a decrease in the cathode current. At the same time, the impedance Z of the transmission line also changes, but not as significantly. The impedance Z_{lim} calculated in the limiting current approximation exhibits a decrease within several tens of percents in the region of low voltages (a 10% decrease at U = 0.5 MV) and within several percents at high voltages (a 5% decrease at U = 15 MV) as compared to the results of calculations (Z_{min}) in the minimum current approximation.

Figure 3 shows plots of the reduced velocity $\beta_f = V_f/c$ of the SMIW front versus voltage in the SMIW. The calculations were performed using formula (5) in the two approximations developed for the determination of γ_m. The maximum difference (up to 20%) between the front velocities in the two cases is observed in the region of low voltages, where the limiting current approximation gives lower values of β_f. For comparison, Fig. 3 also presents a plot of the limiting front velocity versus voltage as described by formula (5) with $\gamma_m = \Gamma$: $\beta_{f\,\max} = (\Gamma - 1)^{1/2}/(\Gamma + 1)^{1/2}$. The results of calculations are compared to the experimental data for β_f measured at U = 0.46 MV [3] and U = 3.4 MV [4] (data taken from [5]). Both theoretical curves agree well with the velocity measured at U = 3.4 MV (in the vicinity of this point, the two curves intersect in Fig. 2). However, the experimental value of β_f obtained at U = 0.46 MV fits better to the curve calculated using the limiting current approximation.

Thus, a comparison of the results obtained in the limiting current approximation to those obtained using the minimum current approximation showed that both methods give close values for total current of MITL (Fig. 2). However, the values of γ_m in the two cases differ to a greater extent, which can be used for experimental verification of the approximation proposed in this paper.

Acknowledgments. The authors are grateful to A.A. Kim for fruitful discussion of the results of this investigation.

This study was supported by the Russian Foundation for Basic Research (project no. 05-02-17754).

REFERENCES

1. L. I. Rudakov, M. V. Babykin, A. V. Gordeev, *et al.*, *Generation and Focusing of High-Current Electron Beams* (Énergoatomizdat, Moscow, 1990).
2. A. V. Gordeev, Zh. Tekh. Fiz. **48**, 784 (1978) [Sov. Phys. Tech. Phys. **23**, 463 (1978)].
3. E. I. Baranchikov, A. V. Gordeev, Yu. V. Koba, *et al.*, in *Proceedings of the 6th IAES Conference on Plasma Physics and Controlled Thermonuclear Reactions, Berchtesgaden, 1976.*
4. I. D. Smith, P. Champney, and J. M. Creedon, in *Proceedings of the International Pulsed Power Conference, New York, 1976*, pp. IIC 8–11.
5. J. W. Poukey and K. D. Bergeron, Appl. Phys. Lett. **32**, 8 (1978).

Translated by P. Pozdeev

Technical Physics Letters, Vol. 31, No. 5, 2005, pp. 397–399. Translated from Pis'ma v Zhurnal Tekhnicheskoĭ Fiziki, Vol. 31, No. 9, 2005, pp. 83–88.

Autoionization Resonances in Outer-Shell *p*-Electron Photoionization Cross Sections of Alkali Metal Atoms

M. A. Kulov, N. O. Vasetskaya, and V. K. Ivanov*

St. Petersburg State Polytechnical University, St. Petersburg, Russia

** e-mail: ivanov@tuexph.stu.neva.ru*

Received December 20, 2004

Abstract—New results of many-electron calculations of the outer-shell *p*-electron photoionization cross sections for rubidium and cesium atoms are presented. The resonance structure of these cross sections, related to the excitation of the autoionization sates $ns^1np^6(n+1)s^1mp$ ($m = n+1, n+2, n+3, \ldots$), is analyzed. The many-electron correlations are taken into account within the framework of the random phase approximation with exchange and the many-body perturbation theory. The decisive role of two-electron processes in the formation of resonance profiles is demonstrated. Differences in the behavior of electrons with various spin moment projections are traced. © *2005 Pleiades Publishing, Inc.*

In recent years, investigations into the photoionization phenomena involving outer-shell electrons in atoms and ions have attracted the attention of both experimentalists [1–4] and theorists (see [4–6] and references therein). Of special interest in this respect is the range of absorbed photon energies close to the inner-shell excitation threshold. Due to the excitation of such inner-shell electrons to quasi-discrete autoionization states, the photoionization cross sections of external electrons acquire resonance profiles. Since the process responsible for the formation of such resonances exhibits a substantially many-electron character, a theoretical description of this phenomenon requires that many-electron correlations [7] be correctly taken into account.

In this study, a numerical method based on the many-body perturbation theory (MBPT) was used for the investigation of a Rydberg series of autoionization resonances $ns \longrightarrow (n+1, n+2, n+3, \ldots)p$ in rubidium (Rb) and cesium (Cs) atoms whose experimental spectra were recently reported by Koide *et al.* [2, 3].

The electronic structure of alkali metal atoms, comprising a closed electron shell with an additional (unpaired) outer *s* electron, is conveniently written within the framework of the spin-polarized approximation as $1s\uparrow 1s\downarrow \ldots ns\uparrow ns\downarrow np^3\downarrow (n+1)s\uparrow$, where arrows specify the electron spin projections. When the energy of the incoming photon is close to the energy of excitation of one of the following transitions,

$$ns\uparrow ns\downarrow np^3\uparrow np^3\downarrow (n+1)s\uparrow \longrightarrow ns\downarrow np^3\uparrow np^3\downarrow (n+1)s\uparrow mp\uparrow,$$

or

$$ns\uparrow ns\downarrow np^3\uparrow np^3\downarrow (n+1)s\uparrow \longrightarrow ns\uparrow np^3\uparrow np^3\downarrow (n+1)s\uparrow mp\downarrow,$$

the direct photoionization of *p* electrons (from *np* shells) competes with the resonance photoionization (with excitation of an autoionization state). The interference of these photoionization channels leads to the formation of an asymmetric profile in the photoionization cross section of the *np* shell, which is described in terms of the Fano parametrization as [5]

$$\sigma(\varepsilon) = \sigma_0\left(1 - \rho^2 + \rho^2\frac{(q+\varepsilon)^2}{\varepsilon^2+1}\right). \quad (1)$$

Here, $\varepsilon = 2(\omega - \tilde{\omega}_s)/\gamma$ is the dimensionless deviation from the resonance energy (measured in the resonance halfwidths $\gamma/2$); ω and $\tilde{\omega}_s$ are the photon energy and the renormalized resonance energy, respectively; σ_0 is the cross section calculated without allowance for the resonance; q is the profile index; and ρ^2 is a parameter determining the resonance depth. All the parameters are determined by the photoinduced transition amplitudes and the matrix elements of the effective electron–electron interaction [1, 5]. Thus, the resonance parameters depend on the approximation used for the calculation of these matrix elements.

The first-order approximation for calculations of the transition amplitudes and the matrix elements of interaction is offered by the random phase approximation with exchange (RPAE), which takes into account the contribution due to correlations related to the excitation

1063-7850/05/3105-0397$26.00

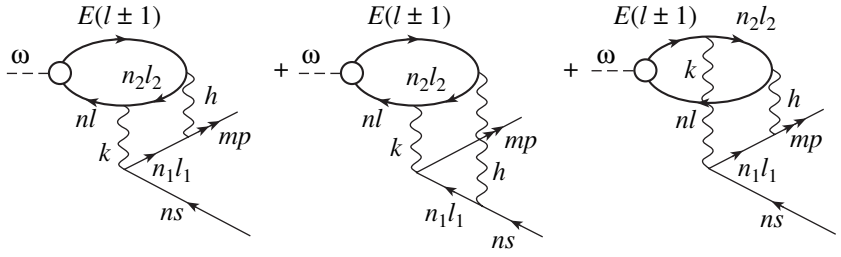

Fig. 1. The Goldstone diagrams corresponding to the excitation amplitude with allowance for the screening effect (see text for explanations).

of a single electron–hole pair at each moment. The basis set of single-particle wave functions and energies was obtained upon correction of the Hartree–Fock basis set by means of the Dyson equation method (DEM) for the self-energy part of the hole propagator [5, 6]. The DEM takes into consideration the dynamic polarization of atomic electrons, which leads to better agreement between calculated excitation energies and the experimental data [2, 3]. The RPAE procedure takes into account the interactions involving seven channels of photoionization from the outer shells: $ns\uparrow(ns\downarrow) \longrightarrow Ep$, $np\uparrow(np\downarrow) \longrightarrow Ed$, $np\uparrow(np\downarrow) \longrightarrow Es$, and $(n + 1)s\uparrow \longrightarrow Ep$ (where E is the electron energy in the final state).

Previously, it was established [1, 5–7] that allowance for the correlations related only to RPAE and the dynamic polarization effects is insufficient for adequate description of the cross section in the vicinity of analogous resonances in the atoms of noble gases. This is related to the fact that "weak" amplitudes of the discrete $ns \longrightarrow mp$ excitations in the RPAE become comparable with the amplitude of the second-order MBPT, which is beyond the RPAE framework and takes into account dynamic screening of the interaction of the excited electron and a hole due to excitation of the second ("strong) electron–hole pair (e.g., $np \longrightarrow Ed$).

Figure 1 shows the Goldstone diagrams corresponding to the excitation amplitude with allowance for the screening effect. Here, the time axis points to the right; the dashed line corresponds to the incoming photon; the rightward (leftward) arrow corresponds to the particle (hole); the wavy line corresponds to the Coulomb interaction between electrons; a circle at the vertex corresponds to the transition amplitude with all RPAE correlations taken into account; k and h refer to the orbital momentum transfer; n and l are the principal and orbital quantum numbers of the outer-shell electron, respectively; and n_1l_1 and n_2l_2 are the possible intermediate states. The total contribution of these processes to the amplitude is obtained by summing all diagrams over the possible (k, h, n_1l_1, n_2l_2) sets and including the exchange diagrams. As expected, the maximum correction is obtained when a "strong" $np \longrightarrow Ed$ channel is excited in the intermediate state. Analogous corrections must be taken into account for the matrix elements of the effective electron–hole interaction determining the resonance width, in which case the RPAE dipole vertex

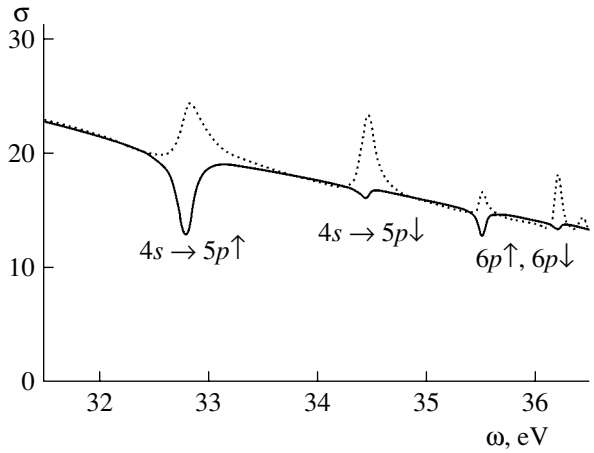

Fig. 2. The photoionization cross section of the outer 4*p* electron shell of Rb in the vicinity of the $4s \longrightarrow mp$ autoionization resonance: dashed profile is calculated using the RPAE, solid profile corresponds to the RPAE with allowance for two-electron processes.

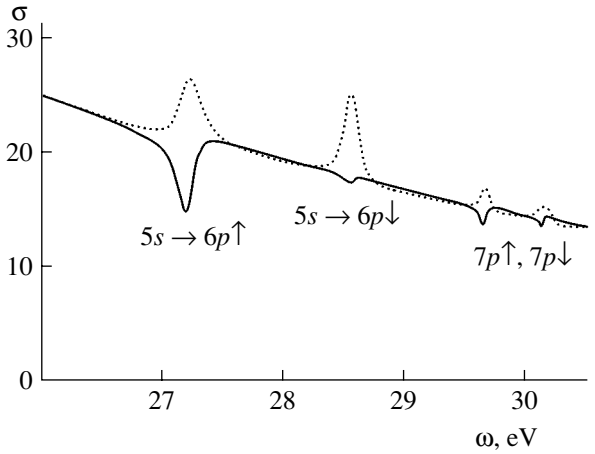

Fig. 3. The photoionization cross section of the outer 5*p* electron shell of Cs in the vicinity of the $5s \longrightarrow mp$ autoionization resonance: dashed profile is calculated using the RPAE, solid profile corresponds to the RPAE with allowance for two-electron processes.

Parameters of autoionization resonances in Rb and Cs atoms

Rb	RPAE		RPAE + screening		Experiment [3]	
	q	γ, eV	q	γ, eV	q	γ, eV
$4s \longrightarrow 5p\uparrow$	2.70	0.210	0.05	0.180	0.11 ± 0.05	0.16(5)
$4s \longrightarrow 5p\downarrow$	7.07	0.119	0.32	0.100	0.4 ± 0.1	0.1(2)
$4s \longrightarrow 6p\uparrow$	6.45	0.028	0.09	0.080	0.12 ± 0.02	0.10(3)
$4s \longrightarrow 6p\downarrow$	19.1	0.020	0.41	0.062	–	–
Cs	RPAE		RPAE + screening		Experiment [3]	
	q	γ, eV	q	γ, eV	q	γ, eV
$5s \longrightarrow 6p\uparrow$	6.16	0.185	0.23	0.162	0.26 ± 0.01	0.15(1)
$5s \longrightarrow 6p\downarrow$	–24.9	0.102	0.38	0.082	0.5 ± 0.1	0.06(1)
$5s \longrightarrow 7p\uparrow$	–28.4	0.028	0.27	0.057	–	–
$5s \longrightarrow 7p\downarrow$	–29.2	0.030	0.44	0.039	–	–

is replaced by the matrix element of the electron–electron interaction according to the RPAE diagram.

Figures 2 and 3 present the results of calculations of the outer-shell *p*-electron photoionization cross sections for Rb and Cs atoms, respectively, in the vicinity of the resonance. Within the framework of the RPAE, the resonances in both Rb and Cs atoms appear as small asymmetric peaks. However, the experiments showed shallow "windows" in these cross sections [2, 3]. Allowance for the dynamic screening processes dramatically changes the resonance parameters (widths, depths, and profile indices). The resonance parameters for the first two resonances, $ns\uparrow \longrightarrow mp\uparrow$ and $ns\downarrow \longrightarrow mp\downarrow$, in Rb and Cs atoms are presented in the table. The resonance profiles are qualitatively different from those obtained in the RPAE and show much better agreement between theory and experiment [2, 3].

In conclusion, we have demonstrated that high-order many-electron processes play a determining role in the formation of autoionization resonances in alkali metal atoms. Only jointly taking into account the dynamic polarizability of the many-electron system (RPAE), the dynamic polarization (DEM), and the dynamic screening can provide for a satisfactory agreement between theory and experiment.

Acknowledgments. This study was supported by the Ministry of Education of the Russian Federation, project nos. E02-3.2-267 and A03-2.9-332.

REFERENCES

1. P. Van Kampen, G. O'Suillivan, V. K. Ivanov, *et al.*, Phys. Rev. Lett. **78**, 3082 (1997).
2. M. Koide, F. Koike, R. Wehlitz, *et al.*, J. Phys. Soc. Jpn. **71**, 1676 (2002).
3. M. Koide, F. Koike, T. Nagata, *et al.*, J. Phys. Soc. Jpn. **71** (11), 1 (2002).
4. A. Neogi, E. T. Kennedy, J.-P. Mosnier, *et al.*, Phys. Rev. A **67**, 042707 (2003).
5. V. K. Ivanov and M. A. Kulov, Proc. SPIE **5127**, 31 (2003).
6. M. A. Kulov, N. O. Vasetskaya, and V. K. Ivanov, Proc. SPIE **5400**, 50 (2004).
7. M. Ya. Amusia and A. S. Kheifets, Phys. Lett. A **82A**, 407 (1981).

Translated by P. Pozdeev

Technical Physics Letters, Vol. 31, No. 5, 2005, pp. 400–402. Translated from Pis'ma v Zhurnal Tekhnicheskoĭ Fiziki, Vol. 31, No. 9, 2005, pp. 89–94.

New Formulation of the Transparent Boundary Conditions for the Parabolic Equation

M. Yu. Trofimov

Pacific Institute of Oceanology, Russian Academy of Sciences, Far-Eastern Division, Vladivostok, Russia
e-mail: dominus@poi.dvo.ru

Received December 28, 2004

Abstract—New approximate transparent boundary conditions for the nonstationary parabolic (Schrödinger) equation are derived using the method of multiple scales. *© 2005 Pleiades Publishing, Inc.*

This paper is devoted to the construction of transparent boundary conditions for the nonstationary Schrödinger equation

$$iu_x + \beta(x)u_{yy} + \nu(x, y)u = 0, \qquad (1)$$

where subscripts x and y denote the partial derivatives with respect to the corresponding variable. This equation appears as an approximate model for description of diffraction and wave propagation in the parabolic equation method [1]. Such boundary conditions need to be defined on the boundaries of a bounded computational domain for the numerical solution of problems related to unbounded domains. The construction of boundary conditions providing the desired transparency involves separation of the waves arriving to and outgoing from the boundary. In the available literature, this is achieved either by factorization of the equation, whereby it is represented as a product of terms describing waves propagating in one direction (see, e.g., [2] for the wave equation), or by matching a solution obtained inside the computation domain with a solution for the free space existing outside this domain and satisfying certain radiation conditions [3].

As is known, approximate description of the unidirectional propagation of waves is provided by the Wentzel–Kramers–Brillouin (WKB) method (or the ray technique) [4], which can be classified as the method of multiple scales [5]. The possibility of simultaneous description of the waves propagating in various directions is retained due to the nonlinearity of the Hamilton–Jacobi (eikonal) equation for the phase variable. These properties of ray solutions make them applicable to the formulation of approximate transparent boundary conditions.

In order to implement this approach to Eq. (1), let us follow the generalized method of multiple scales [5]. According to this, we introduce slow variables $X = \epsilon x$, $Y = \epsilon y$ and the fast variable $\eta = (1/\epsilon)\theta(X, Y)$, where ϵ is a small parameter; pass to the prolonged derivatives

$$\frac{\partial}{\partial x} \longrightarrow \epsilon\frac{\partial}{\partial X} + \theta_X\frac{\partial}{\partial \eta}, \quad \frac{\partial}{\partial y} \longrightarrow \epsilon\frac{\partial}{\partial Y} + \theta_Y\frac{\partial}{\partial \eta};$$

and substitute the expansion

$$u = u_0 + \epsilon u_1 + \ldots.$$

Separating the terms with respect to powers of ϵ, we obtain at $O(\epsilon)$ the representation

$$u_0 = A(X, Y)\exp((i/\epsilon)\theta(X, Y)) \qquad (2)$$

and the Hamilton–Jacobi equation for the phase θ (assumed in this paper to be real):

$$\theta_X + \beta(\theta_Y)^2 - \nu = 0; \qquad (3)$$

The solvability condition of the equation for u_1 at $O(\epsilon^1)$ is

$$iA_X + i\beta\theta_Y A_Y + i\beta(\theta_Y A)_Y = 0. \qquad (4)$$

Multiplying Eq. (3) by $(1/\epsilon)A\exp((i/\epsilon)\theta)$ and adding the product to Eq. (4) multiplied by $\exp((i/\epsilon)\theta)$, we obtain

$$u_{0X} + 2\beta\theta_Y u_{0Y} - \frac{1}{\epsilon}i\beta(\theta_Y)^2 + \beta\theta_{YY}u_0 - \frac{1}{\epsilon}i\nu u_0 = 0.$$

Returning to the initial variables and introducing the wavenumber $k = \theta_Y$ (which is $O(\epsilon^0)$), we eventually arrive at the equation

$$u_{0x} + 2\beta k u_{0y} - i\beta k^2 u_0 + \beta k_y - i\nu u_0 = 0. \qquad (5)$$

Although Eq. (5) is of the first order, the system of equations (3)–(5) is capable of describing the refraction and reflection of waves at the boundaries of the $\{(x, y)|y = \text{const}\}$ type, because Eq. (3) (which is quadratic in θ_Y) has solutions corresponding to waves propagating in both the positive and negative directions of

the y axis. Deducing by the usual way Snell's laws [4] for the system of equations (3)–(5), we conclude, in particular, that the condition of complete transmission of the wave with the phase θ through the boundary under consideration is provided by Eq. (5), while the condition of complete reflection corresponds to the same relation with k replaced by $-k$.

Using Eq. (5) (with u_0 replaced by u) as the approximate transparent boundary conditions and assuming (for simplicity) that the potential ν vanishes at the boundaries, let us pose the initial and boundary value problem for Eq. (1) in the band $\{x, y | x \geq 0, a \leq y \leq b\}$ with the following initial and boundary conditions:

$$u = u_I \quad \text{at} \quad x = 0, \tag{6}$$

$$\begin{aligned} u_x - 2\beta|k|u_y - i\beta k^2 u - \beta|k|_y &= 0 \quad \text{at} \quad y = a, \\ u_x + 2\beta|k|u_y - i\beta k^2 u + \beta|k|_y &= 0 \quad \text{at} \quad y = b. \end{aligned} \tag{7}$$

Here, $k = \theta_Y$ for θ obtained by solving the Cauchy problem for Eq. (3) with the initial condition

$$\theta(X, Y) = \theta_I(Y) \quad \text{at} \quad X = 0, \tag{8}$$

given for all Y. This initial condition appears as a result of representation of the initial data u_I in the rapidly oscillating form

$$u_I = A_I(\epsilon y)\exp((i/\epsilon)\theta_I(\epsilon y)). \tag{9}$$

Of course, this representation is not unique and depends on additional information (used for selecting the small parameter ϵ and for separating the initial condition into the amplitude and rapidly oscillating parts) and on the method of specifying the initial phase for all Y. As for the initial amplitude $A_I(\epsilon y)$, it can be specified by the boundary values on the segment $[a, b]$ so that $A_I(\epsilon y) = A_I(\epsilon a)$ for $y < a$ and $A_I(\epsilon y) = A_I(\epsilon b)$ for $y > b$.

The use of boundary conditions (7) can be illustrated by calculations performed for the numerical simulation of a Gaussian beam

$$u(x, y) = \sqrt{\frac{x_0}{x + x_0}}\exp\left(i\frac{y^2 - yx_0(2y + px)}{4(x + x_0)}\right). \tag{10}$$

Such a beam, considered in [3], is an exact solution of Eq. (1) with $\beta = 1$ and $\nu = 0$.

Taking $x_0 = -ia$ with a real $a > 0$, we write the initial condition as

$$u_I = u(0, y) = \exp\left(-\frac{y^2}{4a}\right)\exp\left(-i\frac{py}{2}\right)$$

and select the initial phase as

$$\theta_I = \theta(0, y) = -\frac{1}{2}py. \tag{11}$$

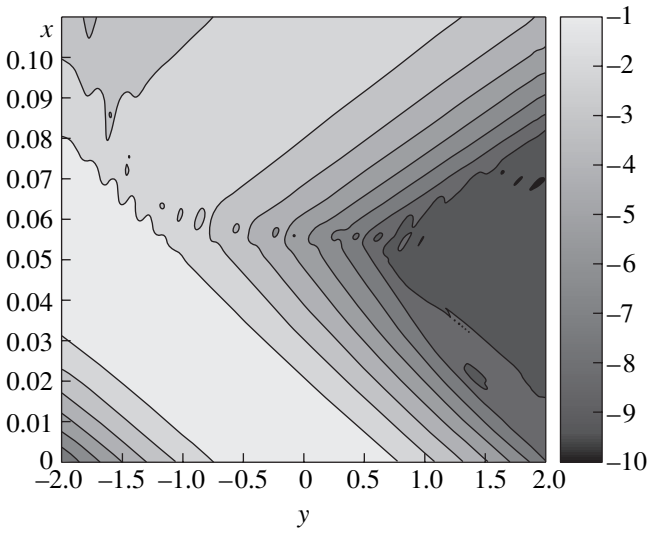

Fig. 1. Isolines of $\log_{10}(|u|)$ obtained upon calculations with boundary conditions (7).

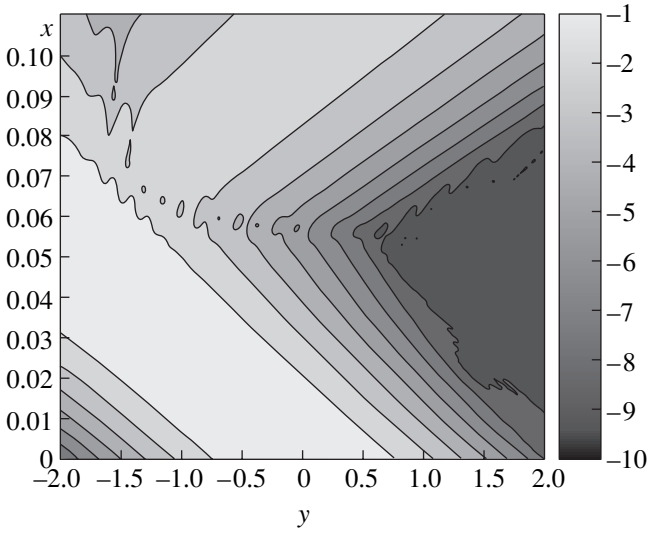

Fig. 2. Isolines of $\log_{10}(|u|)$ obtained upon calculations with boundary conditions formulated according to Baskakov and Popov [3].

A solution to the Cauchy problem for the Hamilton–Jacobi equation (3) with the initial condition (11) is as follows (see, e.g., [6]):

$$\theta(x, y) = \min_{\xi}\left(\frac{(y - \xi)^2}{4x} - \frac{1}{2}p\xi\right) = -\frac{1}{2}py - \frac{1}{4}p^2x. \tag{12}$$

Let us use this solution to formulate the boundary condition of type (7). In this example, the problem of selecting a small parameter and introducing slow variables is not encountered because the small parameter in representation (2) in the case of a linear phase (12) is canceled.

Calculations were performed using the Crank–Nicholson difference scheme [7] for a Gaussian beam with the parameters $a = 1/16$ and $p = 2/0.05$. The results of these calculations presented in Figs. 1 and 2 show satisfactory quality of the boundary conditions of type (7).

In conclusion, it is necessary to make some comments on the issues not considered above. First, one can readily obtain the boundary conditions corresponding to subsequent orders in ϵ by using simple recurrent relations. Second, the initial and boundary value problem posed by Eqs. (6) and (7) is only conditionally well posed. The condition of well posedness consists in a limited growth of the angle of u as a complex number.

The proposed method is simple to implement in cases when an exact or approximate solution of the Cauchy problem for the Hamilton–Jacobi equation is known in analytical form. For an appropriate selection of scales, such solutions can be obtained by approximating the potential ν in Eq. (3) by the potential of zero radius. The applicability of this approach is confirmed by the results of numerical experiments.

Acknowledgments. This study was supported by the Federal Program according to project no. 10002-251/P-17/026-387/190504-301.

REFERENCES

1. V. M. Babic and V. S. Buldyrev, *Asymptotic Methods in Short-Wave Diffraction Theory* (Nauka, Moscow, 1972; Springer-Verlag, Berlin, 1991).
2. B. Engquist and A. Majda, Math. Comput. **31**, 639 (1977).
3. V. A. Baskakov and A. V. Popov, Wave Motion **14**, 123 (1991).
4. Yu. A. Kravtsov and Yu. I. Orlov, *Geometrical Optics of Inhomogeneous Media* (Nauka, Moscow, 1980).
5. A. H. Nayfeh, *Perturbation Methods* (Wiley, New York, 1973).
6. V. P. Maslov, Usp. Mat. Nauk **42** (3), 39 (1987).
7. D. Potter, *Computational Physics* (Wiley, New York, 1973).

Translated by P. Pozdeev

Technical Physics Letters, Vol. 31, No. 5, 2005, pp. 403–404. Translated from Pis'ma v Zhurnal Tekhnicheskoĭ Fiziki, Vol. 31, No. 10, 2005, pp. 1–4.

The Effect of a Dielectric Coating on the Surface Energy of Thin Metal Films of the Al–Li Alloy System

V. A. Sozaev* and R. A. Chernyshova

Kabardino-Balkarian State University, Nalchik, Kabardino-Balkaria, Russia

** e-mail: sozaevv@kbsu.ru*

Received November 11, 2004

Abstract—The surface energy σ of a thin film of an equiatomic binary alloy $Al_{0.5}Li_{0.5}$ contacting with a dielectric medium is calculated using the method of electron density functional. It is established that the difference $\Delta\sigma = \sigma_0 - \sigma(\varepsilon)$ (σ_0 is the initial surface energy and ε is the permittivity) is an almost linear function of ε^{-1}.

The influence of dielectric media on the surface properties of metal alloys remains incompletely studied. However, such data are necessary for the development of both active and passive elements of micro- and nanoelectronic devices, chemical energy converters, capillary energy accumulators, etc. Of special interest in this respect are the surface characteristics of alloys of the Al–Li system, which are widely used in various applications. These alloys are known to exhibit thermostimulated and radiation-enhanced segregation of the light component (lithium) at the free surface [1, 2]. The Al–Li alloys are inconvenient objects for experimental investigations because both alloy components belong to light elements that are difficult to detect. In this context, it is of interest to study the surface characteristics of Al–Li alloys by theoretical methods.

In this paper, the surface energy of a thin film of an Al–Li alloy in contact with a dielectric medium is determined using the method of electron density functional.

The model of a phase boundary and the method of calculation have been described elsewhere [3]. Assuming that the dielectric medium is the same on both sides of the film ($\varepsilon_1 = \varepsilon_2 = \varepsilon$), the surface energy of the film in the jelly approximation can be expressed as

$$\sigma_j = \frac{1}{2}\int_0^\infty \varphi(z)[n_-(z) - n_+(z)]dz$$
$$+ 0.3(3\pi^2)^{2/3}\int_0^\infty [n_-^{5/3}(z) - n_+^{5/3}(z)]dz$$
$$-0.75(3/\pi)^{1/3}\int_0^\infty [n_-^{4/3}(z) - n_+^{4/3}(z)]dz \qquad (1)$$
$$- 0.056\int_0^\infty \left[\frac{n_-^{4/3}(z)}{0.079 + n_-^{1/3}(z)} - \frac{n_+^{4/3}(z)}{0.079 + n_+^{1/3}(z)}\right]dz$$
$$+ \frac{1}{72}\int_0^\infty \frac{|\nabla n_-(z)|^2}{n_-(z)}dz + C_{xc}(r_s)\int_0^\infty \frac{|\nabla n_-(z)|^2}{n_-^{4/3}(z)}dz.$$

Here, $C_{xc}(r_s) = (2.702 - 0.174r_s)10^{-3}$; $r_s = (4/3\pi n_-)^{-1/3}$; $n_-(z)$ and $n_+(z)$ are functions describing the distribution of the positive and negative charge, respectively; φ(z) is the electrostatic potential at the phase boundary [3]. The first term in relation (1) reflects the contribution of the intrinsic electrostatic interaction in the electron gas and the interactions of this electron gas with the jelly charge and a positive charge in the adsorption layer (this term depends on the Gibbs coordinate); the second term corresponds to the contribution that is due to the kinetic energy of the noninteracting electron gas; the third term is a Weizsácker–Kirzhnits correction to the kinetic energy, which is related to the inhomogeneity of the field; the fourth and fifth terms reflect the contributions to σ_j that are due to the exchange and correlation interactions, respectively; and the sixth term is a nonlocal correction to the exchange–correlation interaction in the Geldart–Resolt approximation.

The computational procedure included minimization of the surface energy through variation of the parameter β and the surface concentration x_s at a 0.001 step. The accuracy of calculation of the Gibbs coordinate R_G and the surface energy σ was 10^{-5} and 10^{-3}, respectively. The first approximation corresponded to the absence of surface charging.

As an example, we have estimated the surface energy of the films of an equiatomic binary alloy $Al_{0.5}Li_{0.5}$ with a thickness of $L = 10a_0$ and $15a_0$, where a_0 is the radius of the first Bohr orbit. An analysis of the results of calculations showed that an increase in the

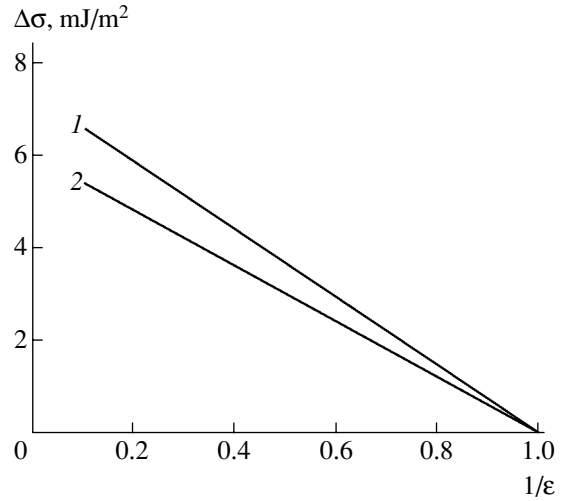

Plots of the difference $\Delta\sigma = \sigma_0 - \sigma(\varepsilon)$ versus inverse permittivity $1/\varepsilon$ of a dielectric medium for $Al_{0.5}Li_{0.5}$ alloy films with a thickness of $L = 10a_0$ (*1*) and $15a_0$ (*2*).

permittivity of the medium and/or in the film thickness leads to a decrease in the surface energy. This behavior is analogous to that reported previously for the films of alkali metal alloys [3]. According to estimates, growth in the $Al_{0.5}Li_{0.5}$ film thickness is also accompanied by enhanced "pulling" of the electron density from the film into dielectric and by increased segregation of lithium at the alloy film surface.

Thus, a decrease in the surface energy of alloy films in contact with a dielectric medium is explained primarily by the action of two factors: (i) "pulling" of the electron density from the film into the dielectric and (ii) segregation of lithium (the component possessing a lower surface energy) at the alloy film surface. As can be seen from the figure, the difference $\Delta\sigma = \sigma_0 - \sigma(\varepsilon)$ (σ_0 is the initial surface energy) for $Al_{0.5}Li_{0.5}$ films with a thickness of $L = 10a_0$ and $15a_0$ is a linear function of $1/\varepsilon$. Estimates of the separate terms contributing to the surface energy show that the maximum contribution to σ_j is due to the kinetic (σ_k), exchange (σ_a), and electrostatic (σ_c) components.

Conclusions. (i) At a given thickness of a metal alloy film (in the absence of surface charging), the external dielectric medium influences the surface energy by "pulling" the electron density from the film toward the dielectric and by increasing the segregation of a component with minimum surface energy.

(ii) The surface energy of an $Al_{0.5}Li_{0.5}$ alloy film decreases (i.e., the adhesion energy increases) with increasing thickness of the film and permittivity of the medium, by analogy with the behavior of the films of alkali metal alloys.

(iii) For $Al_{0.5}Li_{0.5}$ alloy films, the difference $\Delta\sigma = \sigma_0 - \sigma(\varepsilon)$ is virtually a linear function of the inverse permittivity $1/\varepsilon$ of the medium.

REFERENCES

1. G. G. Bondarenko and S. P. Kucheryavyĭ, Fiz. Khim. Obrab. Mater., No. 1, 132 (1991).
2. A. Yu. Lozovoĭ, P. A. Korzhavyĭ, A. V. Ponomoreva, and Yu. Kh. Vekilov, Materialovedenie, No. 1, 43 (1997).
3. V. A. Sozaev, R. A. Chernyshova, and D. V. Yaganov, Izv. Akad. Nauk, Ser. Fiz. **68**, 657 (2004).

Translated by P. Pozdeev

Technical Physics Letters, Vol. 31, No. 5, 2005, pp. 405–407. Translated from Pis'ma v Zhurnal Tekhnicheskoĭ Fiziki, Vol. 31, No. 10, 2005, pp. 5–10.

The Effect of Intense Plastic Deformation on the Mechanical Properties and Substructure of Copper Modified by Dispersed HfO_2 Nanoparticles

V. I. Betekhtin*, K. V. Betekhtin, A. G. Kadomtsev, and S. A. Pul'nev

Ioffe Physicotechnical Institute, Russian Academy of Sciences, St. Petersburg, 194021 Russia

** e-mail: Vladimir.Betekhtin@mail.ioffe.ru*

Received January 13, 2005

Abstract—The effect of intense plastic deformation in the course of rolling on the temperature dependence of the ultimate strength of copper containing dispersed HfO_2 nanoparticles was studied. The results of thermoactivation analysis of the experimental data showed that the introduction of HfO_2 particles did not change the activation energy and, hence, the mechanism of fracture. The presence of dispersed nanoparticles is manifested primarily by an increase in the thermal stability of copper subgrains and their mutual misorientation. This leads to increasing thermal stability of the strength. Rolling significantly influences the elastic modulus of the dispersion-strengthened composite. © *2005 Pleiades Publishing, Inc.*

As is known, the intense plastic deformation of metals containing dispersed oxide nanoparticles improves the mechanical properties of such composites and, what is especially important, increases the thermal stability of these properties. In recent years, much attention has been devoted to investigations of the properties of materials subjected to intense plastic deformation by means of equichannel angular pressing and shear under pressure (see, e.g., [1–4]). The effects of deformation by rolling are studied to a much lesser extent.

This Letter presents the results of an investigation of the effect of deformation by rolling on the mechanical properties of copper containing dispersed HfO_2 nanoparticles.

The experiments were performed with Cu–HfO_2 composite samples prepared from single crystals of a Cu–0.8 wt % Hf solid solution grown using the Stepanov technique, in which the content of Hf was close to the limiting solubility at melting temperature. The oxide (HfO_2) nanoparticles in the copper matrix were formed by means of internal oxidation in the course of annealing of the solid solution at about 1000°C in an oxygen-containing atmosphere [2, 4]. By varying the time of exposure in oxygen, it was possible to control the thickness of a layer containing HfO_2 particles up to a maximum value of 5 mm. The results of electron-microscopic examination showed that the dimensions of HfO_2 particles fall within 10–50 nm.

The composite samples were tested in the state upon intense plastic deformation by room-temperature rolling. The maximum degree of elongation upon rolling was ≈98%.

The temperature dependence of the strength of a composite sample upon ultimate rolling was determined, in comparison to pure copper, by tensile testing to fracture at a constant loading rate of σ = 25 MPa/s. Thermoactivation analysis of this temperature dependence was based on a kinetic approach to fracture [5]. Using this method, we determined the activation energy of fracture (U_0) and the structure-sensitive factor $\gamma = V_0\gamma'$, where V_0 is a characteristic volume (close to the atomic volume) and γ' is a dimensionless coefficient of local stresses arising during deformation of a loaded material. Previously, it was established [6, 7] that the magnitude and thermal stability of γ in metals is determined by the value and temperature dependence of the small-angle misorientation (θ) of subgrains in the samples deformed to fracture at various temperatures (T) and stresses (σ). In this study, the measurements of θ were performed using the method of small-angle X-ray scattering (SAXS) [6].

The Young modulus was determined using the natural frequency of longitudinal oscillations in the samples under conditions of electrostatic excitation. These experiments were performed on a special setup created at the Ioffe Physicotechnical Institute (St. Petersburg) [3].[1]

Experimental results and discussion. The temperature dependence of the strength of ultimately rolled Cu–HfO_2 composite samples is presented in the figure (curve *1*). As can be seen, the stress at break exhibits a linear decrease with increasing temperature. The linear variation of the strength as a function of the temperature indicates that, in the domain of stresses σ, temperatures T, and loading rates $\dot{\sigma}$ studied ($\dot{\sigma}$ is a quantity

[1] The measurements of the Young modulus of composites were performed by Yu.A. Burenkov.

1063-7850/05/3105-0405$26.00 © 2005 Pleiades Publishing, Inc.

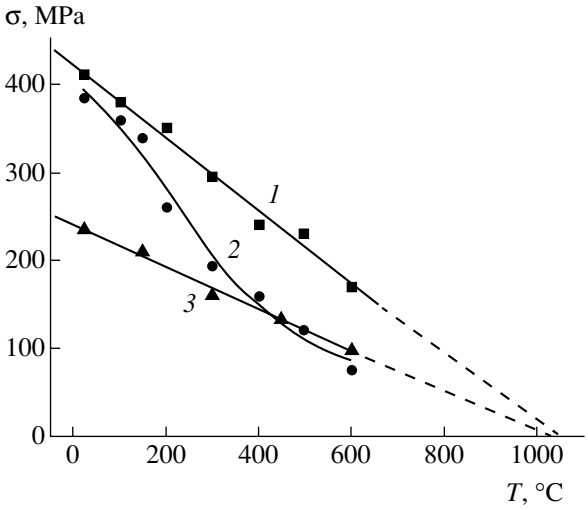

Plots of the strength versus temperature for (*1*) rolled Cu–HfO_2 composite, (*2*) rolled copper, and (*3*) copper annealed upon rolling.

inverse to the lifetime τ), the values of U_0 and γ can be estimated using an expression relating τ to σ and T [5]:

$$\tau = \tau_0 \exp(U_0 - \gamma\sigma/kT). \quad (1)$$

Proceeding from Eq. (1), it was shown [8] that, for $\tau_0 \approx 10^{-13}$ s and $\sigma \approx 10^7$ Pa/s, the

$$U_0 \approx 30kT_0, \quad (2)$$

$$\gamma \approx -30k(\Delta\sigma/\Delta T)^{-1}. \quad (3)$$

Here, k is the Boltzmann constant, T_0 is the temperature obtained by extrapolating the linear dependence of σ on T to intersection with the temperature axis ($\sigma = 0$), and $\Delta\sigma/\Delta T$ is the slope of this linear dependence.

For a correct thermoactivation analysis (in this case, for determining U_0 and γ), it was necessary [9] to check for the identity of a structural factor determining the mechanism of fracture under the given testing conditions (σ, T, $\dot{\sigma}$). As was noted above, such a structural factor in metals is the misorientation of subgrains (θ). We have measured θ by SAXS in the Cu–HfO_2 composite samples deformed to fracture at various temperatures T. It was found that the misorientation is virtually the same ($\theta \approx 80 \pm 7'$) in the entire temperature range studied.

Previously, it was also demonstrated [6, 7] that, while the conservation of γ is determined by the constancy of θ in the samples tested under various conditions (σ and T), the magnitude of γ in a metal occurring in different initial states (annealed and rolled to various degrees, etc.) is inversely proportional to θ. This statement is confirmed by the results of this study. Indeed, the temperature dependence of the strength of copper annealed upon rolling (stabilizing annealing at a temperature above the maximum temperature used in the tensile tests) is also linear (see curve *3* in the figure). The results of SAXS measurements of the misorientation of subgrains in such copper showed that θ is same ($38' \pm 4'$) for the samples tested to fracture at various temperatures. This value is about half that for the Cu–HfO_2 composite. It should be noted that the stress at break for annealed copper and the composite also differ by a factor of about 2.

Thus, the results of structural investigations confirm the correctness of thermoactivation analysis of the temperature dependences of the strength of Cu–HfO_2 composite and annealed copper samples.

Estimates obtained using formula (2) showed that the activation energy of fracture are the same for Cu–HfO_2 composite and annealed copper samples: $U_0 \approx 78$ kcal/mol (as determined by extrapolating the σ versus T plots to intersection with the temperature axis, $\sigma = 0$). This value agrees well with the interatomic interaction energy (sublimation heat) in copper (≈80 kcal/mol), which confirms the key role of the matrix in determining the resistance to fracture in dispersion-strengthened composites. Estimates obtained using formula (3) showed that $\gamma = 1.1$ nm^3 and $\gamma' = 35$ for the Cu–HfO_2 composite and that $\gamma = 2.37$ nm^3 and $\gamma' = 77$ for copper, which confirms the inverse proportionality of γ and γ' to θ established in [6, 7].

Taking into account the aforementioned correlation between θ and γ (or γ'), let us consider the temperature dependence of the strength of rolled copper (see curve *2* in the figure). As can be seen, this dependence is virtually linear in the temperature interval from 18 to 150°C, while the misorientation of subgrains measured in the copper samples tested to fracture is $\approx 80 \pm 7'$, that is, almost the same as that in the samples of rolled Cu + HfO_2 composite (the somewhat greater strength of the composite as compared to that of copper is apparently related to the presence of HfO_2 nanoparticles in the former case). However, at $T > 150$°C, the strength of copper upon rolling becomes significantly lower than that of the Cu–HfO_2 composite. The measurements of misorientation θ showed that the thermal stability of subgrains in copper tested at $T > 150$°C is significantly decreased: in the samples tested to fracture at 200 and 400°C, the misorientation of subgrains is $\theta = 60 \pm 5'$ and $38 \pm 4'$, respectively.

Thus, analysis of the obtained experimental data leads to the conclusion that it is the presence of HfO_2 nanoparticles that provides for the thermal stability of a structure formed upon intense plastic deformation by rolling and, hence, for the thermal stability of the mechanical properties (strength) of the dispersion-strengthened composite material. This conclusion is consistent with the published data on the influence of dispersed oxide nanoparticles on the thermal stability of metals upon intense plastic deformation by means of

equichannel angular pressing [10]. According to these data, the structure of ultradisperse metals is stabilized by oxide particles or second-phase inclusions situated at the grain boundaries and/or at the grain–subgrain interfaces.

Estimates of the effect of rolling on the elastic modulus (E) of Cu–HfO_2 showed that rolling to 50, 75, and 94% decreases the modulus to ≈114.7, ≈93, and ≈85 GPa, respectively, from the initial value $E \approx$ 127 GPa. This decrease in E is significantly more pronounced than that upon equichannel angular pressing of the same composition [3].

Acknowledgments. This study was supported by the Russian Foundation for Basic Research, project no. 03-03-32606.

REFERENCES

1. V. M. Segal, V. I. Reznikov, V. I. Kopylov, D. A. Pavlik, and D. F. Malyshev, *Processes of Plastic Forming in Metals* (Navuka i Tekhnika, Minsk, 1994) [in Russian].
2. A. B. Lebedev, S. A. Pul'nev, V. V. Vetrov, *et al.*, Fiz. Tverd. Tela (St. Petersburg) **40**, 1268 (1998) [Phys. Solid State **40**, 1155 (1998)].
3. A. B. Lebedev, Yu. A. Burenkov, S. A. Pul'nev, *et al.*, Izv. Akad. Nauk, Ser. Fiz. **64**, 381 (2000).
4. V. Y. Gertsman, R. Birringer, and R. Z. Valiev, Scr. Metall. Mater. **30**, 229 (1994).
5. V. R. Regel', A. I. Slutsker, and E. E. Tomashevskiĭ, *Kinetic Nature of Strength of Solids* (Nauka, Moscow, 1974) [in Russian].
6. S. N. Zhurkov, V. I. Betekhtin, and A. I. Slutsker, Fiz. Tverd. Tela (Leningrad) **5**, 1326 (1964) [Sov. Phys. Solid State **5**, 966 (1964)].
7. V. I. Betekhtin, *Problems of Strength and Plasticity in Solids* (Nauka, Leningrad, 1979), pp. 142–154 [in Russian].
8. A. I. Slutsker, V. I. Betekhtin, and J. C. Lee, Acta Mater. **52**, 2733 (2004).
9. V. L. Indenbom and A. N. Orlov, *Thermally Activated Processes in Crystals* (Mir, Moscow, 1973), Vol. 2, pp. 3–22 [in Russian].
10. D. G. Morris and M. A. Morris, Acta Metall. **39**, 1763 (1991).

Translated by P. Pozdeev

Technical Physics Letters, Vol. 31, No. 5, 2005, pp. 408–410. Translated from Pis'ma v Zhurnal Tekhnicheskoĭ Fiziki, Vol. 31, No. 10, 2005, pp. 11–16.

Room-Temperature Ultrasonic Annealing of Radiation Defects in Silicon

A. A. Podolyan[a,*] and V. I. Khivrich[b]

[a] *Kiev National University, Kiev, Ukraine*

[b] *Institute for Nuclear Research, National Academy of Sciences of Ukraine, Kiev, Ukraine*

** e-mail: gogi@mail.univ.kiev.ua*

Received November 23, 2004

Abstract—Room-temperature ultrasonic annealing of point radiation defects in the bulk of silicon is demonstrated for the first time. The radiation defects in single crystal silicon were generated by the exposure to γ radiation from a ^{60}Co source. A qualitative model of processes in the system of radiation defects under the action of ultrasound is proposed. © *2005 Pleiades Publishing, Inc.*

In recent years, much attention has been devoted to using ultrasound as a factor that effectively influences the defect structure of crystalline semiconductors [1–4]. This direction of research is of special importance for silicon microelectronic technology, since the high degree of integration in modern devices requires the development of methods for controlled modification of the composition of defects in the base material. Previously, we demonstrated the possibility of an ultrasonically stimulated redistribution of impurities [3] and modification of the structure of defects (including interstitial silicon atoms) [4] in single crystal dislocation-free silicon.

This Letter reports for the first time on the low-temperature ultrasonic annealing of point defects generated in single crystal silicon by γ quanta from a ^{60}Co source.

The experiments were performed with Czochralski grown *n*-type silicon single crystals with a resistivity of $\rho \approx 400\ \Omega$ cm, which were cut from the central part of the ingot. The samples were mechanically polished using abrasive silicon carbide powders (M40 and M10 grades) and then chemically polished in a standard solution (CP-4). The sample crystal dimensions after preparative treatments were $25 \times 7 \times 1.44$ mm.

Radiation defects were generated by exposure to γ quanta from a ^{60}Co source (the sample temperature during irradiation was $T_{irr} < 50$°C) to a total dose of 5×10^7 rad ($\Phi \approx 8 \times 10^{16}$ cm^{-2}). The concentration of radiation-induced defects was evaluated in terms of the lifetime τ of minority charge carriers in the samples. This parameter, which is sensitive to the defect concentration, was determined using the photoconductivity decay technique [5]. It should be noted that the initial τ values measured upon preparation were approximately the same in all samples.

The ultrasonic treatment (UST) of irradiated samples was effected using ring-shaped piezoceramic transducers featuring radial oscillation modes. The transducers were glued to the samples so that ultrasonic oscillations with a frequency of 10–30 kHz were excited in the direction of the maximum crystal size. The USTs and the measurements of τ were performed at room temperature.

Figure 1 shows the typical plots of the minority carrier lifetime τ versus UST duration for γ-irradiated (curve *1*) and unirradiated (curve *2*) silicon crystals. As can be seen, UST at the selected intensity effectively influences the τ value in the irradiated samples. The observed behavior can be explained by the effect of ultrasound on the concentration of radiative recombination centers generated by the absorbed γ quanta.

Figure 2 presents the results of isochronous (15 min) annealing of a γ-irradiated silicon sample not sub-

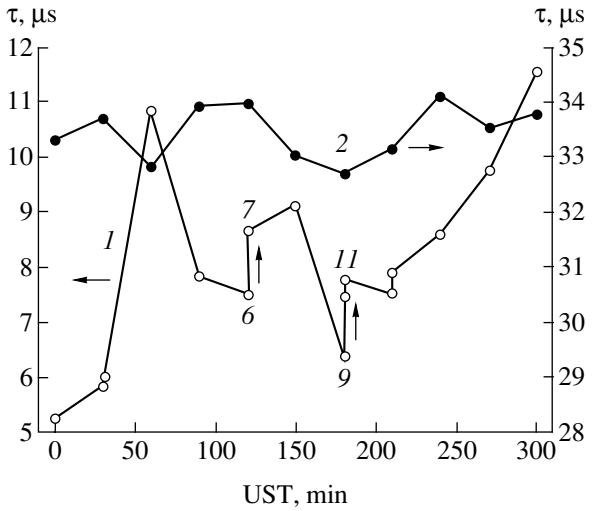

Fig. 1. Typical plots of the minority carrier lifetime τ versus UST duration for (*1*) γ-irradiated and (*2*) unirradiated silicon crystals.

1063-7850/05/3105-0408$26.00 © 2005 Pleiades Publishing, Inc.

jected to any other treatment. The function $f_\tau = (\tau^{-1} - \tau_0^{-1})/(\tau_\Phi^{-1} - \tau_0^{-1})$ is the fraction (normalized to unity) of unannealed radiation defects, where τ_0, τ_Φ, and τ are the minority carrier lifetimes before and after γ-irradiation and in the course of annealing, respectively. It should be noted that the residual radiative recombination centers are annealed in the temperature interval 370–450°C. Therefore, the effect of the A-type centers ($V–O_i$ complexes between vacancies and interstitial oxygen atoms with an acceptor level at $E_c - 0.17$ eV, representing the main radiative recombination centers in Czochralski grown *n*-type silicon [6, 8]) on the minority carrier recombination in the samples studied is insignificant (the A-type centers are completely annealed at ~350°C [6, 7]).

The curve of isochronous annealing depicted in Fig. 2 is similar to the analogous curves reported previously [9, 10]. From this we infer that the main radiative recombination centers in our samples are complexes of the $C–O–V_2$ (carbon–oxygen–divacancy) type introducing an acceptor level ($E_c - 0.45$ eV) into the bandgap [9, 10]. An insignificant negative annealing observed at 260–350°C probably reflects the formation of additional $C–O–V_2$ centers [9, 10] via the interaction of vacancies (liberated as a result of decomposition of the A-type centers unstable at these temperatures) with C_iO_i (interstitial carbon–interstitial oxygen) complexes also formed in significant amounts in irradiated crystals of Czochralski grown *n*-type silicon [8].

A rather complicated variation of the minority carrier lifetime as a function of UST time (Fig. 1, curve *1*) with a general increase in τ is evidence of complex processes in the system of radiation-induced defects under UST conditions. As is known, there are several possible mechanisms favoring the annealing of radiation defects, including (i) the migration of defects to sinks, (ii) the formation of more complicated defects, and (iii) the dissociation of complexes [11].

Apparently, several mechanisms of the annealing of radiation defects are also operative under UST conditions. In the first stage (0–60 min), τ exhibits a growth that reflects a rapid decrease in the concentration of radiative recombination centers. In this stage, the defects are annealed by means of their diffusion to sinks (without dissociation), whereby they lose the recombination activity. The subsequent stage of UST (60–210 min) involves the formation of new recombination centers and their partial annealing, which is reflected by the τ variations observed in this period of time. Keeping the samples for several days at ~25°C was also accompanied by annealing of the newly formed recombination centers (see Fig. 1, jumps *6–7* and *9–11* in curve *1*, indicated by vertical arrows). This behavior can be explained by the ultrasound-stimulated dissociation of radiation defects of one type, followed by the formation of new defects. Indeed, dissociation of

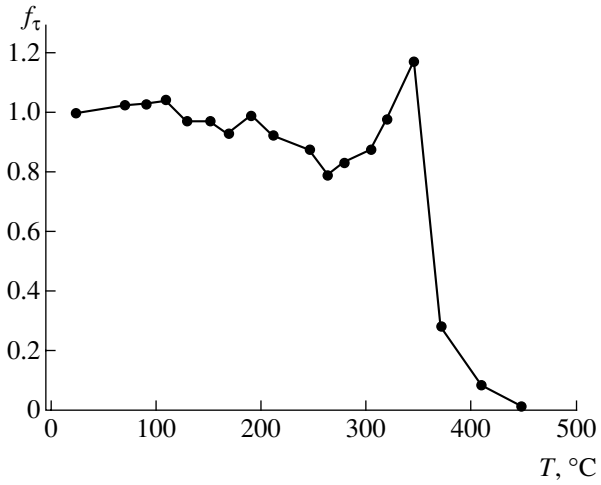

Fig. 2. Variation of the fraction f_τ of unannealed radiation defects in the course of isochronous annealing of a γ-irradiated silicon crystal.

the $C–O–V_2$ complexes may lead to the formation of new recombination-active defects, such as the A-type centers and complexes unstable at room temperature; for example, VB (vacancy–substitution boron) complexes at $E_v + 0.43$ eV [6, 7]. The appearance of such defects leads to a decrease in τ and explains the observed room-temperature annealing with jumps in τ. In the final stage (210–300 min), UST leads to a monotonic annealing of the recombination centers that is accompanied by an increase in τ. This annealing proceeds more smoothly than that in the initial stage (Fig. 1, curve *1*). The final UST stage involves dissociation of the residual recombination-active defects formed upon decomposition of the $C–O–V_2$ complexes.

It should be emphasized that the proposed model of annealing of the radiative recombination centers under the action of ultrasound is rather schematic. Further detailed investigations are necessary in order to elucidate the true picture of events in irradiated silicon under UST conditions. However, in this study, it was most important to experimentally establish the possibility of low-temperature annealing of the radiation-induced point defects of one type in silicon under the action of ultrasound.

Acknowledgments. The authors are grateful to T.I. Kibkalo and V.F. Lastovetskii (Institute for Nuclear Investigations) and A.B. Nadtochiy (Department of Physics, Kiev National University) for their help in preparation and UST of silicon samples.

REFERENCES

1. S. S. Ostapenko, L. Jastrebski, J. Lagowski, and B. Sopori, Appl. Phys. Lett. **65**, 1555 (1994).
2. Y. Koshka, S. Ostapenko, T. Ruf, and J.-M. Zhang, Appl. Phys. Lett. **69**, 2537 (1996).

3. I. V. Ostrovskii, A. B. Nadtochiy, L. P. Steblenko, and A. A. Podolyan, in *Proceeding of the IEEE International Ultrasonics Symposium, Atlanta, GA, 2001*; http://www.ieeeuffc.org/archive/ul/proceed/2001/proceed/u0110401.pdf
4. A. P. Onanko, A. A. Podolyan, and I. V. Ostrovskiĭ, Pis'ma Zh. Tekh. Fiz. **29** (15), 40 (2003) [Tech. Phys. Lett. **29**, 634 (2003)].
5. M. Saritas and H. D. McKell, J. Appl. Phys. **63**, 4561 (1988).
6. I. D. Konozenko, A. K. Semenyuk, and V. I. Khivrich, *Radiation Effects in Silicon* (Naukova Dumka, Kiev, 1974) [in Russian].
7. V. S. Vavilov, V. F. Kiselev, and B. N. Mukashev, *Defects in the Bulk and on the Surface of Silicon* (Nauka, Moscow, 1990) [in Russian].
8. A. S. Zubrilov and S. V. Koveshnikov, Fiz. Tekh. Poluprovodn. (Leningrad) **25**, 1332 (1991) [Sov. Phys. Semicond. **25**, 804 (1991)].
9. P. F. Lugakov, T. A. Lukashevich, and V. V. Shusha, Fiz. Tekh. Poluprovodn. (Leningrad) **13**, 401 (1979) [Sov. Phys. Semicond. **13**, 237 (1979)].
10. I. I. Kolkovskii, P. F. Lugakov, and V. V. Shusha, Phys. Status Solidi A **83**, 299 (1984).
11. J. C. Bourgoin and M. Lannoo, *Point Defects in Semiconductors II: Experimental Aspects* (Springer, Berlin, 1983), Springer Series in Solid-State Science, Vol. 35.

Translated by P. Pozdeev

Technical Physics Letters, Vol. 31, No. 5, 2005, pp. 411–413. Translated from Pis'ma v Zhurnal Tekhnicheskoĭ Fiziki, Vol. 31, No. 10, 2005, pp. 17–23.

A Relativistic Backward Wave Oscillator with a Modulating Resonance Reflector

S. D. Korovin, V. V. Rostov, and E. M. Tot'meninov*

Institute of High-Current Electronics, Siberian Division, Russian Academy of Sciences, Tomsk, Russia

** e-mail: totm@lfe.hcei.tsc.ru*

Received December 23, 2004

Abstract—A high-efficiency relativistic microwave source based on a backward wave oscillator (BWO) with a resonance reflector has been studied by experimental and numerical methods. The BWO is capable of generating 12-ns pulses with a carrier frequency of 9.93 GHz at an output radiation power of 0.75 ± 0.11 GW. For the BWO pumped by a high-current electron beam from a SINUS-6K accelerator, the regime with relatively high pulse-to-pulse stability is characterized by a 40% efficiency of power conversion. © *2005 Pleiades Publishing, Inc.*

This study continues investigations of a backward wave oscillator (BWO) employing a resonance reflector of the backward wave [1, 2]. The previous stages of research were devoted primarily to the task of increasing the efficiency of generation in relatively weak magnetic fields (below the cyclotron resonance level). The aim of this study was to increase the BWO efficiency in the general case of operation with strongly magnetized electron beams.

The proposed BWO scheme has certain features that distinguish it from the traditional variant of a relativistic BWO with below-cutoff waveguide section. These distinctive features include a moderate (by a factor of about 1.5) increase in the transverse size of the slow-wave structure (SWS) and the significant role of the preliminary modulation of electron beam in the region of a lumped resonance reflector. The former factor reduces the relative contribution due to asynchronous waves in the particle–field interaction as compared to the synchronous (–1)st spatial harmonic of the backward wave in a corrugated waveguide, which is important (from the standpoint of the electric strength of SWS) for microwave generation on a high power level. The effective modulation of particles with respect to velocity provides for a selective excitation of the working E_{01} mode, which makes the proposed BWO similar to two-chamber generators with a distributed region of electron bunch retardation (such as, e.g., twistron, for which the theoretical efficiency is as high as 60% [3, 4]). This analogy was confirmed by the results of our previous theoretical and experimental investigations, which showed that the efficiency depends both on the position of the resonance reflector relative to SWS (changing the particle modulation phase relative to that of the synchronous wave) and on the depth of modulation.

For the optimum position of the resonance reflector, whereby the bunch at the SWS entrance occurs near the middle of the retarding phase of the synchronous wave, the calculated efficiency reached 60% in the ultrarelativistic case and was somewhat higher for moderate relativistic energies [2]. However, experimental realization of such regimes is complicated due to a significant increase in the oscillator start current. The results of our previous experimental investigations showed the possibility of generation at 25% efficiency in magnetic fields both below and above the level of cyclotron absorption of the backward wave [1]. The main potential for further development of the BWO scheme is related to the selection of the amplitude and phase of the particle beam modulation near the reflector and optimization of the longitudinal profile of the coupling resistance in SWS. In addition, we have also varied the impedance of the vacuum diode in a high-current electron accelerator in the course of numerical simulation of the BWO operation (Fig. 1).

The optimum modulation depth was selected and the BWO parameters were roughly estimated in the approximation of infinitely narrow gap. The numerical calculations were performed using the approximation of one-dimensional motion without stopping and reversal of particles [2]. The electrodynamic characteristics of SWS and reflector were analyzed and the geometry of the matching element on the SWS collector end was selected using special software based on the scattering matrix method [5]. Subsequent optimization of the BWO geometry was carried out using the fully electromagnetic numerical PIC-code KARAT [6]. The final simulation was performed for an electron beam with a current of 3.9 kA, accelerated by a pulsed voltage with an amplitude of 480 kV. In the final geometry, the coupling resistance was 1.9 Ω over the greater part of the SWS length. The BWO employed a guiding magnetic field with an induction of 3 T. The optimum regime cor-

1063-7850/05/3105-0411$26.00

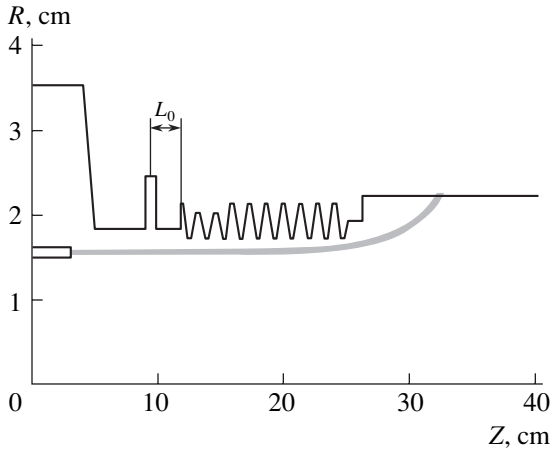

Fig. 1. Schematic diagram of the relativistic BWO with resonance reflector.

responded to the resonance reflector positioned at L_0 = 24 mm relative to the SWS (Fig. 1).

The optimized BWO had a calculated efficiency of 40% for a stationary output power level of 0.75 GW. The rather complicated dynamics of the transient process (Fig. 2) is related to the presence of equiprobable frequencies (8.6 and 10 GHz) in the oscillation spectrum (determined for 0–6 ns sampling times). On the passage to a stationary regime, the system exhibited single-mode generation with the main spectral component at 10 GHz. As the resonance reflector was moved away from the SWS, the time of attaining the stationary regime decreased (due to a decrease in the oscillator start current) and the evidence of competition in the nonlinear stage of the transient process disappeared. At the same time, a shift of the bunch center toward the boundary between accelerating and retarding phases of the synchronous wave field led to a decrease in the BWO efficiency.

The experiments were performed using a nanosecond pulse-periodic electron accelerator of the SINUS-6K type. In the single-pulse regime, the accelerator produced an electron beam with a duration of about 20 ns at a cathode voltage of ≈500 kV and a diode current of ≈4 kA. In these experiments, the BWO with L_0 = 24.5 mm operated in a stable regime with an efficiency of ≈37.5 ± 5% at a working frequency of 9.93 GHz (Fig. 3). The longitudinal magnetic field induction was 2.7 T. The spectrum had a full width at –3 dB level not exceeding 100 MHz. The output microwave power determined by integrating over the radiation pattern was 0.75 ± 0.11 GW. The pulse shape observed in the optimum regime showed evidence of a small fraction (on the order of several percents) of reflected electrons, which was related to their stopping and reversal in a strong high-frequency field in the stationary oscillation regime. The flow of reflected electrons was also observed in the numerical experiment. The standard deviation of the microwave pulse amplitude in the indicated regime was 2–3 times the corresponding value for the amplitude of the accelerating voltage on the cathode.

When the reflector was moved toward the cathode, the reproducibility of pulses was already substantially deteriorated for L_0 = 24.0 mm, whereby the relative scatter of pulse amplitude could exceed 100%. In this regime, output signals with both small and large amplitudes were observed, and the transient process exhibited complicated dynamics (Fig. 4). Taking into account that the carrier frequency in the regime with small microwave pulse amplitude increased to

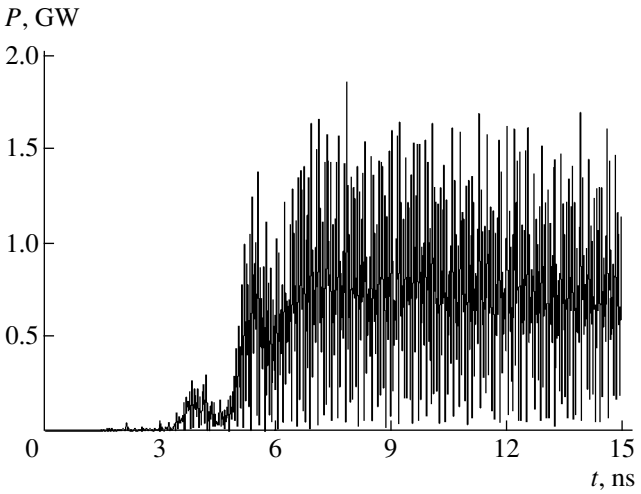

Fig. 2. Typical time series of the output power (non-time-averaged) near the absorber for the BWO simulated in the optimum regime.

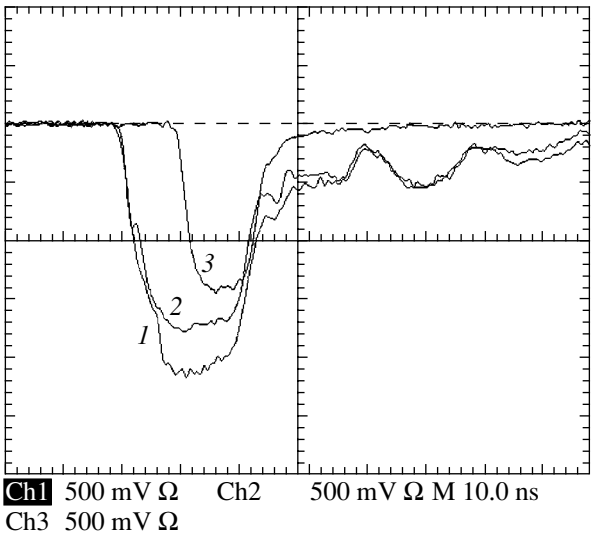

Fig. 3. Typical experimental oscillograms of the (*1*) BWO cathode voltage, (*2*) diode current, and (*3*) microwave detector signal.

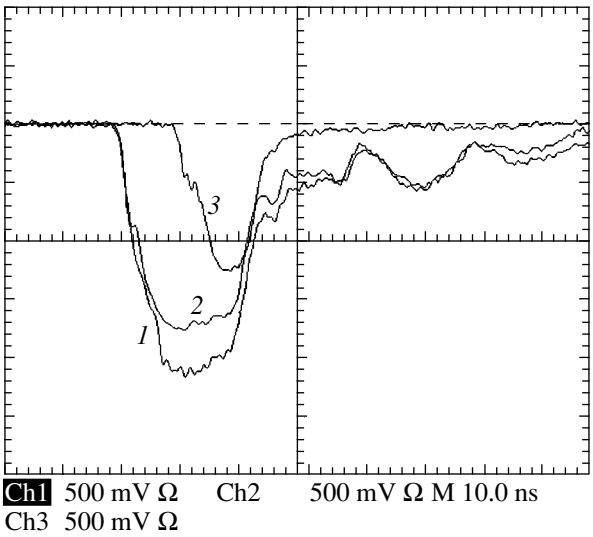

Fig. 4. Same as in Fig. 2, but the detector output voltage pulse *3* was measured with the resonance reflector shifted relative to the optimum position by 0.5 mm toward the SWS.

10.8 GHz, these signals are probably related to resonance oscillations of SWS in the vicinity of the π-type E_{01} mode.

Displacement of the reflector away from the cathode relative to the optimum position (L_0 = 24.5 mm) led to a decrease in the BWO efficiency at a certain increase in the duration of microwave pulses and their reproducibility. Variation of the SWS length for the optimum position of the resonance reflector did not lead to increase in the BWO efficiency. It was also established that an increase in the electron beam power led to a decrease in the efficiency.

Thus, a BWO with the optimum position of the resonance reflector and optimum modulation of particle velocity at the SWS entrance showed an experimental efficiency of 37%. In this optimum regime, further increase in the efficiency is hindered by the nonlinear competition of modes and the excitation of undesired oscillations.

REFERENCES

1. I. K. Kurkan, V. V. Rostov, and E. M. Tot'meninov, Pis'ma Zh. Tekh. Fiz. **24** (10), 43 (1998) [Tech. Phys. Lett. **24**, 388 (1998)].
2. S. D. Korovin, I. K. Kurkan, V. V. Rostov, *et al.*, Izv. Vyssh. Uchebn. Zaved., Radiofiz. **42**, 1189 (1999).
3. N. F. Kovalev, B. D. Kol'chugin, and Z. N. Krotova, Radiotekh. Élektron. (Moscow) **20**, 2636 (1975).
4. N. F. Kovalev, B. D. Kol'chugin, and Z. N. Krotova, Radiotekh. Élektron. (Moscow) **20**, 1309 (1975).
5. G. G. Denisov, D. A. Lukovnikov, and S. V. Samsonov, Int. J. Infrared Millim. Waves **16**, 745 (1995).
6. V. P. Tarakanov, *User's Manual for Code KARAT* (Berkley, Springfield, 1992).

Translated by P. Pozdeev

Technical Physics Letters, Vol. 31, No. 5, 2005, pp. 414–416. Translated from Pis'ma v Zhurnal Tekhnicheskoĭ Fiziki, Vol. 31, No. 10, 2005, pp. 24–29.

Experimental Study of the Converging Density Wave Excitation in a Cylindrical Anode of a High-Current Diode

A. S. Adamenko, S. V. Adamenko, and E. V. Bulyak

Laboratory of Electrodynamic Processes "Proton-21," Kiev, Ukraine

Received August 20, 2004; in final form, December 30, 2004

Abstract—Density waves excited in a cylindrical anode irradiated by a short pulsed high-current electron beam in a relativistic vacuum diode have been experimentally studied. The electron trajectories are almost perpendicular to the side surface of a cylindrical anode coaxial with the cathode. As a result of the discharge, the surface layer of the continuous anode exhibits no visible changes, whereas an inner region of the anode is evaporated. The mechanism of the isentropic wave excitation is elucidated by experiments with a coaxial anode comprising a tube tightly fit to the central rod. According to the most probable explanation, the electron beam induces collapse in the subsurface layer of the anode. © *2005 Pleiades Publishing, Inc.*

In the course of experiments devoted to the energy concentration in solids, we have developed a relativistic pulsed diode with filament electrodes, which is characterized by a specific configuration of the electron flow near the anode. The electron flow in the diode is organized so that the electron trajectories at a cylindrical anode are almost perpendicular to its side surface. This was confirmed by various methods sensitive to energy distribution in the high-energy part of the bremsstrahlung spectrum.

The main parameters of the pulsed electron beam were as follows: electron energy, 250–500 keV; pulse full width at half maximum, 5–20 ns; beam current, 20–70 kA; current density at the anode, 10^5–10^7 A/cm^2. The experimental geometry was as follows. A cylindrical anode was mounted along the diode axis. The flow of accelerated electrons was focused onto the cylindrical surface near the anode tip and struck the anode within a relatively narrow belt with a width on the order of several tens of microns.

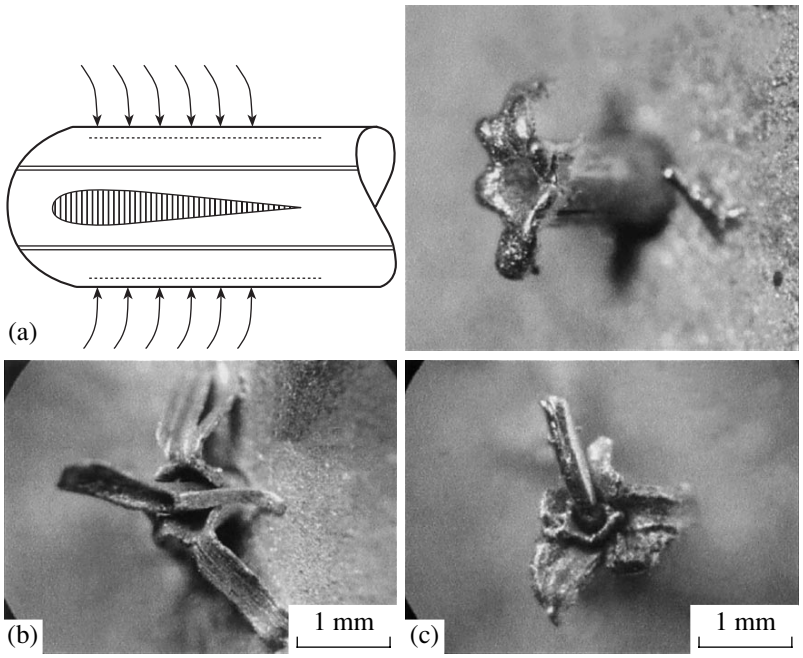

Fig. 1. Schematic diagram of the experiment (top left inset) and the typical micrographs of various anodes upon high-voltage discharge (electron beam pulse duration, 8–10 ns; maximum beam current, 30–50 kA; peak voltage, 350–450 kV): (a) continuous copper anode with a diameter of 0.5 mm; (b) combined copper anode with an outer shell diameter of 0.6 mm and a 0.2-mm inner kernel; (c) combined anode with an outer copper shell diameter of 0.5 mm and an inner 0.2-mm nickel kernel.

1063-7850/05/3105-0414$26.00 © 2005 Pleiades Publishing, Inc.

The electric discharge led to a characteristic fracture of the anode, whereby the outer surface bombarded by accelerated electrons exhibited minimum visible changes. The maximum concentration of thermal energy took place near the anode axis.

We have also performed experiments with combined anodes of coaxial design, comprising a central kernel supporting a tightly fit outer metal cylinder. In such anodes, the character of fracture was somewhat different: in addition to the axial region of high-temperature action (which was smaller in combined anodes than in homogeneous ones), there was outward splitting of fragments of the outer shell. The character of this splitting exhibited no significant dependence on the anode structure, being essentially the same for combined anodes made of identical and dissimilar materials, and for those with continuous or hollow kernels.

Figure 1 presents a schematic diagram of the experiment and shows the typical photographs of anodes upon discharge. Arrows in the top left diagram in Fig. 1a indicate the electron trajectories near the edge of the cylindrical surface facing the cathode; double lines show the interface between the kernel and outer cylinder in combined anodes; and the cross-hatched area in the kernel indicates the region of maximum energy liberation.

The experiments were performed with anodes, both homogeneous and combined, made of various metals, possessing axial symmetry, and having diameters in a range from 100 to 2000 μm. The anodes were irradiated from outside, but they exploded from inside, as can be seen in the microphotographs presented in Figs. 1a–1c. The thickness of flakes split from the anode was 100–300 μm. The metal on the outer surface of such flakes exhibited no significant changes, while the inner surface showed clear evidence of high-temperature action. In homogenous anodes, the maximum energy was liberated in the central region, and the material from these regions was partly evaporated (Fig. 1a). In the case of combined coaxial anodes made of either identical (Fig. 1b) or dissimilar (Fig. 1c) materials with the outer cylinder tightly fit to the kernel, the outer layer always exhibited splitting along the interface.

Our experiments were performed under conditions such that the exciting pulse duration was approximately equal to that of the acoustic pulse: $\tau \approx R/V$, where R is the radial projection of the electron pathlength in the anode and V is the longitudinal sound velocity. Indeed, the radial distribution of the deposited energy (or the density of electron trajectories) in the subsurface layer of the anode according to our calculations (Fig. 2a) is determined by the multiple elastic scattering of electrons on nuclei of the anode material and exhibits a maximum at a depth of 30–70 μm (for a copper anode with a radius of 0.5 mm, in which these effects are most clearly pronounced). The other possible contributions, in particular, due to retardation in the collective electric field and the inelastic scattering effects, were not evaluated, but it can be ascertained that such effects may only reduce the average electron penetration depth. The depth of maximum penetration also decreases with the angle of electron incidence on the surface.

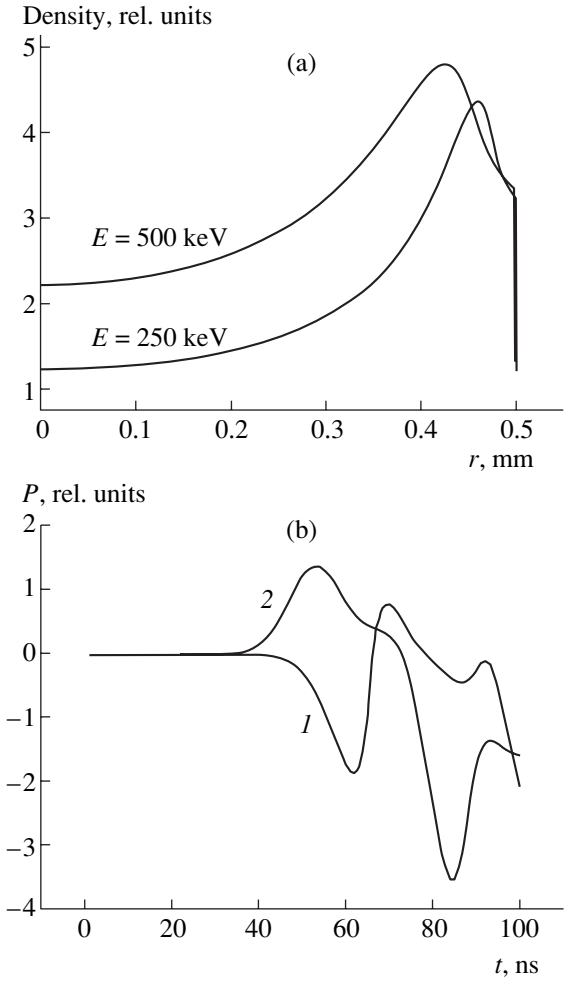

Fig. 2. (a) Radial profile of the density of electron trajectories in a copper cylinder with a radius of 0.5 mm (calculated with neglect of all interactions except elastic scattering); (b) evolution of density waves generated in the case of (*1*) implosion and (*2*) explosion in the surface layer of the node.

Thus, according to our estimates, the main distinctive features of the process studied are as follows:

(i) The distance from the anode surface to the region of maximum heat evolution is at least three times that to the region of maximum electron energy deposition.

(ii) The acoustic pulse duration (defined as the ratio of the energy pulse width in the anode to the longitudinal sound velocity) is approximately equal to the electron beam pulse duration.

(iii) The time of thermal relaxation (leveling of the temperatures of electron and ion subsystems in the surface layer of the anode) is greater than the acoustic pulse duration (see [2]).

A comparison of these estimates to the experimental results leads to the following conclusion. The energy transfer from the electron flow to the region of maximum energy deposition is mediated by a density wave, which is capable of propagating over a distance of several wavelengths without heat evolution (quasi-isentropic regime). This density wave is generated via a nonablative mechanism, since the ablation process involves a direct energy transfer from the primarily excited electron subsystem to the ion subsystem, which requires a relatively large time [2].

There are at least two hypotheses that can be used to describe a nonablative mechanism of density wave generation. Rukhadze [3] suggested that a short intense beam "heats" conduction electrons so that a portion of them leave the surface layer of the metal anode. This violates the charge balance in this layer (the density of positive ions in the crystal lattice becomes greater than the density of conduction electrons), which gives rise to the Coulomb explosion. We may also suggest that the magnetic field of the electron flow is capable of "freezing" conduction electrons. Then, electrons from the beam are added to these conduction electrons and the negative charge density becomes greater than the positive one, which results in the Coulomb implosion (collapse) in the surface layer of the anode. The region of implosion generates rarefaction pulses followed by compression pulses. By contrast, the region of explosion generates compression pulses. If a couple of such pulses propagating toward the axis encounters a discontinuity (interface), an implosion will separate the outer layer from the kernel, while an explosion will fuse the shell into the kernel (Fig. 2b).

To summarize, bombardment of a cylindrical anode by a short intense converging relativistic electron beam gives rise to a converging density wave propagating in the anode material. This wave is capable of transferring the energy without significant losses over a distance of several wavelengths inward the material. The character of fracture observed in combined anodes suggests that a pulse transferring the energy is generated as a result of the Coulomb implosion in the surface layer of the anode.

REFERENCES

1. Yu. V. Sud'enkov and A. I. Pavlishin, Pis'ma Zh. Tekh. Fiz. **29** (12), 14 (2003) [Tech. Phys. Lett. **29**, 491 (2003)].
2. V. M. Bykov, D. I. Vaisburd, M. I. Chebodaev, and A. V. Chernov, Zh. Tekh. Fiz. **74** (4), 77 (2004) [Tech. Phys. **49**, 454 (2004)].
3. A. A. Rukhadze and U. Yusupaliev, Zh. Tekh. Fiz. **74** (4), 127 (2004) [Tech. Phys. **49**, 933 (2004)].

Translated by P. Pozdeev

Technical Physics Letters, Vol. 31, No. 5, 2005, pp. 417–419. Translated from Pis'ma v Zhurnal Tekhnicheskoĭ Fiziki, Vol. 31, No. 10, 2005, pp. 30–34.

Angular Dependence of the Ion Energy, Charge, and Mass Distributions in Surface Discharge Plasma

S. V. Barakhvostov and I. L. Muzyukin

Institute of Electrophysics, Ural Division, Russian Academy of Sciences, Yekaterinburg, 620219 Russia

e-mail: ifd@iep.uran.ru

Received September 2, 2004; in final form, November 15, 2004

Abstract—Previously, the ion energy, charge, and mass distributions in vacuum discharge plasma at the surface of polymeric insulators were studied using an analyzer oriented perpendicularly to the surface, and both multiply charged and high-energy ions were found in the plasma. This Letter presents the first experimental results on the dependence of the ion energy, charge, and mass distributions in the plasma on the particle take-off angle relative to the insulator surface. © *2005 Pleiades Publishing, Inc.*

Experimental. The experiments were performed in a vacuum of 10^{-4} Pa. We have studied the plasma formed at the surface of a high-density poly(ethylene) (HDPE) in discharge initiated by high-voltage pulses with an amplitude of 150 kV, a duration of 3 ns, and a leading front width of ~200 ps. Figure 1 shows a schematic diagram of the experimental setup. In this study, the measurements were performed (unlike our previous study [1]) using a linear scheme. The discharge was initiated between anode *1* and grounded cathode-diaphragm *2*. The plasma was formed at the plane face of an HDPE half-cylinder mounted in an insulating holder on the cathode. The half-cylinder was spaced 10 mm from the cathode-diaphragm and could be rotated about its axis within ±45°, which corresponded to the particle take-off angle varied from 0 to 90° relative to the insulator surface. The cathode had a 1-mm hole and also served the first diaphragm in the collimating system of the energy analyzer.

The energy, mass, and charge distributions in the plasma flow were determined using the Thomson method of parabolas. Charged particles passed via diaphragms *2* and *3* (Fig. 1) and entered the region of parallel electric and magnetic fields (*4*), where the flow of ions was separated with respect to the energy, mass, and charge. Past the deviating system, ions traveled in the free propagation regime to strike microchannel plate (MCP) *5*. The output electron flux from the MCP detector output (proportional to the ion flux at the input) was measured by a CCD matrix, digitized, accumulated over several tens of measurements, and stored in the memory of the personal computer *6*. Each spectrogram was obtained by accumulating the signals from up to 50 discharges. This accumulation allowed components of the ion spectrum not manifested in a single measurement to be revealed. The calculated parabolas were superimposed onto the accumulated experimental spectrograms and the relative ion flow intensities were determined for each region of the parabola. These patterns determined the ion charge, mass, and energy distributions.

Results and discussion. We have determined the ion charge, mass, and energy distributions for five orientations of the insulator surface relative to the analyzer axis. Figure 2 presents the typical spectrograms observed at each value of the particle take-off angle α relative to the insulator surface. In the directions far from the normal (α = 45° and 60°), H^{+1} is the only com-

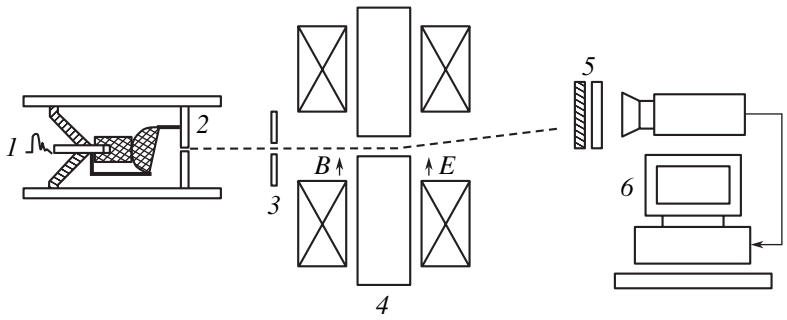

Fig. 1. Schematic diagram of the experimental setup (see text for explanations).

1063-7850/05/3105-0417$26.00 © 2005 Pleiades Publishing, Inc.

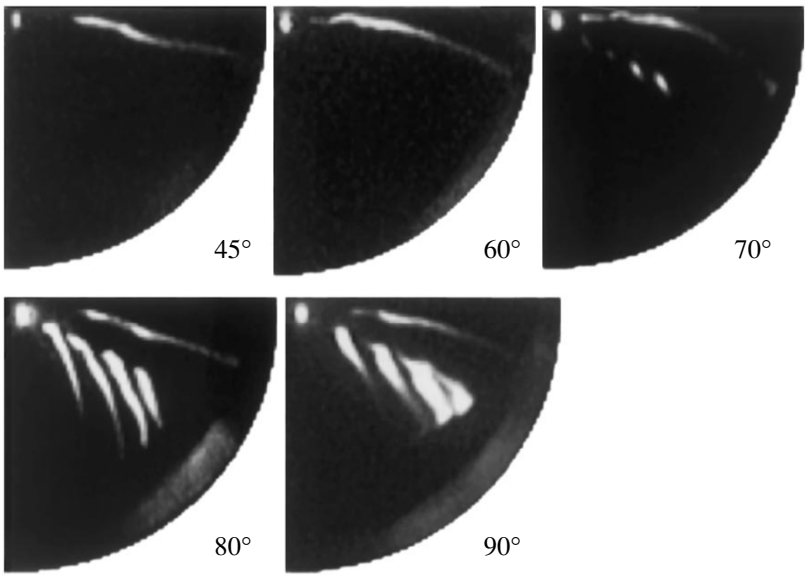

Fig. 2. The typical ion spectrograms measured at various angles α relative to the insulator surface.

ponent in the ion flux. Weak traces of carbon ions appear in the spectrogram measured at α = 70°. At α = 80° and 90°, the intensity of the flow of carbon ions sharply increases and exceeds that of the hydrogen ion component.

It was a rather unexpected observation that the carbon parabolas increased both in brightness and in width: the latter became three times as large as that for hydrogen. The simplest explanation of this behavior is based on the notion about ion beam broadening as a result of electrostatic repulsion between ions traveling in the free propagation regime between the analyzer output and the MCP detector. The velocities of carbon ions are significantly lower than those of hydrogen ions and, hence, the period of time during which the repulsive forces operate is longer in the former case. However, if this were the case, the parabola width for each particular angle would exhibit a clear dependence on the ion velocity, so that the parabola would expand from the center to periphery. Such an expansion was observed neither in this study, nor in the previous experiments [1]. The width of parabolas for all ion fractions was the same, and the relative content of hydrogen ions in the total flow was about 60% in the direction perpendicular to the insulator surface. As can be seen for α = 80°, the carbon parabolas do not expand, and they exhibit equal intensities and relative ion contents.

Another possible explanation proceeds from a difference in the character of acceleration for the ions of light and heavy elements in the plasma expanding into vacuum. According to this explanation, hydrogen ions are accelerated immediately at the insulator surface, while carbon ions are accelerated after passage of the diaphragm (i.e., at distances above 10 mm from the surface). As a result, the imaged area of hydrogen acceleration is restricted to that determined by the 1-mm hole in the diaphragm, whereas carbon ions are collected by the hole within a greater solid angle and then accelerated in the field behind the diaphragm. Thus, the surface area contributing to the total intensity of carbon ions is not limited by the hole and is significantly greater than that for hydrogen ions. This situation may account for the excess of the carbon flow intensity over that of hydrogen ions. Note that this effect is significant

Relative fractions and average energies of ions taken from the discharge plasma at various angles α relative to the insulator surface

α	H^{+1}	C^{+4}	C^{+3}	C^{+2}	C^{+1}
90°	11% 1425 eV	15% 1087 eV	22% 798 eV	24% 795 eV	28% 682 eV
80°	8% 1553 eV	16% 1917 eV	29% 1583 eV	24% 1252 eV	23% 1330 eV
70°	55% 5497 eV	18% 1705 eV	14% 1619 eV	5% 1369 eV	8% 1088 eV
60°	100% 4428 eV				
45°	100% 3671 eV				

only in the vicinity of the direction of maximum intensity (~90°) of the flow of carbon ions relative to the insulator surface. At smaller angles (α = 70°, 60°, and 45°), the intensity of the flow of carbon ions is smaller and the region of acceleration behind the diaphragm is not formed.

Data on the average fractions of hydrogen and carbon ions in the flow for various orientations of the insulator surface are presented in the table. As can be seen from these data, the average energies of ions depend on the ion charge. At the same time, the average energies do not depend in a monotonic manner on the ion take-off angle relative to the surface. Nevertheless, these energies tend to decrease on approaching the direction perpendicular to the insulator surface. The behavior of carbon ions in the directions close to the surface normal shows evidence for a considerable violation of the usual mechanism of plasma expansion. The total ion flow intensity significantly increases on approaching the normal. However, the method of measurements employed cannot provide for a strict quantitative evaluation of the angular dependence of the total ion flow.

Conclusions. The results of our experiments showed that heavier ions exhibit a sharper directivity in the direction perpendicular to the insulator surface. The regions of acceleration of the light and heavy ions occur at different distances from the surface. The region of acceleration for carbon ions may extend to distances in excess of 10 mm.

Acknowledgments. This study was supported by the Russian Foundation for Basic Research (project nos. 02-02-17509 and 02-02-17002).

REFERENCES

1. S. V. Barakhvostov and I. L. Muzyukin, Pis'ma Zh. Tekh. Fiz. **30** (21), 27 (2004) [Tech. Phys. Lett. **30**, 900 (2004)].

Translated by P. Pozdeev

Technical Physics Letters, Vol. 31, No. 5, 2005, pp. 420–422. Translated from Pis'ma v Zhurnal Tekhnicheskoĭ Fiziki, Vol. 31, No. 10, 2005, pp. 35–39.

Effective Electrical Characteristics of a Three-Dimensional Composite Medium

S. V. Khor'kov

Nizhni Novgorod State Technical University, Nizhni Novgorod, Russia

e-mail: priem@nntu.nnov.ru

Received December 20, 2004

Abstract—The electrical characteristics of a three-dimensional composite consisting of components with strongly different conductivities, σ_1 and σ_2, are theoretically described. The quadratic field and current correlators at the percolation threshold are determined, and the distribution of the energy dissipated in the composite between the components is found. The lower limit of the critical index of the nonlinear effective conductivity is estimated. © *2005 Pleiades Publishing, Inc.*

In recent years, much attention has been devoted to the investigation and application of composite materials. Numerous examples of such media are offered by metal–insulator composites, granular materials, metal–polymer composites, etc. The advantage of such inhomogeneous media consists in that their macroscopic characteristics may strongly differ from those of both individual components.

Let us consider a composite comprising a mixture of two materials with strongly different conductivities, σ_1 (metallic component) and σ_2 (dielectric component), and assume that the size of inhomogeneities in the composite is significantly greater than the electron mean free path. Then, the current density $\mathbf{j}$ and the local electric field $\mathbf{e}$ at an arbitrary point of this medium obey the Ohm law

$$\mathbf{j} = \sigma\mathbf{e}. \tag{1}$$

We will also assume that the sample dimensions are such that the effective conductivity σ_{eff} is a self-averaging quantity. Then, the Ohm law for the whole composite can be written as $\langle\mathbf{j}\rangle = \sigma_{\text{eff}}\langle\mathbf{e}\rangle$, where the angle brackets denote averaging over the sample volume. The effective linear conductivity of such a composite at the metal–insulator percolation threshold is described by the universal function

$$\sigma_{\text{eff}} = \sigma_1 h^s, \tag{2}$$

where $h = \sigma_2/\sigma_1$ and s is the critical index. Dykhne [1] determined the exact value of the critical index $s = 1/2$ for any value of h ($0 \le h \le 1$) in a two-dimensional (2D) medium. For a 3D composite, the critical index is exactly determined ($s = 2/3$) only in the case of $h \ll 1$ [2, 3]. This value agrees well with the results of numerical simulations [4].

This study is devoted to the correlators of fields and currents, which determine the effective characteristics of inhomogeneous media. Let us determine the quadratic field correlator $\langle\mathbf{e}^2\rangle$ as a function of the parameter h for a 3D composite. By definition, the average square of the field strength is

$$\langle\mathbf{e}^2\rangle = \frac{\int\mathbf{e}^2 dV}{V}, \tag{3}$$

where V is the composite volume. The integral in relation (3) over the entire system volume reduces to integration over the "metallic" component (characterized by conductivity σ_1 and occupying volume V_1) and the "dielectric" component (σ_2, V_2):

$$\langle\mathbf{e}^2\rangle = \frac{\int\mathbf{e}_1^2 dV}{V} + \frac{\int\mathbf{e}_2^2 dV}{V}. \tag{4}$$

This expression can be rewritten in terms of the average square fields in the different components defined as

$$\langle\mathbf{e}^2\rangle_1 = \frac{\int_{V_1}\mathbf{e}_1^2 dV}{V_1}, \langle\mathbf{e}^2\rangle_2 = \frac{\int_{V_2}\mathbf{e}_2^2 dV}{V_2},$$

so that

$$\langle\mathbf{e}^2\rangle = \frac{V_1}{V}\langle\mathbf{e}^2\rangle_1 + \frac{V_2}{V}\langle\mathbf{e}^2\rangle_2. \tag{5}$$

Equation (5) is valid for arbitrary fractions of components in the composite. At the percolation threshold, this expression yields

$$\langle\mathbf{e}^2\rangle = p_c\langle\mathbf{e}^2\rangle_1 + (1 - p_c)\langle\mathbf{e}^2\rangle_2, \tag{6}$$

1063-7850/05/3105-0420$26.00

where $p_c = V_1/V$ is the critical concentration of the metallic component corresponding to percolation. The results of numerical simulation for the problem of bonds on a simple cubic lattice give $p_c = 0.247$ [5]. The general expression for the effective linear conductivity can be written as

$$\sigma_{eff} = \langle \sigma \mathbf{e}^2 \rangle / \langle \mathbf{e} \rangle^2.$$

Using the formula of correlator splitting, $\langle \mathbf{je} \rangle = \langle \mathbf{j} \rangle \langle \mathbf{e} \rangle$, and Tellegen's theorem [6], one can readily obtain the relation

$$\delta\sigma_{eff} = \langle \delta\sigma \mathbf{e}^2 \rangle / \langle \mathbf{e} \rangle^2. \quad (7)$$

For a two-component composite at the percolation threshold, this relation can be written as

$$\delta\sigma_{eff} = p_c \langle \delta\sigma_1 \mathbf{e}^2 \rangle_1 / \langle \mathbf{e} \rangle^2 + (1 - p_c) \langle \delta\sigma_2 \mathbf{e}^2 \rangle_2 / \langle \mathbf{e} \rangle^2. \quad (8)$$

Using expression (2) with $s = 2/3$ and Eq. (8), we obtain

$$p_c \langle \mathbf{e}^2 \rangle_1 = \langle \mathbf{e} \rangle^2 \frac{h^{2/3}}{3}, \quad (1 - p_c) \langle \mathbf{e}^2 \rangle_2 = \frac{2}{3} \langle \mathbf{e} \rangle^2 h^{-1/3}. \quad (9)$$

Combining relation (6) with Eq. (9) for $h \ll 1$, we eventually arrive at

$$\frac{\langle \mathbf{e}^2 \rangle}{\langle \mathbf{e} \rangle^2} = \frac{2}{3} h^{-1/3} + o(h^{2/3}). \quad (10)$$

By analogy with Eq. (6), the quadratic current density correlator can be written as

$$\langle \mathbf{j}^2 \rangle = p_c \langle \mathbf{j}^2 \rangle_1 + (1 - p_c) \langle \mathbf{j}^2 \rangle_2.$$

Using the Ohm law and formula (9) for $h \ll 1$, we obtain

$$\frac{\langle \mathbf{j}^2 \rangle}{\langle \mathbf{j} \rangle^2} = \frac{h^{-2/3}}{3} + o(h^{1/3}). \quad (11)$$

Note that 2D media obey a strict relation [1]

$$\frac{\langle \mathbf{e}^2 \rangle}{\langle \mathbf{e} \rangle^2} + \frac{\langle \mathbf{j}^2 \rangle}{\langle \mathbf{j} \rangle^2} = \frac{1}{2}\left(h^{-\frac{1}{2}} + h^{\frac{1}{2}} \right),$$

which implies that the currents and fields fluctuate in the same manner. Expressions (10) and (11) show that $\langle \mathbf{e}^2 \rangle$ and $\langle j^2 \rangle$ correlators in a 3D random medium exhibit different dependences on the parameter h.

Now let us find the distribution of the dissipated energy $q = \mathbf{je}$ between components possessing different conductivities. Taking into account that $\langle q \rangle = p_c \langle q \rangle_1 + (1 - p_c) \langle q \rangle_2$ and using Eq. (9) and an expression for the local energy dissipation ($q = \sigma \mathbf{e}^2$), we eventually obtain

$$p_c \langle q \rangle_1 = \frac{\sigma_{eff}}{3} \langle \mathbf{e} \rangle^2, \quad (1 - p_c) \langle q \rangle_2 = \frac{2\sigma_{eff}}{3} \langle \mathbf{e} \rangle^2. \quad (12)$$

These expressions show that heat evolved in a 3D system, in contrast to the 2D case, is distributed inhomogeneously. The dissipated energy density in the dielectric component is twice as large as that in the metallic component.

Because of the chaotic structure of the medium occurring at the metal–insulator percolation threshold, the electric field **e** exhibits strong fluctuations and may significantly exceed the average field $\langle \mathbf{e} \rangle$ in some regions of the composite. This can be seen, for example, from expression (10). In such regions, the electron gas can be significantly heated, which results in violation of the linear relationship (1) between field and current. The results of many experimental investigations showed evidence of an increase in the nonlinear response in inhomogeneous conducting media occurring at the percolation threshold (see, e.g., [8–12]).

Let us estimate the lower limit of the critical index of the nonlinear effective conductivity χ_{eff}. According to [7], this quantity can be expressed as

$$\chi_{eff} = \frac{\langle \chi \mathbf{e}^4 \rangle}{\langle \mathbf{e} \rangle^4}, \quad (13)$$

where $\chi = \chi_1$ and χ_2 are the local nonlinear conductivities of the corresponding components. The effective conductivity is defined as a coefficient in the expansion of the average current $\langle \mathbf{j} \rangle$ with respect to the field $\langle \mathbf{e} \rangle$:

$$\langle \mathbf{j} \rangle = \sigma_{eff} \langle \mathbf{e} \rangle + \chi_{eff} \langle \mathbf{e} \rangle^2 \langle \mathbf{e} \rangle \ldots .$$

Using relation (13), the average over the system can be expressed via average values for the components:

$$\chi_{eff} = \frac{\chi_1 p_c \langle \mathbf{e}^4 \rangle_1}{\langle \mathbf{e}^4 \rangle} + \frac{\chi_2 (1 - p_c) \langle \mathbf{e}^4 \rangle_2}{\langle \mathbf{e}^4 \rangle}.$$

Unfortunately, exact analytical expressions for the correlators $\langle \mathbf{e}^4 \rangle_1$ and $\langle \mathbf{e}^4 \rangle_2$ are not available. However, taking into account that $\langle \mathbf{e}^4 \rangle_i \geq \langle \mathbf{e}^2 \rangle_i^2$ ($i = 1, 2$) and using expression (10), we obtain the relation

$$\chi_{eff} \geq \frac{4}{9} \frac{\chi_2}{(1 - p_c)} h^{-2/3}. \quad (14)$$

By analogy with the 2D case, we may define the critical index ε of the nonlinear effective conductivity via

the relation

$$\chi_{\text{eff}} \propto h^{-\varepsilon}. \quad (15)$$

Comparing relations (14) and (15), we can estimate the lower limit of the critical index as $\varepsilon_{\min} = \frac{2}{3}$ (note that in a 2D randomly inhomogeneous medium $\varepsilon = 1.33$ [13]).

REFERENCES

1. A. M. Dykhne, Zh. Éksp. Teor. Fiz. **59**, 110 (1970) [Sov. Phys. JETP **32**, 63 (1970)].
2. V. A. Kazakov and A. M. Satanin, Phys. Status Solidi B **108**, 19 (1981).
3. V. E. Arkhincheev, Pis'ma Zh. Éksp. Teor. Fiz. **50**, 293 (1989) [JETP Lett. **50**, 325 (1989)].
4. B. Ya. Balagurov and V. A. Kashin, Zh. Éksp. Teor. Fiz. **110**, 1001 (1996) [JETP **83**, 553 (1996)].
5. J. P. Straley, Phys. Rev. B **15**, 5733 (1977).
6. P. Penfield, Jr., R. Spence, and S. Duinker, *Tellegen's Theorem and Electrical Networks: Research Monograph No. 58* (MIT, Cambridge, 1970).
7. D. Stroud and P. M. Hui, Phys. Rev. B **37**, 8719 (1988).
8. M. A. Dubson, Y. C. Hui, M. B. Weissman, *et al.*, Phys. Rev. B **39**, 6807 (1989).
9. Y. Yagil, G. Deutscher, and D. J. Bergman, Phys. Rev. Lett. **69**, 1423 (1992).
10. Y. Yagil and G. Deutscher, Phys. Rev. B **46**, 16115 (1992).
11. Y. Gefen, W. H. Shin, R. B. Laibowitz, *et al.*, Phys. Rev. Lett. **57**, 3097 (1986).
12. R. K. Chakrabarty, K. K. Bardhan, and A. Basu, Phys. Rev. B **44**, 6773 (1991).
13. A. M. Satanin, S. V. Khor'kov, and A. Yu. Ugol'nikov, Pis'ma Zh. Éksp. Teor. Fiz. **62**, 301 (1995) [JETP Lett. **62**, 322 (1995)].

Translated by P. Pozdeev

Technical Physics Letters, Vol. 31, No. 5, 2005, pp. 423–427. Translated from Pis'ma v Zhurnal Tekhnicheskoĭ Fiziki, Vol. 31, No. 10, 2005, pp. 40–50.

Magnetic Flux Penetration into Superconductor in Vortex-Liquid and Vortex-Glass Regimes

I. B. Krasnyuk and Yu. V. Medvedev

Donetsk Physicotechnical Institute, National Academy of Sciences of Ukraine, Donetsk, Ukraine

Received November 1, 2004

Abstract—Magnetic flux penetration into a half-space occupied by a type-II superconductor occurring in a vortex-liquid or vortex-glass state is considered under the assumption that magnetic field exhibits a sharp increase with time (in the blow-up regime) at the interface. It is shown that each phase admits effective localization of magnetic flux in the form of a magnetic wave front, which is stopped at a depth of $x_s \propto e^{-\sigma}\sigma$ in a vortex-liquid regime and at $x_s \propto (2\sigma)^{1/(\sigma+2)}$ in a vortex-glass regime. Here, the parameter $\sigma = U_0/T$ depends on the thermal activation barrier height U_0 and on the temperature T in the vicinity of the melting curve $T_m(B)$ at a given magnetic field induction B. *© 2005 Pleiades Publishing, Inc.*

Introduction. Thermally excited vortex bundles in superconductors are capable of surmounting the pinning barrier by means of hopping conductivity even for $j < j_c$, where j_c is the critical depinning current density. This phenomenon is called magnetic flux creep. If the pinning barrier at $j \longrightarrow 0$ is infinite (whereby the resistivity ρ obeys the condition $\rho(j \longrightarrow 0) \longrightarrow 0$), the superconductor is said to occur in a vortex-glass state, whereas if the barrier is finite ($\rho(j \longrightarrow 0) > 0$), we have a vortex-liquid state [1].

This study is devoted to solving the standard problem of magnetic field penetration into the half-space $x > 0$ in a plane-parallel geometry $B \parallel z$; $E, j \parallel y$; $v \parallel x$, where $v = v_0 e^{-U(j)/T}$ is the vortex velocity (considered below to be close to critical), v_0 is the "microscopic" vortex velocity, U is the activation barrier (independent of the magnetic field B), T is the absolute temperature, and E is the electric field strength.

The problem is solved with a boundary condition corresponding to the so-called blow-up regime [2],

$$b(0, \tau) = b_0(1 - \tau)^m, \quad b(\infty, \tau) = 0, \quad (m < 0), \ \tau > 0,$$

where $b = BH_{c1}$, H_{c1} is the first critical field, $\tau = t/t_0$, and t_0 is the solution lifetime. For $m = 0$ in the regime of viscous flux flow, the problem was considered in [3]; for $m = 0$ in the regime of magnetic flux creep, an analogous problem for the vortex liquid–vortex glass model was studied in [1].

This paper consists of two parts. The first part, devoted to the case of a finite activation barrier (vortex-liquid phase), will show that the aforementioned problem can be reduced to a diffusion equation of the gradient type with a diffusion coefficient proportional to the magnetic field (see Eq. (2) below). In the second part, it will be shown that the vortex-glass phase is described by an equation with nonlinear power σ with respect to the spatial derivative, where $\sigma = U_0/T$ and $U_0 = U(j \longrightarrow 0)$. Such an equation (see Eq. (2) below) was proposed in [1].

According to the vortex-liquid model, the flux flow exhibits effective localization with an infinite velocity of perturbation spreading (Fig. 1). In the vortex-glass model, we obtain a magnetic wave with an immobile point at the front, which is localized within $0 < x < x_0$ during the entire lifetime of the boundary regime (Fig. 2). Magnetic perturbations do not escape from the

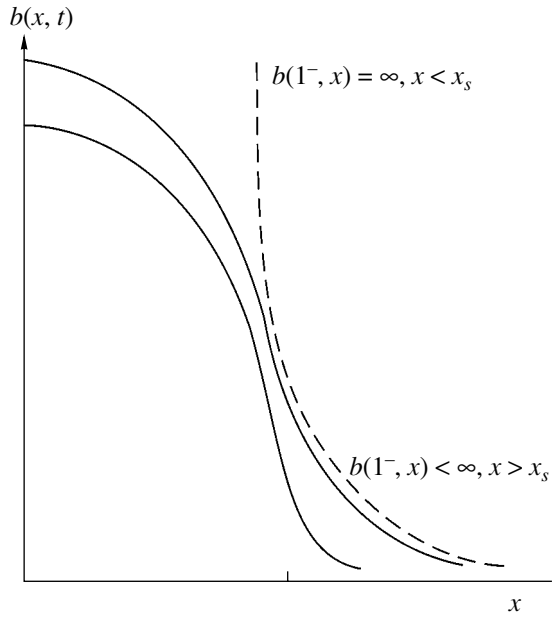

Fig. 1. Effective localization of the magnetic flux, whereby the energy is virtually completely localized within a finite region $\{x < x_s(D, R_0)\}$.

1063-7850/05/3105-0423$26.00 © 2005 Pleiades Publishing, Inc.

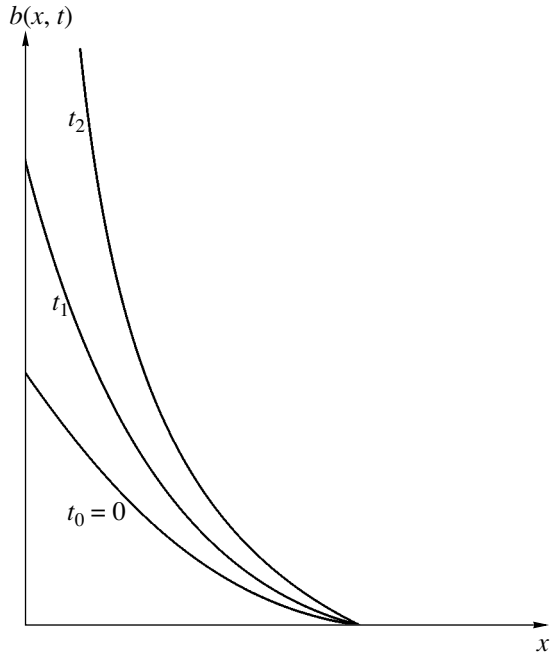

Fig. 2. Evolution of the localized blow-up regime at $t \longrightarrow t_0^-$ for the vortex-glass model ($t_1 < t_2$).

localization region, and the homogeneous magnetic background at $x > x_0$ remains unchanged.

The vortex-liquid regime differs from the vortex-glass one only in that the energy in the former case is almost entirely localized within a finite region $x < x_s$ and the magnetic field to the right of the point x_s is nonzero (but uniformly limited) during the process.

Magnetic flux localization in a vortex-liquid regime. This behavior of the magnetic field can be expected in the case of magnetic flux creep in a vortex liquid at high temperatures $T > T_m(B)$, where $T_m(B)$ is the vortex lattice melting curve [1, p. 1347]. The difference between the vortex-liquid and vortex-glass phases is determined by the parameter

$$\alpha = \left|\frac{\partial U(j)}{\partial j}\right|\frac{\delta j}{T},$$

where δj is the characteristic scale. For $\alpha \ll 1$, the problem is linear and the vortex dynamics exhibits a diffusion character; in the case of $\alpha \gg 1$, we deal with a nonlinear boundary-value problem for a vortex-glass phase, with a power boundary regime for $m > 0$ and a blow-up regime for $m < 0$ (with a boundary condition of the type presented above) [2].

According to the Anderson–Kim model with a finite activation barrier, the nonlinearity parameter obeys the relation

$$\alpha = \frac{U_0}{T}\frac{j}{j_c},$$

and the superconductor response at small current densities j is always quasi-linear (diffusion). On the contrary, in the vortex-glass regime, the superconductor response to current perturbations with

$$\alpha = \mu\frac{U(j)}{T}$$

(where μ is a constant factor) exhibits power nonlinearity of the $|\nabla b|^\sigma$ type and the equation order increases by unity (see Eq. (10) below).

If the system obeys the relations $v_0 = Av_c$ and $(\partial U/\partial j)|_0 = U_0/j_c$, where A is the coefficient on the order of unity and v_c is the critical velocity, then [1]

$$\rho = 2A\rho_{\text{flow}}(B)\frac{U_0}{T}e^{-U_0/T}, \quad (1)$$

where

$$\rho_{\text{flow}}(B) = \rho_n B/H_{c2}$$

is the flux-flow resistivity, H_{c2} is the second (upper) critical field, and ρ_n is the normal-state resistivity.

Using the Maxwell equation

$$-\frac{1}{c}\frac{\partial B}{\partial t} = \frac{\partial E}{\partial x},$$

the Ohm law $E = \rho j$, and relation (1), we obtain the equation

$$\frac{\partial B}{\partial t} = \frac{c^2}{4\pi}\nabla(\rho(B)\nabla B).$$

By passing to a dimensionless coordinate $x \longrightarrow x/\lambda$ and time $\tau = t/t_0$, this equation can be represented in a dimensionless form

$$\frac{\nabla b}{\partial \tau} = D\nabla(\rho(b)\nabla b), \quad (2)$$

where

$$D = \frac{H_{c1}}{H_{c2}}c^2\rho_n\frac{t_0}{\lambda^2}$$

is the diffusion coefficient, λ is the London penetration depth, c is the velocity of light, and $\rho(b) = 2\sigma e^{-\sigma}b$ (by virtue of relation (1)).

Let us consider Eq. (2) with the following boundary condition:

$$b(0, \tau) = b_0(1-\tau)^{-1}, \quad \tau < 1, \quad b_0 = \text{const} > 0. \quad (3)$$

The boundary-value problem posed by Eqs. (2) and (3) has a solution in separable variables [2]

$$b_s(x, \tau) = b_0(1-\tau)^{-1}(1-x/x_s)^2, \quad 0 < x \le x_s, \quad (4)$$

where

$$x_s = (6Db_0)^{1/2} \quad (D \propto \sigma). \quad (5)$$

For $x > x_s$, the function $b_s(x, \tau)$ is zero (Fig. 3). According to the solution given by expressions (4) and (5), the magnetic field is localized despite its infinite growth for $\tau \longrightarrow 1^-$ (limit on the left).

Blatter *et al.* [1] considered Eq. (2) with a constant diffusion coefficient in the vicinity of a point with $b \gg 1$. In this case, this equation simplifies to

$$\frac{\partial b}{\partial \tau} = D\Delta b. \quad (6)$$

For certainty, let us solve this equation with the boundary condition

$$b(0, \tau) = b_0 \exp R_0(1-\tau)^{-1}, \quad R_0 = \text{const} > 0 \quad (7)$$

and the initial condition

$$b_0(x) = \text{const}. \quad (8)$$

The boundary condition (7) is selected in the exponential form only in order to obtain an analytical solution (see [2]), which is possible in the case of a constant diffusion coefficient. For the general form of Eq. (2), it is possible to construct self-similar solutions in the half-space $\{x > 0\}$ with the boundary regime at $x = 0$ set as

$$B(0, \tau) = b_1(\tau), \quad \tau > 0,$$

where $b_1(\tau)$ exhibits infinite growth with increasing τ.

For example, in the case of $b_1(\tau) = b_0(1 + \tau)^m$ ($m > 0$), the solution takes the form

$$b_A(x, \tau) = b_0(1+\tau)^m f_A(\zeta), \ \zeta = x/(1+\tau)^{(1+m\sigma)/(\sigma+2)}.$$

For $b_1(\tau) = b_0 e^{\tau}$, the solution is

$$b_A(x, \tau) = b_0 e^{\tau} f_A(\zeta), \ \zeta = x/\exp\left\{\frac{\sigma}{(\sigma+2)}\tau\right\}.$$

These self-similar solutions are asymptotically stable.

The initial- and boundary-value problem (6)–(8) has an analytical solution (see [2, p. 132]) depicted in Fig. 1. Similar to the case illustrated in Fig. 2, the energy is virtually completely localized within a finite region $x < x_s$, where $x_s = 2(DR_0)^{1/2}$. For $x_1 > x_s$, the energy is

$$W(x_1, t) = \int_{x_1}^{\infty} b(\zeta, t)d\zeta < \text{const}, \quad t \in (0, t_0).$$

It should be noted that the effective depth of localization in this case is independent of the amplitude b_0. With allowance for the field dependence $\rho(b)$, this statement is not valid.

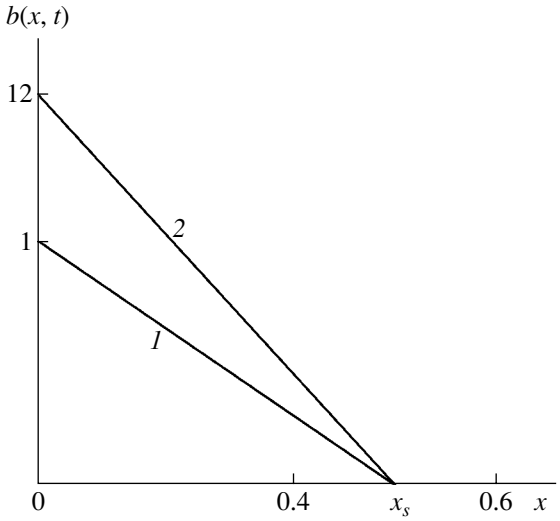

Fig. 3. Magnetic wave front stopping in a superconductor for $D = 0.354$, $\sigma = 2$, $b_0 = 1$, $x_s = 0.5$, and $t_0 - t = 1.25 \times 10^{-2}$ (*1*) and 9×10^{-4} (*2*).

Thus, in the range of fields different from $H_{c2}(T)$, where the superconductor occurs in a vortex-liquid state, the magnetic field exhibits strict localization (in terms of [2]). In the vicinity of $H_{c2}(T)$, only an effective localization takes place. This behavior is related to the fact that, as the melting curve $B_m(T)$ approaches the $H_{c2}(T)$ curve, the system exhibits a crossover whereby the order parameter sharply increases and fluctuations near $H_{c2}(T)$ become significant (see the diagram for the vortex-liquid phase in Fig. 2, which is taken from [1]).

Vortex-glass model. In the vortex-glass regime at temperatures T close to the melting curve $T_m(B)$, the superconductor response becomes substantially nonlinear because the parameter α exhibits infinite growth ($\alpha \longrightarrow \infty$) as $j \longrightarrow 0$. In this case, we must pass from Eq. (2) to the continuity equation [1]

$$\frac{\partial B}{\partial t} = -\frac{\partial}{\partial x}[vB]. \quad (9)$$

It can be shown (see [1, p. 1351]) that, if the activation barrier has the form

$$U(j) = U_0 \ln\left(\frac{j_c}{j}\right),$$

and the vortex velocity can be represented as

$$v = v_0 \exp[-U(j)/T] = v_0 J|J|^{\sigma} \ (J = j/j_c),$$

in the vicinity of a certain equilibrium field $B = B_0$ (in our case, $B = B_{c1}$), the equation of continuity (9) of the vortex line can be reduced to

$$\frac{\partial b}{\partial t} = \nabla(\nabla b|\nabla b|^{\sigma}). \quad (10)$$

Here, $\sigma = U_0/T$, the dimensionless variables are substituted as $x \longrightarrow x/d_p$ and $t \longrightarrow tv_0/d_p$, $d_p = cB_0/4\pi j_c$, and j_c is the critical current (for $d_p/v_0 = t_0$, this corresponds to the preceding case with $t \longrightarrow \tau$).

The above expression for the vortex velocity is selected so as to provide for the crossover at high temperatures ($\sigma \longrightarrow 0$) to the regime of viscous vortex motion ($v \propto J$). Therefore, Eq. (10) describes only magnetic field perturbations on the background of an equilibrium B_0 value. However, within the framework of the theory of weak collective pinning (see, e.g., [4, 5]), this model agrees with experimental data.

It was demonstrated (see [1, Fig. 6]) that the finite thermoactivation barrier against the vortex motion in the vicinity of the melting curve $B_m(T)$ is sufficiently high ($T \ll U_0 < \infty$) and the vortex liquid is pinned (thermally assisted flux flow regime). Near the upper critical field $H_{c2}(T)$, the barrier is small ($U_0 \ll T$) and the vortex liquid cannot be pinned (flux flow regime). As will be demonstrated below, the parameter $\sigma = U_0/T$ determines the magnetic flux penetration depth into the half-space in the blow-up regime. The case of $\sigma \gg 1$ for a finite sample was considered in [1].

Equation (10) describes processes involving magnetic-field perturbations spreading at a finite velocity over any constant background field. In particular, the function $b(x, t) = b_A(x, t)$ is a solution featuring a finite front on a homogeneous (zero-level) background.

Let us solve Eq. (10) with the boundary condition

$$b(0, t) = b_0(1-t)^m, \quad 0 < t < 1, \quad m < 0.$$

The corresponding self-similar solution is

$$b_A(x, t) = b_0(1-t)^m \theta_A(\zeta), \quad (11)$$

where

$$\zeta = \frac{x}{(1-t)^{(1+m\sigma)/(\sigma+2)}}$$

and $\theta_A \geq 0$ is the generalized solution to the boundary-value problem

$$b_0^{\sigma}(|\theta_A'|^{\sigma}\theta_A') - \frac{2+m\sigma}{\sigma+2}\theta_A'\zeta + m\theta_A = 0, \quad \zeta > 0 \quad (12)$$

with the boundary condition

$$\theta_A(0) = 1, \quad \theta_A(\infty) = 0.$$

In the case of $m = -1/\sigma$, Eq. (12) is readily integrated to yield the self-similar solution

$$b_A(x, t) = b_0(1-t)^{-1/\sigma}[(1 - x/x_0)_+]^{(\sigma+2)/\sigma},$$

where

$$x_0 = \frac{\sigma+2}{\sigma}\left[\frac{2\sigma(\sigma+1)}{(\sigma+2)}\right]^{1/(\sigma+2)} b_0^{\sigma/(\sigma+2)} \quad (13)$$

is a magnetic wave with an immobile point at the front localized within $0 < x < x_0$ during the entire lifetime of the blow-up boundary regime, $(\kappa)_+ = (\kappa$ for $\kappa \geq 0$; 0 for $\kappa < 0\}$, and 1^- denotes the exact upper limit on the left. At $x > x_0$, the magnetic perturbations do not escape from the localization region and the homogeneous magnetic background remains unchanged (Fig. 3).

An analysis of the spatiotemporal structure of the self-similar solution (11) shows that the blow-up regime is not localized for $m < -1/\sigma$ [2], that is,

$$x_f(t) \sim (1-t)^{(1+m\sigma)/(\sigma+2)} \longrightarrow \infty$$

for $t \longrightarrow 1^-$, where x_f is the coordinate of the magnetic wave front.

It should be noted that an analogous result can be obtained in the case of a power boundary regime ($m > 0$). For $m = 0$, this expression reduces to a formula for the wave front coordinate in a plate $b(x_f, t) = 0$ (see [1]):

$$x_f(t) = (1+t)^{1/\sigma}, \quad \sigma \gg 1.$$

An analogous formula for a half-space can be derived using the method described in [2]:

$$\bar{x}_f = (1+t)^{1/(\sigma+2)}, \quad t \longrightarrow t/t_0, \quad \sigma > 0.$$

Thus, the magnetic flux exhibits localization for $m \in (-1/\sigma, 0)$, whereby the field grows to infinity only at the point $x = 0$ (see [2, p. 92]).

For a vortex-glass phase in the blow-up regime, the magnetic flux penetrates in the half-space to a finite depth. This depth depends on the temperature and the thermoactivation barrier via the parameter σ as described by formula (13).

An analogous formula for the vortex-liquid regime can be written as

$$x_s = [2Db_0 e^{-\sigma}\sigma]^{1/2}. \quad (14)$$

As can be seen, the magnetic field virtually does not penetrate into the superconductor if the activation barrier is small ($\sigma \longrightarrow 0$).

For the model of a vortex-glass phase at any finite temperature, it is necessary to determine the limit in relation (13) for $\sigma \longrightarrow \infty$. This yields

$$x_0 = [2\sigma]^{1/(\sigma+2)} + O(\sigma^{-1}). \quad (15)$$

An analysis of relations (14) and (15) leads to the following conclusions. For $\sigma \longrightarrow \infty$, the magnetic flux penetration depth $x_s(\sigma) \longrightarrow 0$ in the vortex-liquid model and $x_s(\sigma) \longrightarrow 1$ in the vortex-glass model. On the other hand, for $\sigma \longrightarrow 0$, we obtain the asymptotic formulas $x_s = [2Db_0\sigma]^{1/2}$ in the vortex-liquid model and $x_s = 2\sigma^{1/2}$ in the vortex-glass model. Under identical boundary conditions, we should set $D = b_0 = 1$. Then, the asymptotic formulas coincide to within a factor of $\sqrt{2}$, which has a simple physical explanation.

Thus, the difference in the superconductor response to an external (boundary) perturbation (at small current perturbations, $j_c - j \ll j_c$ [1]) for the vortex-liquid and vortex-glass phases takes place only in the case of sufficiently large finite values of the nonlinearity parameter ($\sigma > 0$).

REFERENCES

1. G. Blatter, M. V. Feigel'man, V. B. Geshkenbein, *et al.*, Rev. Mod. Phys. **66**, 1125 (1994).
2. A. Samarskii, V. Galaktionov, V. Kurdyumov, and A. Mikhailov, *Blow-up in Quasilinear Parabolic Equations* (Nauka, Moscow, 1987; Walter de Gruyter, Berlin, 1995).
3. V. R. Romanovskiĭ, Zh. Tekh. Fiz. **70** (12), 47 (2000) [Tech. Phys. **45**, 1557 (2000)].
4. P. J. Kung, M. P. Maley, M. E. McHenry, *et al.*, Phys. Rev. B **48**, 13922 (1993).
5. E. Zeldov, N. M. Amer, G. Koren, *et al.*, Phys. Rev. Lett. **62**, 3093 (1989).

Translated by P. Pozdeev

Technical Physics Letters, Vol. 31, No. 5, 2005, pp. 428–431. Translated from Pis'ma v Zhurnal Tekhnicheskoĭ Fiziki, Vol. 31, No. 10, 2005, pp. 51–56.

An Acoustic Study of the Relaxation Properties of ZhK-1282 Nematic Liquid Crystals in the Vicinity of the Nematic–Isotropic Phase Transition

V. V. Surnychev, D. L. Bogdanov, and V. V. Belyaev

Moscow State Regional University, Moscow oblast, Russia

e-mail: conrad@nm.ru

Received November 10, 2004

Abstract—The viscous and elastic properties of a ZhK-1282 nematic liquid crystal (NLC) were studied in a temperature interval from 290 to 360 K by method of ultrasonic spectroscopy in the 3–63 MHz frequency range. The temperature dependences of the NLC density and shear viscosity are presented. The results of measurements of the velocity and attenuation of ultrasound and the shear viscosity were used to calculate the volume viscosity coefficient, the moduli of dilatation and isothermal compressibility, the relaxation times of the elastic and viscous properties, and the corresponding critical characteristics of the given NLC. © *2005 Pleiades Publishing, Inc.*

The method of ultrasonic spectroscopy is based on the measurement of the temperature and frequency dependences of the velocity and attenuation of ultrasound in a given material. In combination with data on the density, heat capacity, and viscosity, this acoustical method provides a large body of information not only about thermodynamic and relaxation properties, but also about the structure, thermal processes, and the character and intensity of molecular interactions in this material [1–6].

We have studied a nematic liquid crystal (NLC) of the ZhK-1282 type (created at the Research Institute of Organic Intermediates and Dyes, Moscow) comprising a mixture of alkoxycyanobiphenyls C_nH_{2n+1}–O–C_6H_4–C_6H_4–CN (n = 3–8) (80%), Demus' ester C_4H_9–C_6H_{10}–COO–C_6H_4–OC_2H_5 (16%), and Gray's ester C_4H_9–C_6H_6–COO–C_6H_4–OC_2H_5 (4%). The temperature interval for the existence of a nematic mesophase of this substance at atmospheric pressure extends from 253.1 to T_C = 335.1 K (T_C is the clarification temperature). This mixture is characterized by the presence of both strongly and weakly polar components with various types of intermolecular interactions.

The temperature dependences of the velocity and attenuation of ultrasound in ZhK-1282 in the interval from 290 to 360 K were determined using the variable-distance pulsed phase technique. The plots of the ultrasound velocity c and the absorption coefficient (Stokes attenuation constant) α/f^2 versus temperature at various frequencies in the range from 3 to 63 MHz are presented in Figs. 1a and 1b, respectively.

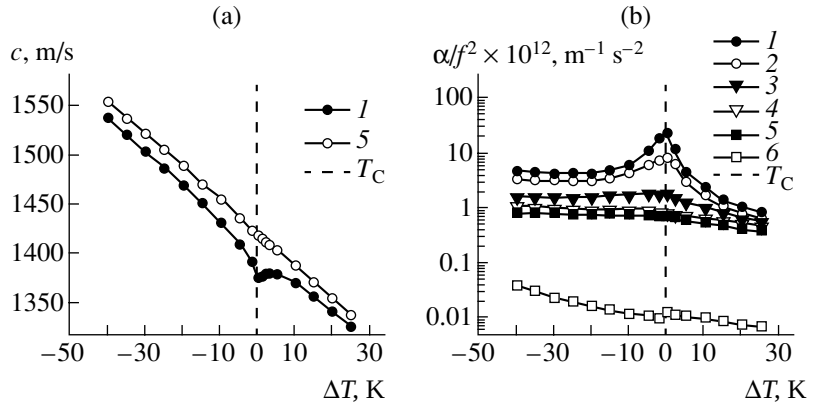

Fig. 1. The temperature dependence of (a) the ultrasound velocity and (b) the ultrasound attenuation coefficient at various frequencies (MHz): (*1*) 3; (*2*) 9; (*3*) 27; (*4*) 45; (*5*) 63; (*6*) $(\alpha/f^2)_S$. T_C is the clarification temperature; $\Delta T = T - T_C$.

1063-7850/05/3105-0428$26.00 © 2005 Pleiades Publishing, Inc.

Table 1. Relaxation parameters of ZhK-1282 at temperatures around T_C

ΔT, K	c_0, m/s	c_∞, m/s	f_c, MHz	$A \times 10^{12}$, $m^{-1} s^2$	$B \times 10^{12}$, $m^{-1} s^2$	f_a, MHz
−40	1537	1555	17	4.0	0.58	17
−10	1432	1457	14	6.1	0.47	14
−5	1408	1438	10	11.8	0.46	10
−2	1383	1426	5.9	24.5	0.46	6.4
2	1376	1413	7.5	15.5	0.44	7.5
5	1381	1406	13	4.4	0.44	13
10	1371	1392	21	2.1	0.35	21
20	1344	1364	42	0.82	0.19	42

The frequency dependences of the velocity and attenuation of ultrasound are described by the formulas [7]

$$c^2 = c_0^2 + (c_\infty^2 - c_0^2)\frac{(f/f_c)^2}{1 + (f/f_c)^2}, \quad (1)$$

$$\frac{\alpha}{f^2} = \frac{A}{1 + f^2/f_\alpha^2} + B, \quad (2)$$

where c_∞ and c_0 are the high- and low-frequency ultrasound velocity limits, respectively; f_c and f_α are the corresponding relaxation frequencies;

$$A = \frac{2\pi^2}{\rho c_0^3}\eta_V^{(0)}, \quad (3)$$

$$\eta_V^{(0)} = (c_\infty^2 - c_0^2)\rho\tau_\alpha, \quad (4)$$

ρ is the density; $\eta_V^{(0)}$ is the low-frequency limit of the volume viscosity; and $\tau_\alpha = 1/(2\pi f_\alpha)$.

An analysis of the frequency dependences of the ultrasound velocity and the absorption coefficient in terms of relations (1) and (2) allows the parameters characterizing relaxation processes in the vicinity of the nematic–isotropic phase transition (Table 1) to be calculated using the results of experimental measurements. As can be seen from the results presented in Table 1, the characteristic relaxation frequencies f_c and f_α are virtually the same in the entire temperature range studied.

Using the values of c_∞ and c_0 determined from the analysis of the frequency dependence of the ultrasound velocity, it is possible to calculate the absolute dispersion of the sound velocity, $(c_\infty^2 - c_0^2)_c$, as well as the dispersions of the elastic modulus ($\Delta K_S^{(c)}$) and the adiabatic compressibility ($\Delta\beta_S^{(c)}$):

$$\Delta K_S^{(c)} = \rho(c_\infty^2 - c_0^2)_c, \quad (5)$$

$$\Delta\beta_S^{(c)} = 1/\Delta K_S^{(c)}. \quad (6)$$

Using relations (3) and (4), we obtain an expression for the ultrasound velocity dispersion related to the relaxation of the volume viscosity:

$$(c_\infty^2 - c_0^2)_\alpha = \frac{Ac_0^3}{2\pi^2\tau_\alpha}. \quad (7)$$

The corresponding dispersions of the elastic modulus and the adiabatic compressibility are as follows:

$$\Delta K_S^{(\alpha)} = \rho(c_\infty^2 - c_0^2)_\alpha, \quad (8)$$

$$\Delta\beta_S^{(\alpha)} = 1/\Delta K_S^{(\alpha)}. \quad (9)$$

Using the experimental values of the ultrasound velocity measured at 3 MHz (c_3) and 63 MHz (c_{63}), we may calculate the absolute values of the elastic moduli $K_S^{(3)}$ and $K_S^{(63)}$, the adiabatic compressibility $\beta_S^{(3)}$ and $\beta_S^{(63)}$, and the corresponding dispersions $\Delta K_S^{(ex)}$ and $\Delta\beta_S^{(ex)}$:

$$K_S^{(3)} = \rho c_3^2, \quad K_S^{(63)} = \rho c_{63}^2, \quad \Delta K_S^{(ex)} = \rho(c_{63}^2 - c_3^2), \quad (10)$$

$$\beta_S^{(3)} = \rho/K_S^{(3)}, \quad \beta_S^{(63)} = 1/K_S^{(63)}, \quad \beta_S^{(ex)} = 1/\Delta K_S^{(ex)}. \quad (11)$$

The results of analysis of the frequency dependence of the relaxation characteristics as functions of the parameters of state show that relaxation processes in

Table 2. Shear viscosity (η_S), density (ρ), volume viscosity coefficient ($\eta_V^{(0)}$ calculated using formula (3)), and $\eta_V^{(0)}/\eta_S$ ratio for ZhK-1282 at temperatures around T_C

ΔT, K	ρ, kg/m^3	$\eta_S \times 10^3$, Pa s	$\eta_V^{(0)} \times 10^3$, Pa s	$\eta_V^{(0)}/\eta_S$
−40	1035	5.60	761	136
−15	1014	1.64	694	422
−10	1010	1.37	920	672
−5	1006	1.15	1693	1471
−2	1003	1.04	3396	3269
2	998	1.20	2082	1734
5	996	1.12	587	525
10	992	0.98	272	278
25	983	0.65	74	113

Table 3. Parameters of the temperature dependence of the low-frequency relaxation of elastic and viscous properties of ZhK-1282

Phase	τ_c^0, s	β_c	τ_α^0, s	β_α
Nematic	2.4	0.45	2.4	0.45
Isotropic	0.48	0.76	0.48	0.76

the liquid crystal studied proceed via two mechanisms: (i) the "critical" mechanisms related to relaxation and fluctuations of the orientation order parameter, and (ii) the "normal" mechanism related to the structural relaxation. Far from the transition, the normal relaxation mechanism is predominant, while near the clarification temperature T_C the critical mechanism begins to dominate. The critical low-frequency relaxation process in both phases is manifested in a narrow temperature interval. The temperature dependence of the effective low-frequency relaxation time for the viscous and elastic properties is described by the expressions,

$$\tau_\alpha = \tau_\alpha^0\left(\frac{\Delta T}{T_C}\right)^{-\beta_\alpha}, \quad \tau_c = \tau_c^0\left(\frac{\Delta T}{T_C}\right)^{-\beta_c}, \qquad (12)$$

where β_α and β_c are the critical exponents; τ_α^0 and τ_c^0 are the dimensional coefficients; and $\Delta T = T - T_C$. It should be noted that the parameters β_α, β_c, τ_α^0 and τ_c^0 are independent of the temperature.

An analysis of the temperature dependences of the characteristic times $\tau_c = 1/(2\pi f_c)$ and $\tau_\alpha = 1/(2\pi f_\alpha)$ showed that, in the vicinity of the clarification point, these parameters are satisfactorily described by formulas (12). The values of τ_c^0, τ_α^0, β_c, and β_α for the isotropic and nematic phases of ZhK -1282 are presented in Table 3. As can be seen from these data, the critical characteristics determined from the temperature dependence of the relaxation rate of the ultrasound velocity coincide with those determined from analogous data on the attenuation coefficient.

Using the values of dispersion of the ultrasound velocity, it is possible to calculate the elastic moduli (K_S), the adiabatic compressibility (β_S), and the dispersions of these quantities (ΔK_S and $\Delta\beta_S$). The results of such calculations are summarized in Table 4. As can be seen, the values of ($\Delta K_S^{(c)}$ and $\Delta K_S^{(\alpha)}$) are quite close: they virtually coincide near T_C and somewhat differ far from the clarification point.

The results presented above lead to the conclusion that processes involved in the relaxation of both the vis-

Table 4. Elastic moduli ($K_S \times 10^9$, N/m^2)), the adiabatic compressibility ($\beta_S \times 10^{-10}$, m^2/N), and the dispersions of these quantities ($\Delta K_S \times 10^7$, N/m^2; $\Delta\beta_S \times 10^{-8}$, m^2/N) for ZhK-1282 at temperatures around T_C

ΔT, K	$K_S^{(3)}$	$K_S^{(63)}$	$\beta_S^{(3)}$	$\beta_S^{(63)}$	$\Delta K_S^{(c)}$	$\Delta K_S^{(\alpha)}$	$\Delta K_S^{(ex)}$	$\Delta\beta_S^{(c)}$	$\Delta\beta_S^{(\alpha)}$	$\Delta\beta_S^{(ex)}$
−40	2.45	2.49	4.08	4.01	5.92	8.12	4.27	1.69	1.23	2.34
−15	2.14	2.19	4.68	4.56	6.67	7.41	5.36	1.50	1.35	1.86
−10	2.07	2.14	4.82	4.68	7.15	8.09	6.36	1.40	1.24	1.57
−5	2.00	2.08	4.99	4.81	8.73	10.6	7.42	1.15	0.94	1.35
−2	1.95	2.04	5.13	4.90	12.1	13.7	9.00	0.83	0.73	1.11
2	1.91	1.99	5.24	5.03	10.3	9.81	7.89	0.97	1.02	1.27
5	1.90	1.96	5.25	5.09	7.08	4.79	6.16	1.41	2.09	1.62
10	1.87	1.92	5.35	5.22	5.76	3.59	4.67	1.74	2.79	2.14
25	1.74	1.76	5.76	5.67	5.00	2.26	2.65	2.00	4.42	3.77

cosity coefficients and the elastic moduli in the vicinity of the clarification temperature are controlled by the same mechanism: relaxation of heterophase fluctuations.

REFERENCES

1. M. F. Grebenkin and A. V. Ivashchenko, *Liquid Crystal Materials* (Khimiya, Moscow, 1987) [in Russian].
2. M. V. Verveĭko and V. N. Verveĭko, *Ultrasound and Thermodynamic Properties of Materials* (Kursk. Gos. Univ., Kursk, 2002), pp. 41–54 [in Russian].
3. M. V. Mikhaĭlov, V. A. Solov'ev, and Yu. S. Syrnikov, *Fundamentals of Molecular Acoustics* (Nauka, Moscow, 1964) [in Russian].
4. P. K. Khabibulaev, É. V. Gevorkyan, and A. S. Lagunov, *Rheology of Liquid Crystals* (FAN, Tashkent, 1992) [in Russian].
5. A. P. Kapustin and O. A. Kapustina, *Liquid Crystal Acoustics* (Nauka, Moscow, 1986) [in Russian].
6. V. V. Belyaev, *Viscosity of Nematic Liquid Crystals* (Nauka, Moscow, 2002; Cambridge International Science Publishing, 2004).
7. *Physical Acoustics: Principles and Methods*, Ed. by W. P. Mason (Academic Press, New York, 1968), Vol. 2, Part A.

Translated by P. Pozdeev

Technical Physics Letters, Vol. 31, No. 5, 2005, pp. 432–434. Translated from Pis'ma v Zhurnal Tekhnicheskoĭ Fiziki, Vol. 31, No. 10, 2005, pp. 57–63.

Periodic and Chaotic Regimes of Liquid Dielectric Convection in a Horizontal Capacitor

V. A. Il'in and B. L. Smorodin*

Perm State University, Perm, Russia

** e-mail: smorodin@psu.ru*

Received December 3, 2004

Abstract—Electroconvective oscillations in nonuniformly heated dielectric liquid occurring in an alternating electric field between plates of a horizontal plane capacitor have been studied within the framework of a low-mode model. The general case of arbitrary frequencies and amplitudes of the electric field is considered and nonlinear dynamics of the convective structures arising as a result of the parametric instability is determined. Two classes of synchronous electroconvective oscillations in the system are found, and the competition and hysteresis of these regimes are analyzed. The average heat flux via the plane capacitor in one of these regimes is greater by a factor of 2.5 than the heat flux in the other regime. The transition to chaotic oscillations proceeds either via a quasi-periodic regime or directly from equilibrium. The boundaries of domains corresponding to various types of behavior of the dielectric liquid are determined in the space of parameters. © *2005 Pleiades Publishing, Inc.*

Inhomogeneous heating of dielectric liquids in electric field may result in the onset of convective motions [1]. As is known, the Rayleigh–Benard convection does not arise under zero gravity conditions or in the case of heating from above. In such cases, the instability of dielectric liquids may be caused by other factors, such as dielectrophoretic forces related to the inhomogeneous polarization of the medium [2]. The effect of electric fields on the motion of liquids is used for the direct conversion of electric energy into kinetic energy of a liquid flow (in electrohydrodynamic energy converters). Another possible application is related to the possibility of controlling heat transfer in high-voltage devices.

The intensity of convection and heat transfer is significantly influenced by modulated thermal and magnetic fields of arbitrary amplitudes and frequencies [3, 4]. Another method of dynamic action upon convective motions in dielectric liquids is based on the use of an alternating electric field of a finite frequency for the resonance excitation of electroconvective motions in the medium [5]. Investigations into this phenomenon are important for the development of various technologies and devices employing electric fields.

This study is devoted to nonlinear oscillatory regimes of electroconvection in the ideal liquid dielectric medium occurring in an alternating electric field between plates of a horizontal plane capacitor of thickness h, the boundary planes of which are heated to different temperatures: $T(-h/2) = \Theta$, $T(h/2) = 0$. The upper boundary potential is assumed to be zero, while the lower boundary potential varies with time according to the law $\varphi(-h/2) = U\cos(2\pi\bar{\nu}t)$, where U is the voltage amplitude, $\bar{\nu} = 1/t_f$ is the frequency, and t_f is the period of modulation. The permittivity ε of the dielectric liquid is assumed to be a linear function of the temperature, $\varepsilon = \varepsilon_0(1 - \beta_\varepsilon T)$, where β_ε is a positive coefficient.

In the case that the voltage applied to the capacitor does not exceed a certain critical value, we may ignore the effect of charge injection on the motion of the medium [6] and write the system of equations for the convection in a liquid dielectric occurring in the gravitational and electric fields with the corresponding boundary conditions (in a dimensionless form):

$$\frac{\partial \mathbf{v}}{\partial t} + \frac{1}{P}(\mathbf{v}\nabla)\mathbf{v} = -\nabla p + \nabla^2\mathbf{v} + \mathrm{Ra}T\mathbf{e} - \frac{R'_\varepsilon}{2}E^2\nabla\varepsilon,$$

$$P\frac{\partial T}{\partial t} + (\mathbf{v}\nabla)T = \nabla^2 T, \quad \mathrm{div}\mathbf{v} = 0, \quad \mathrm{div}\varepsilon\mathbf{E} = 0, \quad (1)$$

$$\mathbf{E} = -\nabla\varphi, \quad \mathbf{e} = (0, 0, 1), \quad \varepsilon = 1 - S_\varepsilon T.$$

Here p, $\mathbf{v}$, φ, and T are the pressure, velocity, potential, and temperature fields; $\mathbf{E}$ is the electric field strength; $\mathrm{Ra} = g\beta\Theta h^3\rho/\eta\chi$ is the Rayleigh number ($\mathrm{Ra} < 0$ corresponds to the case of heating from above); $R'_\varepsilon = \varepsilon_0 U^2/\eta\chi$ is a dielectrophoretic analog of the Galileo number; $P = \eta/\chi\rho$ is the Prandtl number; $\nu = \rho\bar{\nu}h^2/\eta$ is the dimensionless modulation frequency; $S_\varepsilon = \beta_\varepsilon\Theta$ is a parameter characterizing inhomogeneity of the permittivity; ρ, η, χ, and β are the density, viscosity, thermal diffusivity, and thermal expansion coefficient of the liquid, respectively; and g is the acceleration of gravity. Assuming a weak temperature dependence of the per-

mittivity ($\beta_\varepsilon \sim 10^{-2}$–$10^{-4}$ K^{-1}), we may ignore spatial inhomogeneity of the electric field in the equation of motion [1]. The state of quasi-equilibrium is characterized by the following conditions: $\mathbf{v}_0 = 0$, $T_0 = 1/2 - z$, $\varphi_0 = (1/2 - z)\cos(\omega t)$, and $E_0 = \cos(\omega t)$.

Excluding the electric field from Eqs. (1) and restricting consideration to two-dimensional motions, we can write the current function ψ and the temperature deviation ϑ from the equilibrium value T_0 as

$$\begin{aligned} \psi &= A\sin k\pi x\cos\pi z, \\ \vartheta &= B\cos k\pi x\cos\pi z + C\sin 2\pi z. \end{aligned} \tag{2}$$

The amplitudes of these modes ($X \sim A$, $Y \sim B$, $Z \sim C$) are described by a set of equations analogous to the Lorentz differential equations [7] with variable coefficients:

$$\begin{aligned} \dot{X} &= -\mathrm{Pr}X + (r + e\cos^2 2\pi\nu t)Y, \\ \dot{Y} &= -Y + X - XZ, \\ \dot{Z} &= -bZ + XY, \quad b = \frac{4}{1+k^2}, \quad r = \frac{\mathrm{Ra}}{\mathrm{Ra}_0}, \quad e = \frac{\mathrm{Ra}_\varepsilon}{\mathrm{Ra}_{\varepsilon 0}}, \end{aligned} \tag{3}$$

$$\mathrm{Ra}_\varepsilon = R'_\varepsilon S_\varepsilon^2, \quad \mathrm{Ra}_0 = \frac{\pi^4(1+k^2)^3}{k^2}, \quad \mathrm{Ra}_{\varepsilon 0} = \frac{\pi^4(1+k^2)^4}{k^4},$$

where r and e are the normalized thermal and electric Rayleigh numbers, respectively; b is a geometric parameter; and Ra_0 and $\mathrm{Ra}_{\varepsilon 0}$ are the critical numbers corresponding to the onset of thermogravitational [8] and dielectrophoretic [9] convection, respectively.

The boundaries of the resonance domains of dielectrophoretic convection in the case of heating from above were determined previously [10]. It was established that subharmonic perturbations are absent, while the synchronous perturbations can be subdivided into two classes, $H1$ and $H2$. The synchronous perturbations belonging to these classes obey the following relations for a half-period shift:

$$\begin{aligned} &\psi \longrightarrow -\psi;\ \vartheta \longrightarrow -\vartheta;\ \varphi \longrightarrow \varphi\ (H1); \\ t \longrightarrow t + \pi/\omega;& \\ &\psi \longrightarrow \psi;\ \vartheta \longrightarrow \vartheta;\ \varphi \longrightarrow -\varphi\ (H2), \end{aligned} \tag{4}$$

where φ is the potential deviation from the equilibrium value φ_0.

Figure 1 shows a map of the regimes of electroconvection on the plane of parameters (e, t_f) (modulation amplitude versus period) for a dielectric liquid heated from above ($r = -10$) in the gravitational field. In domain I, all perturbations tend to decay and the dielectric liquid occurs in a state of mechanical equilibrium. In domain II, only periodic parametric oscillations are excited. Here, the current function ψ exhibits periodic variation with time in accordance with relations (4),

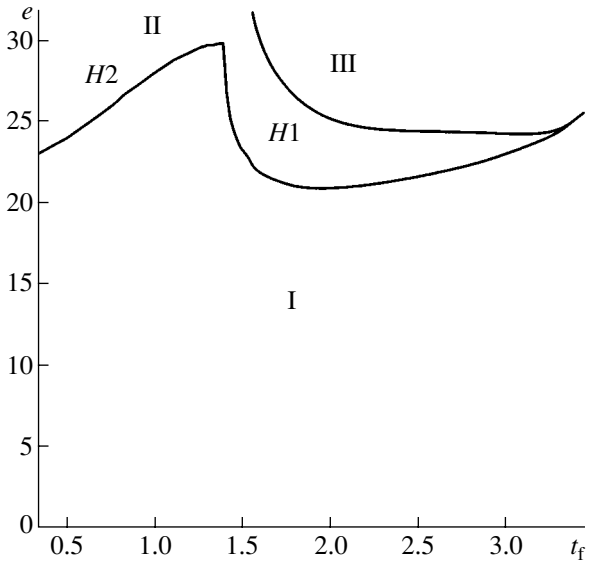

Fig. 1. A map of regimes on the plane of parameters t_f (modulation period) versus e (electrical Rayleigh number) for a dielectric liquid in a plane horizontal capacitor heated from above ($r = -10$): (I) equilibrium; (II) periodic oscillations; (III) chaotic regimes.

while deviations from the equilibrium temperature (ϑ) and potential (φ) caused by the nonlinear (with respect to the amplitudes X, Y, and Z) interaction differ from this behavior. As the amplitude increases (to approach the upper boundary of domain II in Fig. 1), incommensurate frequencies appear in the Fourier spectra characterizing the current function fluctuations for the external field periods $t_f < 3.3$, whereas chaotic oscillations take place near the lower boundary of domain III. Thus, the transition to chaos in this case proceeds via quasiperiodic regimes. For $t_f > 3.3$, the transition to chaos proceeds directly from equilibrium: chaotic oscillations exhibit damping below the boundary of domains I and III.

The intensity of heat transfer via liquid in the capacitor is conveniently characterized in terms of the Nusselt number (Nu), which represents the time-averaged dimensionless heat flux per unit area of the horizontal boundary. Calculations showed that Nu is close to unity for the perturbations of class $H1$, and it is greater by a factor of about 2.5 for the perturbations of class $H2$. Figure 2 presents a plot of the Nusselt number versus field amplitude e for the system driven by an external field with $t_f = 1.43$ (in the state at the boundary between regions $H1$ and $H2$). As can be seen from this figure, an increase in the field amplitude above the critical value of $e = 25.5$ leads to soft development of a convective regime of class $H1$, whereby the Nusselt number smoothly increases and slightly exceeds unity ($\mathrm{Nu}_{\max} = 1.08$). A sharp increase in the heat flux up to $\mathrm{Nu}_{\max} = 2.65$ in the interval $29.3 < e < 36.7$ is possible as a result of the transition to a regime of class $H2$, which proceeds in a rigid (jumplike) manner.

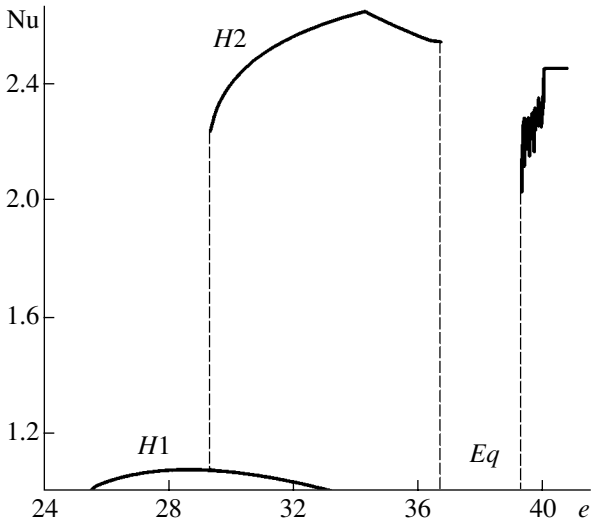

Fig. 2. A plot of the Nusselt number Nu (characterizing the heat flux via the horizontal capacitor) versus field amplitude e for $\nu = 0.7$ ($t_f = 1.43$).

In the region $29.3 < e < 33$ (Fig. 2), there is a competition between regimes of the classes $H1$ and $H2$. Depending on the initial state, the system exhibits oscillations of various types and features transitions with hysteresis between these regimes when the field amplitude is varied. Another type of competition—between the regimes of class $H2$ and equilibrium—is observed in the region $33 < e < 36.7$, and only equilibrium regimes (Eq) are possible for $36.7 < e < 39.3$. Indeed, a dielectric liquid heated from above ($r = -10$) in the absence of electric field occurs in a highly stable state and an alternating field may excite parametric instability only under resonance conditions characterized by certain amplitudes and frequencies. Escape from the resonance region is related to the damping of perturbations and the establishment of equilibrium, whereby an alternating field cannot excite electroconvection in the system.

As the field amplitude is increased further, $e > 39.3$, the system falls within the domain of chaotic oscillations. This region contains periodicity windows, the first of which corresponds to the interval of field amplitudes $40 < e < 40.8$ (Fig. 2).

Acknowledgments. This study was supported in part by the Russian Foundation for Basic Research (project no. 03-01-00327) and by the US Civilian Research and Development Foundation (CRDF Grant no. PE-009-0).

REFERENCES

1. R. J. Turnbull and J. R. Melcher, Phys. Fluids **12**, 1160 (1969).
2. L. D. Landau and E. M. Lifshitz, *Course of Theoretical Physics*, Vol. 8: *Electrodynamics of Continuous Media* (Nauka, Moscow, 1982; Pergamon Press, New York, 1984).
3. B. L. Smorodin, Zh. Éksp. Teor. Fiz. **120**, 1421 (2001) [JETP **93**, 1231 (2001)].
4. M. I. Shliomis, B. L. Smorodin, and S. Kamiyama, Philos. Mag. **83**, 2139 (2003).
5. B. L. Smorodin, Pis'ma Zh. Tekh. Fiz. **27** (24), 79 (2001) [Tech. Phys. Lett. **27**, 1062 (2001)].
6. S. A. Zhdanov, S. R. Kosvintsev, and I. Yu. Makarikhin, Zh. Éksp. Teor. Fiz. **117**, 398 (2000) [JETP **90**, 352 (2000)].
7. M. I. Rabinovich and D. I. Trubetskov, *Introduction to the Theory of Oscillations and Waves* (Nauka, Moscow, 1984; Kluwer, Dordrecht, 1989).
8. G. Z. Gershuni and E. M. Zhukhovitskiĭ, *Convective Stability of Incompressible Fluids* (Nauka, Moscow, 1972; Springfield, Jerusalem, 1976).
9. P. H. Roberts, Quart. J. Mech. Appl. Math. **22**, 211 (1969).
10. B. L. Smorodin and M. G. Velarde, J. Electrost. **50**, 205 (2001).

Translated by P. Pozdeev

Technical Physics Letters, Vol. 31, No. 5, 2005, pp. 435–437. Translated from Pis'ma v Zhurnal Tekhnicheskoĭ Fiziki, Vol. 31, No. 10, 2005, pp. 64–69.

Ion Separation with Respect to Charge in a Beam Transported via a Flat Gap

V. A. Shklyaev*, S. Ya. Belomyttsev, and V. V. Ryzhov

Institute of High-Current Electronics, Siberian Division, Russian Academy of Sciences, Tomsk, Russia

** e-mail: shklaev@to.hcei.tsc.ru*

Received December 29, 2004

Abstract—The transport of a beam of variously charged ions via a flat equipotential vacuum gap is theoretically described. The values of the critical beam current density are determined. The current density and the average ion charge in a beam past the gap are expressed as functions of the injected beam parameters (current density, average charge, and initial energy). Regimes featuring the effective separation of singly and doubly charged ions are found. © *2005 Pleiades Publishing, Inc.*

It was experimentally demonstrated [1–3] that the charge composition in a beam of variously charged ions changes upon transfer via an equipotential drift chamber. However, a complete theoretical description of this phenomenon is not available, which hinders its use for ion beam separation with respect to charge.

Let us consider a one-dimensional stationary problem for a multicomponent ion beam transported via a flat equipotential vacuum gap. By a multicomponent beam we imply a flow of variously charged ions possessing the same mass M. For the sake of simplicity, we restrict consideration to a beam consisting of singly and doubly charged ions. Let the ions have the same kinetic energies ε_0 in the region of hydrodynamic expansion [4], after which they enter an accelerating gap and are driven by the voltage U. Under real conditions, the gap is necessary in order to reflect electrons and extract a purely ion beam from a plasma [1–3]. Thus, in our case, the beam of accelerated ions is injected into the flat equipotential vacuum gap with the energies $eU + \varepsilon_0$ and $2eU + \varepsilon_0$ for the singly and doubly charged ions, respectively. In order to describe the transport of this beam via the gap, we use an approach based on the solution of the Poisson equation, which was developed previously and applied to a beam of singly charged ions moving in a flat gap [5, 6].

The Poisson equation describing the potential distribution in the gap transporting a nonrelativistic multicomponent beam can be written as

$$\frac{\partial^2\varphi}{\partial z^2} = -4\pi\left[j^{(1)} + j^{(2)}\left(\frac{\varphi}{2\varphi - \varepsilon_0/e}\right)^{1/2}\right]\sqrt{\frac{M}{2e}}\frac{1}{\varphi^{1/2}}, \quad (1)$$

where $j^{(1)}$ and $j^{(2)}$ are the partial current densities for the singly and doubly charged ions, respectively (in the region of reflection, the forward and reverse currents are added); φ is the electrostatic potential corresponding to the kinetic energy of singly charged ions; and $V^{(1)}/V^{(2)} = [\varphi/(2\varphi - \varepsilon_0/e)]^{1/2}$ is the ratio of velocities for the singly and doubly charged ions in the gap. In order to describe the charge composition of the beam, let us introduce the average ion charge defined in terms of the current density components of the singly and doubly charged ions: $K = (j^{(1)} + 2j^{(2)})/(j^{(1)} + j^{(2)})$.

Equation (1) was numerically integrated for the boundary conditions selected so as to ensure that a zero potential in the gap would correspond to the zero energy of singly charged ions. The result yields the critical current densities for the injected beam and gives the output current density j_{out} in the beam past the gap as a function of the injected current j_{in}. Since the beam consists of singly and doubly charged ions, we obtain four critical current densities (rather than two as in the case of a single-component beam). It is convenient to normalize the currents to the first critical current density for a beam of singly charged ions, $I = j/j_{cr1}$, where

$$j_{cr1} = \frac{1}{9\pi}\left(\frac{2eZ}{M}\right)^{1/2}\frac{(U + \varepsilon_0/e)^{3/2}}{(L/2)^2}. \quad (2)$$

For the convenient presentation of results, we also introduce the parameter

$$\alpha = \frac{\varepsilon_0/2}{eU + \varepsilon_0}. \quad (3)$$

Figure 1 shows an example of the dependence of the output current density on the injected current density (current transfer curve), which was obtained by numerical integration of the Poisson equation (1). In this plot, one can distinguish four states of the ion beam. The first is a single-flow state (0*b* segment in Fig. 1A), in which all ions in the beam are transported via the gap.

1063-7850/05/3105-0435$26.00 © 2005 Pleiades Publishing, Inc.

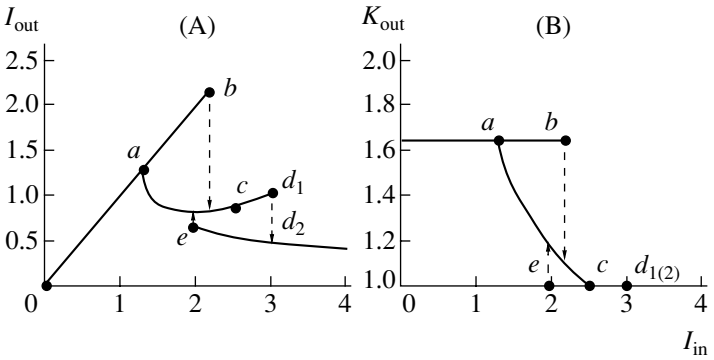

Fig. 1. The curves of (A) the output current density I_{out} and (B) the average ion charge K_{out} versus the injected current density I_{in} for a multicomponent ion beam transported via the gap for $K_{in} = 1.65$ and $\alpha = 0.119$ ($\varepsilon_0 = 47$ eV, $U = 150$ V).

When the injected current density exceeds the $I_{cr2}^{(2)}$ value (point *b*, representing the second critical current density for doubly charged ions), the system passes from the single-flow to a two-flow state, whereby a virtual anode (VA) is formed in the gap that reflects a fraction of the doubly charged ions back toward the plane of injection. The second state of the beam (curve *ac* in Fig. 1A) is characterized by the presence of a VA formed by the doubly charged ions. Singly charged ions in this state can freely travel via the gap. Since doubly charged ions are partly reflected from the VA, the average ion charge K_{out} in the beam past the gap decreases.

As the injected current density increases above the I_s value (point *c*, representing the separation current density), the VA formed by the doubly charged ions becomes the plane of their total reflection (reflective VA). Here, the beam passes to the third state (curve cd_1 in Fig. 1A), in which only the singly charged ions pass via the gap without reflection (the effective ion separation regime). The average ion charge past the gap in this state is $K_{out} = 1$ and the corresponding current density is $I_{out} = I_{in}^{(1)}$.

When the injected current density exceeds the $I_{cr2}^{(1)}$ value (point d_1, representing the second critical current density for singly charged ions), the system passes to the fourth state (curve ed_2 in Fig. 1A) with two virtual anodes at different positions in space. The first VA is the plane of reflection for doubly charged ions, while the second VA reflects a fraction of singly charged ions back toward the plane of injection. In this state, the average ion charge past the gap is $K_{out} = 1$ but the current density is $I_{out} = I_{in}^{(1)}$.

Depending on the parameters of the injected beam (the average ion charge K_{in}, the initial ion energy ε_0 before acceleration, and the accelerating voltage *U*), the relative current densities of the beam components may vary. The values of the second critical current densities for singly and doubly charged ions, as well as the ion separation current densities obtained upon numeric integration of Eq. (1), are listed in the table.

Based on the relation between the second critical current densities for singly and doubly charged ions ($I_{cr2}^{(1)}$ and $I_{cr2}^{(2)}$, respectively) and the ion separation current density (I_s), it is possible to determine three domains of parameters of the injected beam (Fig. 2) corresponding to various types of the current transfer curves. When the injected current density increases in the first domain (I), the beam sequentially passes all the four states described above. In the second domain (II), the beam passes from the first (single-flow) state via the VA formation to the third state featuring a reflective VA for doubly charged ions. In the third domain (III), the beam passes from the first directly to the fourth state with two VAs.

The second critical current densities ($I_{cr2}^{(1)}$ and $I_{cr2}^{(2)}$) and the ion separation current densities (I_s) for various parameters (K_{in} and α) of the injected ion beam

K_{in}		α				
		0.1	0.2	0.3	0.4	0.5
1.8	$I_{cr2}^{(2)}$	2.28	1.97	1.66	1.35	1.05
	I_s	3.7	3.83	3.7	3.41	3.01
	$I_{cr2}^{(1)}$	4.39	5.37	6.18	6.89	7.54
1.6		2.19	1.95	1.69	1.41	1.21
		2.29	2.35	2.24	2.05	1.79
		2.64	3.12	3.49	3.81	4.09
1.4		2.11	1.94	1.73	1.48	1.22
		1.81	1.89	1.80	1.64	1.42
		2.05	2.36	2.58	2.76	2.91
1.2		2.04	1.94	1.79	1.60	1.36
		1.71	1.76	1.69	1.54	1.34
		1.79	1.996	2.13	2.23	2.31

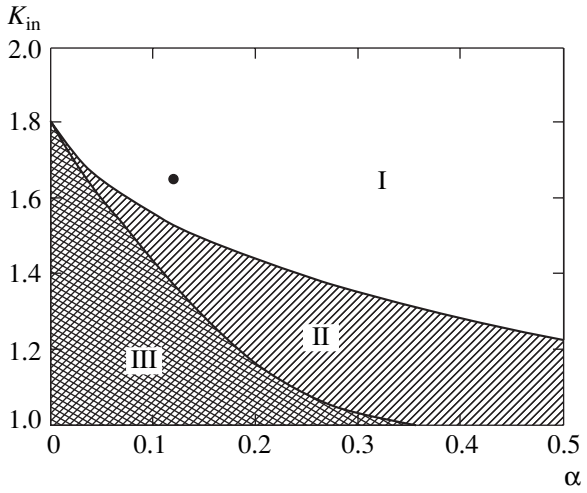

Fig. 2. The plane of parameters of the injected ion beam showing the domains I–III corresponding to various types of the current transfer curves. Point indicates the values of parameters K_{in} and α corresponding to the diagram in Fig. 1A.

Thus, the change in the average ion charge in a multicomponent beam transported via a gap is related to the VA formation in the drift chamber and to the reflection of ions from the space-charge potential of the VA. The potential necessary to provide for the full stopping of doubly charged ions is lower by $\varepsilon_0/2e$ than that for the singly charged ions. The obtained numerical solution of the Poisson equation (1) showed that partial separation of an ion beam with respect to the charge [3, 7] takes place when the beam is in the second state (curve *ac* in Fig. 1A). We have determined the parameters of the injected beam ensuring complete ion separation (i.e., the regime in which all transmitted ions are singly charged [1, 2]). It has been shown that an effective ion separation regime exists (curve cd_1 in Fig. 1A) in which all singly charged ions are transported via the gap.

REFERENCES

1. S. Humphries, Jr., C. Burkhart, S. Coffey, *et al.*, J. Appl. Phys. **59**, 1790 (1986).
2. S. Humphries, Jr. and H. Rutkowski, J. Appl. Phys. **67**, 3223 (1990).
3. E. Oks, G. Yushkov, I. Litovko, *et al.*, Rev. Sci. Instrum. **73**, 735 (2002).
4. A. S. Bugaev, V. I. Gushenets, A. G. Nikolaev, *et al.*, Zh. Tekh. Fiz. **70** (9), 37 (2000) [Tech. Phys. **45**, 1135 (2000)].
5. R. B. Miller, *Introduction to the Physics of Intense Charged Particle Beams* (Plenum Press, New York, 1982).
6. S. D. Gvozdover, *Theory of Microwave Electron Devices* (Gostekhizdat, Moscow, 1956) [in Russian].
7. V. A. Shklyaev, S. Ya. Belomyttsev, and V. V. Ryzhov, in *Proceedings of the 13th Symposium on High Current Electronics, Tomsk, 2004*, pp. 80–82.

Translated by P. Pozdeev

Technical Physics Letters, Vol. 31, No. 5, 2005, pp. 438–440. Translated from Pis'ma v Zhurnal Tekhnicheskoĭ Fiziki, Vol. 31, No. 10, 2005, pp. 70–75.

High-Power Source of 200–350 nm Spontaneous Emission Excited by Unipolar Current Pulses

D. V. Rybka[a], E. Kh. Baksht[a], M. I. Lomaev[a], A. N. Panchenko[a], V. F. Tarasenko[a,*], M. Krishnan[b], and J. Thompson[b]

[a] *Institute of High-Current Electronics, Siberian Division, Russian Academy of Sciences, Tomsk, Russia*

[b] *Alameda Applied Science Corporation, 94577 San Leandro (CA), USA*

** e-mail: VFT@loi.hcei.tsc.ru*

Received January 13, 2005

Abstract—Spectral, energy, and temporal characteristics of pulse discharge in xenon have been experimentally studied. Upon passing from an oscillatory regime to unipolar pulses of discharge current, the power of emission in the wavelength interval 200–350 nm increases, while the emission pulse full width at half maximum (FWHM) decreases. A quartz pulsed discharge lamp excited by a generator based on high-current high-voltage diodes radiates in the 200–350 nm interval at a peak radiant intensity above 65 kW/sr and at a pulse FWHM ~ 2 μs.

Introduction. In recent years, we have developed a relatively cheap, high-power source of pulsed UV radiation for controlling a diamond-based commutator [1, 2]. For this purpose, it is necessary to ensure that the emission falls predominantly within the spectral range $\lambda \leq 350$ nm ($\lambda \leq 225$ nm corresponds to the fundamental absorption of diamond, whereas the absorption at $\lambda \leq 350$ nm is due to impurities [3, 4]) and that the pulse full width at half maximum (FWHM) does not exceed several microseconds. The most promising radiation sources for this spectral range are offered by xenon pulse discharge lamps [5, 6]. However, an increase in the charging voltage and/or the storage capacitance in such lamps is accompanied by increase in the pulse duration, while the growth of the output radiation power slows down.

The aim of this study was to find the regimes of discharge in xenon such that the output radiation power in the wavelength interval 200–350 nm would significantly increase at a pulse FWHM within several microseconds.

Experimental. The discharge in xenon was powered by a pulse generator with the electrical scheme depicted in Fig. 1. The experiments were performed with two variants of the *LC* oscillator. Variant 1 represented a traditional *LC* oscillator comprising serially connected capacitor bank C_0, a trigatron type switch *S*, and a pulse discharge lamp *FL*. A distinctive feature of variant 2 was the high-current diode array *D* (eight SOS-50-2 diodes [7]) connected parallel to the lamp with inductance L_1.

The main experiments were carried out with a charging voltage of $U_0 = 5$–35 kV, a capacitance of $C_0 = 260$ nF, and a discharge circuit inductance of ~200 nH. The discharge was initiated in a pulsed lamp with an interelectrode gap of 4 mm filled with xenon at a pressure of 550 Torr. The emission was extracted via walls of a quarts cylinder with an inner diameter of 20 mm,

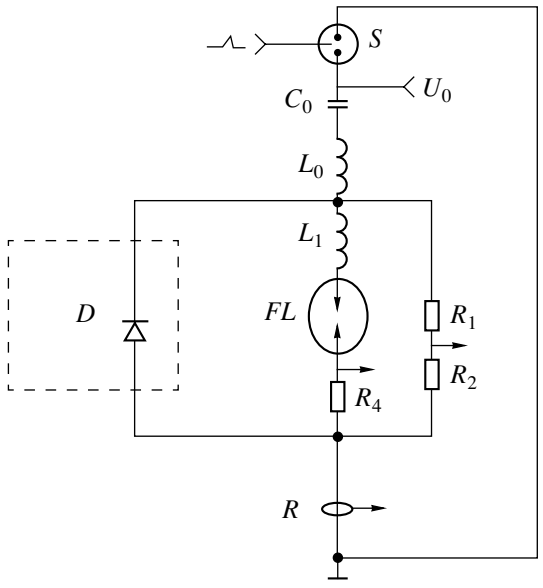

Fig. 1. Electric circuit diagram of the experimental setup: $C_0 = 260$ nF; $L_0 = 30$ nH; $L_1 = 170$ nH; *S*, trigatron switch; *FL*, pulse discharge lamp; *D*, high-current diodes; *R*, Rogowski coil.

1063-7850/05/3105-0438$26.00 © 2005 Pleiades Publishing, Inc.

which transmitted not less than 85% of radiation with $\lambda = 200$–350 nm.

The optical characteristics were studied using a spectrometer (EPP 2000C-25) with a CCD-array photodetector, a diamond detector (AASC Company), and a calibrated coaxial photocell (FEK-22SPU). The dynamics of emission from expanding discharge plasma was monitored using a CCD camera (SensiCam).

Results and discussion. The source operation was characterized by measuring the discharge current, voltage between electrodes, output radiation power, and emission spectrum. We have also obtained photographs of the discharge emission at various moments. Figure 2 shows the typical oscillograms of discharge current and the radiant intensity kinetics measured for the discharge in xenon initiated at various voltages in the scheme with generators 1 and 2. Curves *a* and *b* in this figure characterize the oscillatory regime of discharge current (excited by generator 1), while curves *c* and *d* correspond to unipolar discharge current pulses (excited by generator 2). As can be seen, the radiation power (proportional to the radiant intensity) in the case of a unipolar current pulse increases, while the emission pulse duration (FWHM) decreases compared to the case of generator 1.

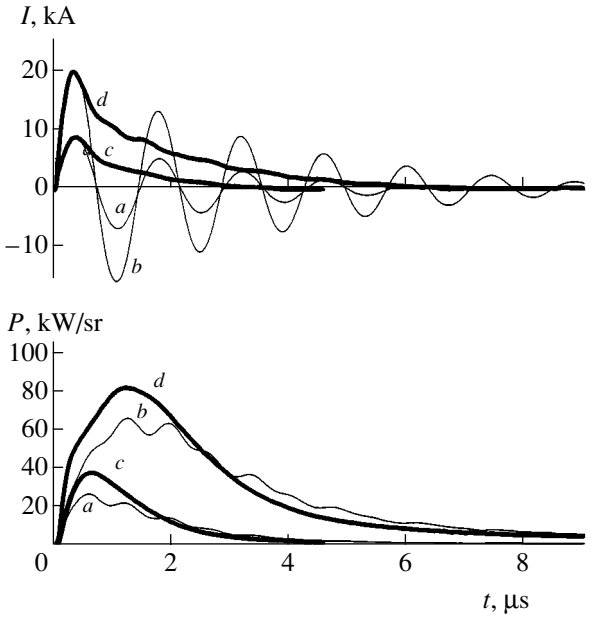

Fig. 2. Kinetics of discharge current I and radiant intensity P of a xenon pulse discharge lamp in a 200–350 nm wavelength interval in a regime of excitation by (*a*, *b*) generator 1 and (*c*, *d*) generator 2 for $U_0 = 9.5$ kV (*a*, *c*) and 24 kV (*b*, *d*).

As was pointed out above, the discharge current in the lamp powered by generator 2 with high-current diodes always passed in one direction. This is explained as follows. When capacitance C_0 is discharged upon switching of the diode voltage from reverse to forward, the diodes shunt the inductance L_1 via the lamp so that the energy stored in this inductance is transferred via the newly formed L_1–*D*–*FL* circuit. It should be noted that the magnitude of current at the moment of voltage switching is close to maximum because the active resistance of the *S*–S_0–*FL* circuit at this moment is much lower than its wave impedance. The current of L_1 discharge via the L_1–*D*–*FL* circuit decreased according to exponential law with a time constant $\tau \sim L_1/R_c$, where R_c is the active resistance of this circuit. At the same time, the current via the diode–lamp (*D*–*FL*) circuit measured by a Rogowski coil (*R* in Fig. 1) had the shape of decaying oscillations.

The observed increase in the output radiation power of the pulse discharge lamp excited by generator 2 (compared to generator 1) can be explained by the absence of pulsation in the excitation power (i.e., in the power supplied to discharge). When the lamp is excited by generator 1 (traditional *LC* oscillator) at a voltage above several kilovolts, the discharge regime acquires an oscillatory character and the excitation power exhibits unavoidable pulsation. As the excitation power decreases to zero, the discharge plasma cools down. This, in turn, leads to pulsation in the output radiation power (Fig. 2, curves *a* and *b*). At large U_0 values, the maximum output power is reached in the second peak of emission (after the second half-period of the current). In the case of excitation by generator 2, the current passes only in one direction and the pulsation of power supplied to discharge is smoothened. This leads to an increase in the peak radiant intensity (in our experiments, by ~30%) and a decrease in the emission pulse duration (FWHM).

In the case of discharge excitation by generator 2, the energy emitted in the 200–350 nm wavelength interval reached ~2 J at an efficiency of ~8.5% with respect to the energy supplied to discharge. The peak radiant intensity in the 200–350 nm interval was above 65 kW/sr. It should be noted that an increase in the peak output radiation power for the lamp excited by generator 2 (as compared to the case of generator 1) is not accompanied by a decrease in the energy of the emission pulse.

Conclusions. We demonstrated that the passage from oscillatory to unipolar regime of discharge current leads to an increase in the output radiation power and a decrease in the emission pulse width (FWHM). The spectral, energy, and temporal characteristics of pulse discharge in xenon have been experimentally studied using a lamp excited by generators of two types. A high-power source of spontaneous emission based on high-current pulse discharge in xenon is created. The emission pulse energy in a wavelength interval from 200 to 350 nm is ~2 J at an 8.5% efficiency of the electric to radiant energy conversion. The proposed lamp radiates in the 200–350 nm interval at a peak radiant intensity above 65 kW/sr and a pulse FWHM ~ 2 μs.

Acknowledgments. This study was supported in part by the US Civilian Research and Development Foundation (CRDF Grant no. RP2-538-TO-02).

REFERENCES

1. M. I. Lomaev, D. V. Rybka, V. F. Tarasenko, *et al.*, Izv. Vyssh. Uchebn. Zaved., Fiz., No. 1, 81 (2004).
2. D. V. Rybka, E. Kh. Baksht, M. I. Lomaev, *et al.*, Zh. Tekh. Fiz. **75** (2), 131 (2005) [Tech. Phys. **50**, 270 (2005)].
3. J. E. Field, *The Properties of Diamond* (Academic, London, 1979).
4. G. B. Bokiĭ, G. N. Bezrukov, Yu. A. Klyuev, A. M. Naletov, and V. I. Nepsha, *Natural and Synthetic Diamonds* (Nauka, Moscow, 1986) [in Russian].
5. *Encyclopedia of Low-Temperature Plasma Physics: Introductory Volume 4*, Ed. by V. E. Fortov (Nauka, Moscow, 2000) [in Russian].
6. G. N. Rokhlin, *Discharge Sources of Light* (Énergoatomizdat, Moscow, 1991) [in Russian].
7. S. N. Rukin, Prib. Tekh. Éksp., No. 4, 5 (1999).

Translated by P. Pozdeev

Technical Physics Letters, Vol. 31, No. 5, 2005, pp. 441–443. Translated from Pis'ma v Zhurnal Tekhnicheskoĭ Fiziki, Vol. 31, No. 10, 2005, pp. 76–82.

Anomalous Scenario of the Dynamic Chaos Onset in Multimode Laser Diodes

G. G. Akchurin* and A. G. Akchurin

Saratov State University, Saratov, Russia

** e-mail: AkchurinGG@mail.ru*

Received December 29, 2004

Abstract—Anomalous transition to the regime of dynamic chaos in a multimode quantum-well heterolaser (λ = 635 nm) is possible as a result of an injection-current-induced change in the gain. A stable multimode regime (featuring more than ten longitudinal modes) is established near the lasing threshold under conditions of weak nonlinear coupling. As the injection current increases, the competition of modes results in a partial suppression of weak laser modes. At a certain excess of the gain over losses, a regime with hard excitation of four modes is realized that is characterized by the onset of a dynamic chaos manifested by irregular amplitude pulsation of modes, broadening of the optical spectrum, and loss of coherence. The loss of coherence is revealed by a decrease in the visibility of interference bands and by their chaotic shifts. An increase in the overall nonlinear coupling and the corresponding competition of modes leads to a decrease in the dimension of the self-oscillatory system and to the onset of a stable single-mode lasing regime. © *2005 Pleiades Publishing, Inc.*

Introduction. Multimode lasing regimes are typical of semiconductor and solid-state lasers with amplification bandwidths from hundreds of GHz to tens of THz and a mode frequency separation from hundreds of MHz to hundreds of GHz [1]. Laser diodes may feature up to several tens of modes, while solid-state lasers, from several tens (in YAG:Nd microlasers) up to several tens and even hundreds of thousands (in titanium-sapphire lasers) [2]. Ultrashort laser pulses are obtained in the regime of forced mode locking, whereby the number of phase-locked modes determines the laser pulse width ranging from hundreds of picoseconds to tens of femtoseconds [3, 4]. Recently, we discussed features of the onset of chaotic regimes upon breakage of the regime of forced mode locking, which takes place in multimode solid-state lasers during cavity tuning and leads to laser pulse broadening and irregular generation, as can be observed in both real and numerical experiments [5].

Possible scenarios of the onset of dynamic chaos in single-mode lasers and those operating in nonautonomous regimes were reviewed by Oraevskiĭ [6]. In semiconductor lasers, the most thoroughly studied were the regimes of transition to chaos via period-doubling cascades realized in systems with delayed optical feedback [7–9].

Modern nonlinear dynamics has established the main mechanisms of the development of instability and the principal scenarios of the transition to chaos in dissipative nonlinear systems [10–12]. In recent years, centers of research in nonlinear dynamics have extensively studied the features of chaos onset in model chains and arrays of van der Pol oscillators linked by bonds of various types; there were also attempts at numerical modeling of distributed nonlinear systems [13, 14]. The main scenario of dynamic chaos onset in a system of coupled oscillators (called the Ruelle–Takens scenario) is based on notions about the breakage of quasi-periodicity (three-dimensional torus) and the appearance of a strange attractor [15].

In laser physics, this mechanism of transition to chaos was repeatedly observed in experiments with gas-discharge lasers. Prior to the development of the ideology of nonlinear dynamics, this regime was referred to as the "nonsynchronized laser noise."

We have experimentally realized the Ruelle–Takens scenario of transition to chaos in autonomous coupled oscillators using a gas-discharge He–Ne laser (λ = 633 nm) with a mode frequency separation on the order of 250 MHz and an amplification bandwidth of 1.5 GHz. At the lasing threshold, the system features a single-mode regime. An increase in the gain achieved by means of increasing the discharge current leads to the sequential excitation of two and three modes, which exhibit significant competition only in a symmetric regime. However, excitation of the fourth mode was accompanied by a jumplike appearance of strong low-frequency power fluctuations which were manifested by a broadening of the spectrum of beats in the longitudinal modes, and by a nonstationary and noisy optical spectrum (observed using a scanning Fabry–Perot interferometer [17]).

This paper presents experimental results showing evidence of dynamic chaos onset via a scenario substantially different from the classical Ruelle–Takens model. The new transition regime was observed in a multimode semiconductor quantum-well laser in the

1063-7850/05/3105-0441$26.00 © 2005 Pleiades Publishing, Inc.

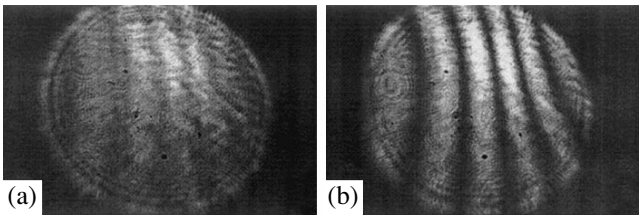

Fig. 1. A change in the contrast of interference bands observed using a Jamin interferometer in response to a growth in the control parameter $\beta = I/I_{th}$ (gain excess over threshold) with increasing injection current in a quantum-well laser diode ($\lambda = 635$ nm): (a) dynamic chaos with hard excitation of four longitudinal modes frequency-separated by $\Delta\nu = 130$ GHz ($I = 16$ mA; $\beta \sim 1.6$); (b) stable single-mode lasing regime ($I = 20$ mA; $\beta = 2$).

course of variation of control parameters, such as the gain. This anomalous scenario of dynamic chaos onset has been observed for the first time in a distributed self-oscillatory system and is of interest both for laser physics and for nonlinear physics in general.

Experimental methods and results. The regime of dynamic chaos was observed in a semiconductor quantum-well injection heterolaser ($\lambda = 635$ nm) with a typical linewidth on the order of 1.5 THz and a mode frequency separation of 130 GHz. The traditional method of observation of chaotic regimes in lasers, which is based on the analysis of intermode beats in the RF frequency range, was inapplicable because of the extremely high frequency of these beats. However, this method makes possible direct investigation of the optical spectrum with the aid of optical diffraction spectrometers. We used a high-resolution spectrometer of the DFS-3 type. The optical spectrum of laser modes was detected by a digital CCD camera (VideoScan), which allowed the spectra to be recorded at a rate of 30 shots per second. This method provided a spectral resolution of 16 GHz with respect to the mode width, and ensured the detection of minimum frequency shifts at a resolution of 2 GHz. The time correlation function was measured using a Michelson angle interferometer. In addition, we monitored the visibility of interference bands (which allowed us to estimate the degree of incoherency breakage) with the aid of a Jamin interferometer and a CCD camera.

In the case of excitation near the lasing threshold (for the gain excess over losses $\beta = I/I_{th} < 1.1$), the laser featured more than ten stable modes with an asymmetric Lorentz envelope. The time coherence function appears as the typical quasi-periodic function (with a period of 1.48 mm/s = 4.95 ps) with $N - 1$ minima, where N is the number of laser modes. Below the lasing threshold, the coherence length did not exceed 50 μm.

As the injection current was increased, the total power exhibited linear growth. However, this was accompanied by an increase in the nonlinear interaction of modes leading to partial suppression of their amplitude, especially of weak modes at the line edge. The increase in nonlinearity led to an increase in the competition of modes; as a result, the number of modes decreased but their spectrum remained stable, albeit dependent (at a fixed current) on the mode frequency tuning relative to the center of the laser line. At a certain excess over threshold ($\beta \sim 1.6$), four longitudinal modes with comparable intensities are excited in a jumplike manner. Simultaneously, the mode spectrum revealed the onset of strong pulsation in the mode intensity, broadening of the optical spectrum, a nonstationary character of the coherence function, sharp decrease in the contrast of interference bands, and their chaotic deviations. Detailed investigation of the contrast and chaotic dynamics of the interference bands showed their relation to the onset of strong phase fluctuations. Recently, we observed such chaotic phase fluctuations in the interference signal of waveguide modes as manifested by the irregular dynamics of the speckle field in laser-probed optical fibers [18].

Figure 1 shows the typical interference patterns observed in the regimes of (a) dynamic chaos and (b) stable single-mode lasing related to an increase in nonlinearity. The regime featuring three to four modes is also nonstationary and strongly depends on the tuning of cavity modes relative to the center of the laser line. As the injection current is increased further (and the degree of nonlinearity grows accordingly), the system exhibits a transition to the regime of stable double-mode lasing, with a jumplike switching to the single-mode regime as a result of the cavity frequency drift. On a level of double-threshold gain for lasers of the given type, we observed a regime of stable sing-mode lasing with a coherence length exceeding several meters.

Thus, the observed evolution of bifurcation regimes and a nontraditional scenario of the transition to dynamic chaos with increasing degree of nonlinearity substantially differ from the classical behavior. This difference is probably related to the type of intermode coupling. In the case of a semiconductor laser with a homogeneous Lorentz emission line, the longitudinal modes are globally coupled. In a gas laser with a Doppler emission line, where the Ruelle–Takens scenario is realized, the modes selectively interact with certain atomic groups and the adjacent modes are most strongly coupled. It should be noted that the parameter of mode coupling is frequency-dependent and may change when the cavity length is tuned within $\lambda/2$, which will influence the thresholds for the onset of chaotic regimes. Diode-pumped solid-state YAG:Nd microlasers with intracavity second-harmonic generator ($\lambda = 532$ nm) also exhibit chaotic regimes upon the excitation of three to four modes, which are related to thermal drift of the cavity length. However, the features of complicated chaotic dynamics arising in such lasers for certain cavity tuning parameters require additional investigation.

Thus, we have experimentally observed an anomalous scenario of the transition to chaos in a nonlinear system with global coupling in response to a control parameter such as the gain excess over losses. Strong nonlinear interaction in the coupled multimode self-oscillatory system can lead (via mode competition) to a decrease in the system dimension and to the realization of a single mode regime.

We believe that the results presented above are not only important from the standpoint of basic nonlinear dynamics, but they are also significant for practical applications, since semiconductor lasers are now widely used in information technologies. Knowledge of complex nonlinear dynamic regimes in distributed self-oscillatory systems will provide for developing technologies of low-noise signal generation.

Acknowledgments. The authors are grateful to D.I. Trubetskov and L.A. Mel'nikov for fruitful discussions of results.

This study was supported by the Presidential Program of Support for Leading Scientific Schools in Russia (project no. NSh-25.2003.2) and the US Civilian Research and Development Foundation for the Independent States of the Former Soviet Union (CRDF grant no. REC-006).

REFERENCES

1. *Semiconductors and Semimetals*, Vol. 22: *Lightwave Communications Technology*, I. *Semiconductor Injection Lasers*, Ed. by W. T. Tsang (Academic, New York, 1985).
2. R. Holzwarth, Th. Udem, T. W. Hänsch, *et al.*, Phys. Rev. Lett. **85**, 2264 (2000).
3. J. Herrmann and B. Wilhelmi, *Lasers for Ultrashort Light Pulses* (North-Holland, Amsterdam, 1987; Mir, Moscow, 1986).
4. P. G. Kryukov, Kvantovaya Élektron. (Moscow) **31**, 95 (2001).
5. A. G. Akchurin, G. G. Akchurin, and L. A. Melnikov, in *Proceedings of the International Conference on Synchronization of Chaotic and Stochastic Oscillations, SYNCHRO 2002, Saratov, 2002*, p. 14.
6. A. N. Oraevskiĭ, Izv. Vyssh. Uchebn. Zaved., Prikl. Nelin. Din. **4**, 3 (1996).
7. R. Lang and K. Kobayashi, IEEE J. Quantum Electron. **16**, 347 (1980).
8. J. Mork *et al.*, IEEE J. Quantum Electron. **28**, 93 (1992).
9. J. P. Goedgebuer *et al.*, IEEE J. Quantum Electron. **34**, 594 (1998).
10. M. I. Rabinovich and D. I. Trubetskov, *Introduction to the Theory of Oscillations and Waves* (Nauka, Moscow, 1984; Kluwer, Dordrecht, 1989).
11. P. Berge, Y. Pomeau, and C. Vidal, *Order Within Chaos* (Wiley, New York, 1987; Mir, Moscow, 1991).
12. S. P. Kuznetsov, *Dynamical Chaos* (Fizmatlit, Moscow, 2001) [in Russian].
13. V. S. Anishchenko, T. E. Vadivasova, and V. V. Astakhov, *Nonlinear Dynamics of Chaotic and Stochastic Systems* (Saratov State University, Saratov, 1999) [in Russian].
14. A. A. Akopov, T. E. Vadivasova, V. V. Astakhov, *et al.*, Izv. Vyssh. Uchebn. Zaved., Prikl. Nelin. Din. **11** (4–5), 66 (2003).
15. D. Ruelle and F. Takens, in *Strange Attractors*, Ed. by Ya. G. Sinaĭ and L. P. Shil'nikov (Mir, Moscow, 1981) [in Russian].
16. G. G. Akchurin, A. R. Kristallov, L. A. Mel'nikov, *et al.*, Obz. Elektron. Tekh., Ser. 11: Lazernaya Tekh. Optoelektron. **4**, 850 (1981).
17. G. G. Akchurin, in *Proceedings of the 10th International Conference on Coherent and Nonlinear Optics, Moscow, 1985*, p. 32.
18. G. G. Akchurin and A. G. Akchurin, Pis'ma Zh. Tekh. Fiz. **30** (24), 56 (2004) [Tech. Phys. Lett. **30**, 1045 (2004)].

Translated by P. Pozdeev

Technical Physics Letters, Vol. 31, No. 5, 2005, pp. 444–445. Translated from Pis'ma v Zhurnal Tekhnicheskoĭ Fiziki, Vol. 31, No. 10, 2005, pp. 83–87.

Effect of Pressure on the Properties of a Silicon–Glass Interface

S. I. Vlasov*, M. A. Ergasheva, and T. P. Adylov

National University of Uzbekistan, Tashkent, Uzbekistan

** e-mail: vlasov@uzcsi.ru*

Received January 10, 2005

Abstract—The effect of hydrostatic pressure on the energy distribution of surface states localized at the boundary between silicon (Si) and a lead borosilicate glass ($PbO–SiO_2–B_2O_3–Al_2O_3–Ta_2O_5$) has been studied. At a pressure of 8 kbar, donor centers are formed in a layer of glass adjacent to the silicon–glass interface, which are capable of participating in electron exchange with the semiconductor. © *2005 Pleiades Publishing, Inc.*

Interphase boundaries between semiconductors and dielectrics, which are formed by means of thermal oxidation of a semiconductor substrate, contain a large number of stressed and unsaturated valence bonds that make such interfaces highly sensitive to external pressure. The pressure-induced changes in the properties of semiconductor–dielectric interfaces are probably caused by mechanical stresses, which stimulate the gettering of thermal defects from the bulk of semiconductor, or by impurities localized in the transition layer and interacting with the surface states [1].

Low-melting glasses deposited onto a semiconductor surface at reduced temperatures decrease the probability of thermal defect formation and reduce mechanical stresses at the interface. This paper presents the results of investigations of the effect of hydrostatic compression on the properties of a boundary between single crystal silicon and a lead borosilicate glass.

The experiments were performed with a mixed oxide glass of the $PbO–SiO_2–B_2O_3–Al_2O_3–Ta_2O_5$ type (PbO, 49%; SiO_2, 32%; B_2O_3, 15%; Al_2O_3, 3%; Ta_2O_5, 1%) deposited onto ⟨111⟩-oriented single silicon plates (KEF-5 grade). The glass was deposited by applying a fine-disperse powdered glass with subsequent fusion (T = 680°C) and annealing (T = 470°C) [2]. The electrical measurements were performed on metal–glass-semiconductor (MGS) structures obtained by the deposition of aluminum onto the outer glass and semiconductor surfaces. The area of a control electrode formed on the glass surface was $S = 0.2$ cm^2.

The samples of MGS structures were subjected to uniform (hydrostatic) compression at 8 kbar on a Gidrostat LG-16 setup. The electrical properties of samples were studied by methods of high-frequency (1 MHz) capacitance–voltage characteristics and isothermal relaxation of capacitance [3] in the MGS structures. Using the results of measurements, the density of surface states was calculated using well-known relations [4].

Figure 1 shows the distribution of the density of surface states over the bandgap of silicon for one of the MGS structures compressed at 8 kbar (curve *1*) in comparison to the data for a control (uncompressed) sample (curve *2*). As can be seen, the dN_{SS}/dE spectrum of the compressed sample exhibits an additional peak with a maximum at E_c – 0.39 eV. According to commonly accepted notions, the formation of maxima in the dN_{SS}/dE spectrum is related to the impurity centers localized either in the space charge region of the semiconductor [6] or in a layer of glass adjacent to the silicon–glass interface [7]. In order to elucidate the role of impurity centers localized in the semiconductor, we removed the glass from MGS structures by chemical etching and formed a Schottky barrier by means of the

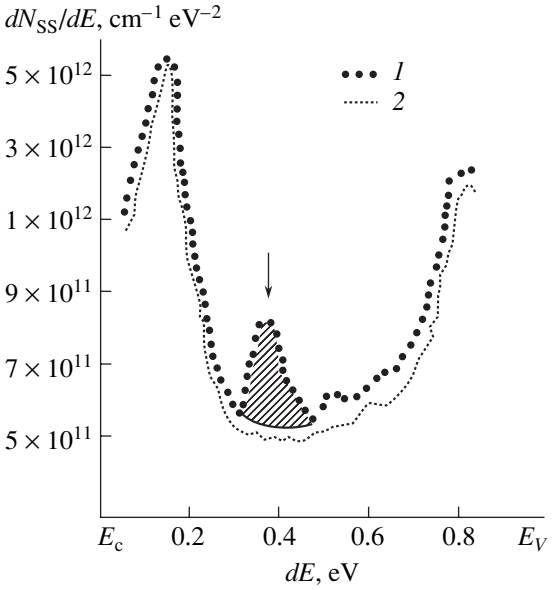

Fig. 1. Energy distribution of the differential density of surface states in (*1*) hydrostatically compressed (8 kbar) and (*2*) control (uncompressed) MGS structures. The arrow indicates a peak due to the pressure-induced donor centers.

1063-7850/05/3105-0444$26.00 © 2005 Pleiades Publishing, Inc.

vacuum deposition of gold. The concentration and energy spectrum of deep centers in this structure were studied by measuring the isothermal relaxation of capacitance. It was established that all Schottky barriers prepared using compressed structures exhibit recharge of centers with an ionization energy of $E_c - 0.4$ eV and a concentration of $N_b = 3 \times 10^{12}$ cm^{-3}.

The observed temperature dependence (Fig. 2) of the time constant τ of relaxation of the population of these centers ($\tau(T)$ plots [3]) was not identical to the $\tau(T)$ curves reported in the literature [3, 8, 9]. The charge related to the new centers (estimated assuming their homogeneous distribution over the entire thickness of the space charge region of silicon) was calculated as $Q = qN_bSd = 3 \times 10^{-11}$ C. On the other hand, a charge corresponding to the maximum in the density of surface states (see the crosshatched area under curve *2* in Fig. 1) is $Q_{SS} = qN_{SS}SdE = 2 \times 10^{-7}$ C. A comparison of the two estimates shows that deep centers with the concentration indicated above cannot account for the appearance of the maximum observed in the density of surface states.

In order to determine the influence of charges localized in the glass on the density of surface states, we used the temperature dependence of the dielectric loss tangent ($\tan\delta$) for the control and compressed samples measured at a frequency of 1 MHz and a bias voltage of 4 V in the temperature interval from –30 to +20°C. A comparison of the results of these measurements showed that the $\tan\delta(T)$ curve for the control (uncompressed) structure exhibits a well-pronounced relaxation maximum at $T_m = -20$°C, while the structures upon compression exhibit an increase in the level of losses and a shift of the relaxation maximum toward higher temperatures ($T_m = 5$–8°C).

Recently, we demonstrated [5] that analogous structures upon compression exhibit hysteresis phenomena. It was suggested that this behavior is related to the appearance of charged centers in the layer of glass adjacent to the semiconductor. In order to check the hypothesis formulated in [5], we cooled the sample structures to –30°C and applied short (0.2–0.3 s) enrichment bias voltage pulses with an amplitude of 30–35 V. Then, a constant enrichment bias voltage was applied (+8 V) and the temperature was increased to 20°C. At this temperature, we measured the capacitance–voltage characteristics, determined the dN_{SS}/dE distribution over the semiconductor bandgap, and compared these distributions obtained for the structures treated as described above to the spectra in Fig. 1. This comparison showed that the action of a pulsed enrichment voltage decreased the amplitude of the dN_{SS}/dE peak at $E_c - 0.4$ eV by a factor of 2–3. However, the 2-h treatment of these samples at $T = 50$°C, with application of a depletion voltage (–18 V), restored the spectrum of the density of surface states, whereby it acquired the same shape as in Fig. 1.

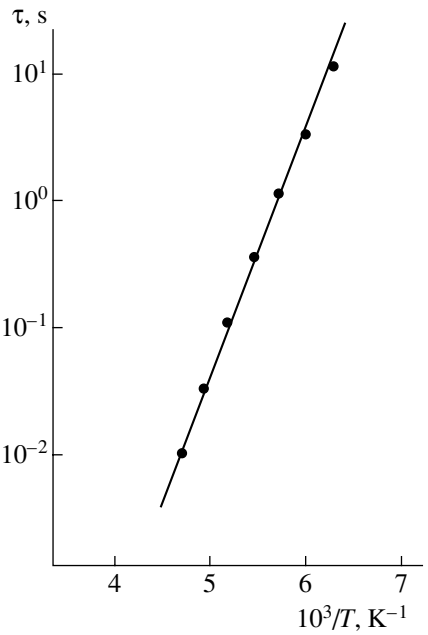

Fig. 2. The temperature dependence of the time constant τ of relaxation of the population of pressure-induced donor centers at the silicon–glass interface.

Based on the above results, we make the following conclusions. Modification of the spectrum of dN_{SS}/dE in MGS structures upon hydrostatic compression is caused by structural changes in the layer of glass adjacent to the silicon–glass interface. These changes lead to the appearance of donor centers capable of participating in electron exchange with the semiconductor.

REFERENCES

1. P. B. Parchinskiĭ and S. I. Vlasov, Mikroélektronika **30**, 466 (2001).
2. P. B. Parchinskiĭ, S. I. Vlasov, and U. T. Turgunov, Neorg. Mater. **38**, 750 (2002).
3. L. S. Berman and A. A. Lebedev, *Deep Level Transient Spectroscopy in Semiconductors* (Nauka, Leningrad, 1981) [in Russian].
4. A. P. Gorban, V. G. Litovchenko, and P. Ch. Peikov, Phys. Status Solidi A **10**, 289 (1973).
5. S. I. Vlasov, M. A. Ergasheva, and T. P. Adylov, in *Proceedings of the Conference on Photoelectric Phenomena in Semiconductors, Tashkent, 2004*, pp. 71–72.
6. S. I. Vlasov, S. Z. Zaĭnabidinov, I. N. Karimov, and A. A. Nasirov, Fiz. Tekh. Poluprovodn. (Leningrad) **21**, 764 (1987) [Sov. Phys. Semicond. **21**, 467 (1987)].
7. S. I. Vlasov, P. B. Parchinskiĭ, and L. G. Ligai, Mikroélektronika **32**, 121 (2003).
8. L. S. Berman, S. I. Vlasov, and V. F. Morozov, Izv. Akad. Nauk SSSR, Ser. Fiz. **42**, 1175 (1978).
9. J. W. Chen and A. G. Milnes, Ann. Rev. Mater. Sci. **10**, 157 (1980).

Translated by P. Pozdeev

Technical Physics Letters, Vol. 31, No. 5, 2005, pp. 446–448. Translated from Pis'ma v Zhurnal Tekhnicheskoĭ Fiziki, Vol. 31, No. 10, 2005, pp. 88–94.

On the Possibility of Increasing the Efficiency of Sealed-Off Nitrogen Lasers

A. I. Fedorov

Institute of the Optics of Atmosphere, Siberian Division, Russian Academy of Sciences, Tomsk, Russia

e-mail: fedorov@asd.iao.ru

Received January 12, 2005

Abstract—A sealed-off nitrogen laser operating in a periodic-pulse regime at a repetition rate of 40 Hz has been experimentally studied and it is demonstrated that the laser efficiency can be increased by quasi-stationary energy pumping into the active medium (pure nitrogen or its mixtures with helium or neon). The presence of a buffer gas (helium or neon) allows the energy parameters of radiation to be increased and the laser efficiency to be controlled. A small-sized sealed-off nitrogen laser is developed, which operates at a peak output power of 160 kW and a pulse energy of 0.8 mJ with an efficiency of 0.27%. © *2005 Pleiades Publishing, Inc.*

Small-sized sealed-off nitrogen lasers operating in a periodic-pulse regime are promising sources of radiation in the near UV range. These sources are used for pumping organic dues in laser chemistry, in spectroscopic investigations, in gas-discharge plasma diagnostics, etc. [1]. The advantages of nitrogen lasers are simple operation, chemical inertness of the active medium, and relatively low cost in comparison to excimer lasers. In some applications, the wavelength (337.1 nm) of lasing in the second positive system of bands ($C^3\Pi_u$–$B^3\Pi_g$) of molecular nitrogen has proved to be most effective. Using these lasers, it is also possible to obtain radiation in the near IR range by using the positive system of bands ($B^3\Pi_g$–$A^3\Sigma_u$) of molecular nitrogen. Moreover, nitrogen lasers are capable of simultaneously operating in the UV and IR spectral intervals, which significantly expands the field of possible applications.

The disadvantages of nitrogen lasers are their low energy efficiency (<0.1%), low output energy per pulse (≤0.1 mJ), limited working life of the active medium (~10^6 pulses), and large divergence of the output radiation. However, rough estimates obtained by Godard [3] showed that the efficiency of nitrogen lasers may reach up to 4%. Then, lasers with efficiencies from 0.4 to 3% were reported [4–6], in which an increase in the efficiency was achieved due to the development of special elements of the excitation system and their matching to the active volume. It was also demonstrated that it is possible to increase the laser pulse duration up to 40 ns [7–9], raise the output pulse energy up to 30 mJ [6, 8, 10, 11], and decrease the output beam divergence [9, 11–13].

Numerous attempts at the mathematical modeling of processes in nitrogen lasers were mostly restricted to the systems pumped by fast discharge and yielded no satisfactory agreement with available experimental data. This situation hinders the search for conditions favoring the creation of lasers with the desired characteristics (in particular, high efficiencies) for the traditional methods of pumping. For this reason, much effort is devoted to experimental investigations aimed at the development of an effective nitrogen laser [6, 14–17].

This paper considers the possibility of increasing the efficiency of a periodic-pulse nitrogen laser by means of quasi-stationary energy pumping into the active medium (pure nitrogen or its mixtures with helium or neon) [9, 18]. The nitrogen laser operated in a sealed-off regime at a pulse repetition rate of up to 40 Hz. The laser characteristics were studied using a setup described in detail elsewhere [13]. The transverse excitation discharge was initiated in a $7 \times 5 \times 200$ mm active volume with a buffer volume of 1 liter. The active medium was energy-pumped from a capacitive circuit with a crown-discharge UV preionization. Using this scheme of pumping, it was possible to provide for a self-consistent regime of the excitation energy pumping to the active medium [9]. The pumping scheme was switched by a commercial discharger of the RU-62 type. The capacitive source was charged to a constant voltage of 10 kV. The experiments were performed with technical-grade nitrogen and spectroscopic-grade helium and neon.

The discharge and energy parameters of the laser filled with nitrogen or its mixtures with helium or neon were studied in a pulse repetition regime. The maximum parameters of laser radiation for the optimum working pressures of nitrogen (P_0) and various pulse repetition rates f are presented in the table. The laser operation was characterized by the average output power W_0, pulse power W_1, pulse energy E_1, and efficiency η. The laser pulse full width at half height (FWHM) was 5 ns. An analysis of these results shows that the maximum parameters of laser radiation are obtained at a low repetition rate (3 Hz), where a pulse

1063-7850/05/3105-0446$26.00

power of 160 kW and a pulse energy of 0.8 mJ were reached at a practical efficiency of 0.27%, which is much higher than that achieved with the traditional pumping scheme employing the Blumlain generator. As the repetition rate is increased to 10 Hz, the laser efficiency decreases by a factor of about 4 and then varies rather slightly when the repetition rate is further increased to 40 Hz. A maximum average power of 3.8 mW was obtained at a laser efficiency of 0.03%. This behavior of the radiation parameters is related to the features of energy deposition in the discharge at a fixed charging voltage of 10 kV.

Analogous experiments aimed at increasing the laser efficiency were performed for the working mixtures of nitrogen with helium and neon in the range of working pressures from 30 to 760 Torr. Figure 1 shows plots of the average radiation power for N_2–He mixtures with the partial pressure of helium varied from 15 to 610 Torr. The measurements were performed at a fixed nitrogen pressure in the range from 15 to 150 and a pulse repetition rate of 10 Hz. No lasing was observed in pure nitrogen at a pressure of 15 Torr. An increase in the helium content in the mixture provided a linear increase in the average power to 0.7 mW at a total pressure of 200 Torr. In this case, the radiation pulse power exhibited a nearly tenfold growth, remained constant as the helium pressure was increased to 500 Torr, and then gradually decreased to 0.5 mW at a working pressure of about 1 atm (~1 bar).

The average power of 0.7 mW observed at a nitrogen pressure of 30 Torr corresponds to a maximum power for the N_2–He (1 : 19) mixture with 15 Torr of N_2. This power exhibited a twofold growth for the N_2–He (1 : 9) mixture with 30 Torr of N_2. The average power of 1.4 mW observed at a nitrogen pressure of 60 Torr corresponds to a maximum power for the N_2–He (1 : 9) mixture with 30 Torr of N_2. This power exhibited a 30% increase for the N_2–He (1 : 4) mixture with 60 Torr of helium. The average power of 1.9 mW observed at a nitrogen pressure of 90 Torr almost corresponds to a maximum power for the N_2–He (1 : 4) mixture with 60 Torr of N_2. This power exhibited only a 10% increase for the N_2–He (1 : 1–3) mixture with 90 Torr of N_2. It should be noted that the average power for pure nitrogen at a pressure not exceeding 60 Torr can be much lower than or equal to the power level achieved in N_2–He mixtures at 1 atm.

The maximum radiation power of 2.25 mW obtained at a nitrogen pressure of 120 Torr linearly decreased upon the addition of helium, until reaching half of the initial level in the mixture at 1 atm. An analogous situation was observed for a nitrogen pressure of 150 Torr, where the average radiation power dropped to nearly zero at 1 atm. This decrease in the average radiation power with increasing helium pressure is related to contraction of the discharge and is caused by a small electron density created in the gap by the UV preionization source. The electron density was limited by the power source operating at a constant charging voltage of 10 kV.

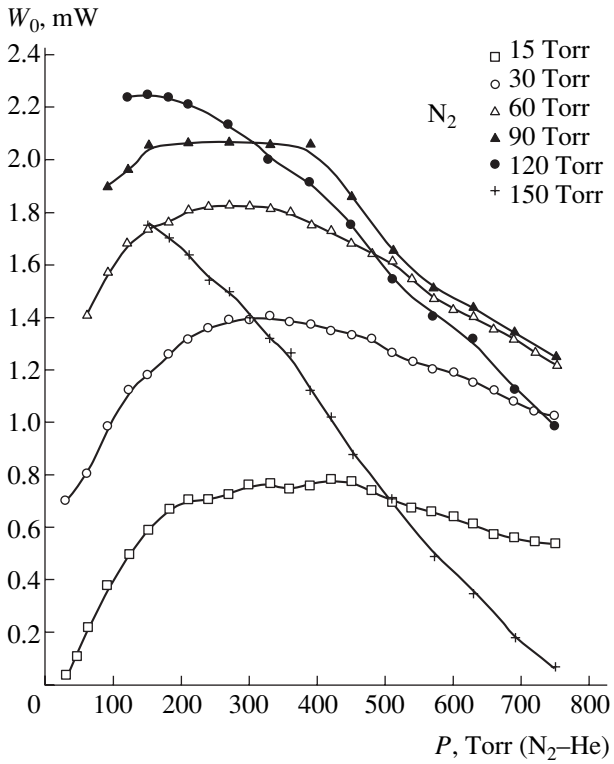

Fig 1. Plots of the average output radiation power versus partial pressure of helium in N_2–He mixtures with various fixed pressures of nitrogen for a sealed-off laser operating at a pulse repetition rate of 10 Hz.

Figure 2 shows analogous plots of the average radiation power for N_2–He mixtures with the partial pressure of neon varied from 15 to 610 Torr. The measurements were performed at a fixed nitrogen pressure in the range from 15 to 150 Torr and a pulse repetition rate of 10 Hz. For a nitrogen pressure of up to 60 Torr, the shapes and amplitudes of the curves for the mixtures with neon are almost identical to those for the nitrogen–helium mixtures. At a nitrogen pressure of 90 Torr, the neon additive increases the maximum radiation power

Maximum output radiation parameters of a sealed-off nitrogen laser operating at optimum nitrogen pressures and various pulse repetition rates

f, Hz	P_0, Torr	W_0, mW	W_1, kW	E_1, mJ	η, %
3	120	2.4	160	0.8	0.27
10	120	2.1	42	0.21	0.07
20	120	3	30	0.15	0.05
30	90	3.5	23	0.12	0.04
40	90	3.8	19	0.095	0.03

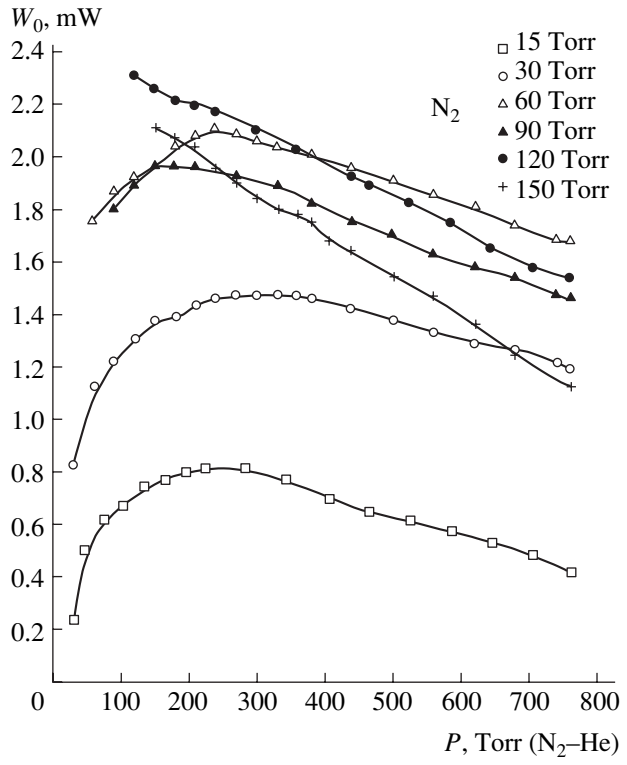

Fig 2. Plots of the average output radiation power versus partial pressure of neon in N_2–He mixtures with various fixed pressures of nitrogen for a sealed-off laser operating at a pulse repetition rate of 10 Hz.

by only 8% in an N_2–Ne (1 : 1) mixture, but this maximum is still lower than that in the N_2–Ne (1 : 3) mixture with 60 Torr of nitrogen. Another characteristic feature of the mixtures with neon is that, at high nitrogen pressures, the neon additives linearly decrease the average radiation power. This power decreases at 1 atm to a level less than half of that for the analogous mixtures with helium.

Thus, an analysis of the results of this investigation showed that the output radiation parameters of nitrogen lasers can be significantly increased by adding a buffer gas (helium or neon) at a fixed nitrogen pressure of up to 60 Torr. The choice between these the two buffer gases is not important for the working pressures about 0.5 atm. At lower pressures, it is better to use nitrogen–helium mixtures, while neon is recommended as a buffer gas in nitrogen at a nearly atmospheric pressure.

Conclusions. (i) A sealed-off nitrogen laser pumped in a quasi-stationary regime can operate at a peak output power of 160 kW and a pulse energy of 0.8 mJ with the high practical efficiency of 0.27%.

(ii) Adding a buffer gas (helium or neon) to nitrogen provides for a significant increase in the output radiation parameters and, hence, in the efficiency of a sealed-off nitrogen laser.

(iii) A sealed-off nitrogen laser with high output radiation parameters, operating at a repetition rate of 40 Hz in a range of working gas pressures from 30 to 760 Torr, has been developed and experimentally studied.

REFERENCES

1. A. M. Razhev and G. G. Telegin, Zarubezhn. Radioélektron., No. 3, 76 (1978).
2. V. O. Lisitsyn, A. R. Sorokin, and G. G. Telegin, Kvantovaya Élektron. (Moscow) **2**, 1710 (1975).
3. J. P. Girardeau-Mountaunt, Nouv. Rev. Opt. **25**, 341 (1974).
4. B. Godard, IEEE J. Quantum Electron. **10**, 147 (1974).
5. B. Oliveira dos Santos, C. E. Fellows, J. B. de Oliveira e Souza, *et al.*, Appl. Phys. B **41**, 241 (1986).
6. H. Seki, S. Takemori, and T. Sato, IEEE J. Sel. Top. Quantum Electron. **1**, 825 (1995).
7. Yu. I. Bychkov, V. F. Losev, V. V. Savin, *et al.*, Izv. Vyssh. Uchebn. Zaved., Fiz., No. 1, 81 (1978).
8. U. Rebhan, J. Hildebrandt, and G. Skopp, Appl. Phys. **23**, 341 (1980).
9. A. I. Fedorov, Pis'ma Zh. Tekh. Fiz. **27** (24), 52 (2001) [Tech. Phys. Lett. **27**, 1050 (2001)].
10. J. I. Levatter and Shao-Chi Lin, Appl. Phys. Lett. **25**, 703 (1974).
11. E. Armandillo and A. J. Kearsley, Appl. Phys. Lett. **41**, 611 (1982).
12. A. Rothem and S. Rosenwaks, Opt. Commun. **30**, 227 (1979).
13. A. I. Fedorov, Opt. Atmos. Okeana **8**, 1664 (1995).
14. A. I. Fedorov, Opt. Atmos. Okeana **11**, 135 (1998).
15. V. V. Apollonov and V. A. Yamshchikov, Kvantovaya Élektron. (Moscow) **32**, 183 (2002).
16. B. A. Kozlov, R. I. Ashurkov, M. A. Akinin, *et al.*, Izv. Ross. Akad. Nauk, Ser. Fiz. **66**, 1172 (2002).
17. V. V. Atezhev, S. K. Vartapetov, A. K. Zhigalgin, *et al.*, Kvantovaya Élektron. (Moscow) **34**, 790 (2004).
18. A. I. Fedorov, Pis'ma Zh. Tekh. Fiz. **26** (26), 71 (2000) [Tech. Phys. Lett. **26**, 876 (2000)].

Translated by P. Pozdeev